Politecnico di Torino

ScuDo
Scuola di Dottorato ~ Doctoral School
WHAT YOU ARE, TAKES YOU FAR

Doctoral Dissertation

Doctoral Program in Electrical, Electronics and Communications Engineering

(34^{th}cycle)

EM Device for Cerebrovascular Diseases Imaging

Design, Implementation and Experimental Validation

By

David O. Rodríguez-Duarte

******

Supervisor(s):

Prof. Francesca Vipiana, Supervisor

Prof. Jorge A. Tóbon Vásquez, Co-Supervisor

Doctoral Examination Committee:

Prof. Jean-Charles Bolomey, Referee, University Paris-Saclay, France

Prof. Marko Helbig, Referee, Ilmenau University of Technology, Germany

Prof. Mario Casu, Politecnico di Torino, Italy

Prof. Raquel Cruz Conceição, University of Lisbon, Portugal

Prof. Jan Vrba, Czech Technical University in Prague, Czech Republic

Politecnico di Torino

2022

Declaration

I hereby declare that, the contents and organization of this dissertation constitute my own original work and does not compromise in any way the rights of third parties, including those relating to the security of personal data.

David O. Rodríguez-Duarte
2022

* This dissertation is presented in partial fulfillment of the requirements for **Ph.D. degree** in the Graduate School of Politecnico di Torino (ScuDo).

This is in memory of my loved grandma, who always had me in her prayers.

Acknowledgements

This work was supported in part by the Italian Ministry of University and Research under the PRIN project “MiBraScan”, and in part by the European Union’s Horizon 2020 research and innovation program under the EMERALD project, Marie Skłodowska-Curie grant agreement No. 764479. It would not be possible without the help and support of a huge group of people and institutions. I want to begin by thanking EMERALD (ElectroMagnetic imaging for a novel genERation of medicAL Devices) initiative, which gave me the tools for developing as a person and high-class researcher, allowing me to meet and work together with some of the most brilliant people in different incredible institutions. Starting from my home institution, POLITO, I thank, first, my supervisors, Francesca and Jorge, who were always there when I needed them, answering all my questions and backing my ideas. I could no ask for better supervisors. You are models to follow. Also, thanks to my non-official co-supervisors Lorenzo and Rosa from CNR-IREA(IT). I really appreciate how you open and share all your acknowledge and experience without hesitation. Then, I cannot forget my friends and colleagues from our Wavevision Group, Cri, Gio, Javi, Marco, Martin, and Vale. It is always a good time to take a coffee with you and change the world. Moreover, I would like to mention the institutions and people who hosted and collaborated with me during my visiting periods. Thanks to Wipl-D group, you are great team of EM experts, but more importantly people. I enjoy a lot my time in Belgrade. Kings College, even if was partially on-line, the two-ways collaboration very valuable. Ilumens Center and Sorbonne University, thank you for providing the medical images and the fruitful discussions on the medical aspects and on the modeling manufacturing of the phantoms, and the stroke problem. I bring with me this medical perspective. Finally, thank Keysight for open me your lab and expertise on calibration techniques. I was great know also the research from the industrial side. Finally, I would like to remember my dear ESRs, you are wonderful group of brilliant minds.

Finally, Infinitas Gracias! to my loving parents and sister, who always believe in me, and all my love to my Morita!, who was always next to me during this challenging travel.

Abstract

This thesis deals with the application of microwave imaging technology to the medical diagnosis and therapeutic follow-up of cerebrovascular diseases, a subject of marked health impact worldwide. The work persuades to accelerate the technology translation from the research bench to the patient bedside, paving the way for future clinical studies with patients.

Crossing microwave engineering and medical imaging, hence, going beyond the strict electromagnetic aspects, the thesis presents the development and validation of a two-version innovative full-fledged in-laboratory prototype for imaging and monitoring cerebrovascular diseases. Specifically, the last version, consisting of a 22-antenna-array placed conformal to the upper head part, each being a flexible antenna with a custom-made matching medium.

The proposed system uses a differential imaging scheme based on a linear reconstruction algorithm, drastically reducing the computational burden while speeding the image reconstruction to a real-time operation. The algorithm then forms 3-D dielectric contrast maps by employing the online measured scattering matrices and exploiting the distorted Born approximation and the truncated singular value decomposition (TSVD), where the operator is advantageously off-line computed via accurate numerical models and an in-house Finite Element Method (FEM) Solver. Additionally, the imaging procedure includes pre-calibration and post-calibration techniques performed at the hardware and software level that compensate for drifts or uncertainties in system components and noise propagated through the operator.

The experimental validation subjects the system to emulated hemorrhagic and ischemic stroke conditions using anthropomorphic phantoms filled with liquids, mimicking their dielectric properties. The results verify the system's capabilities to live-track the continuous evolution of the stroke, indicating its location, approximated shape, and clinical state change. Overall, the work validates the proof-of-concept of

brain stroke follow-up using microwave imaging in non-trivial conditions moving from the design problem to experimental validation, while applying an iterative problem-center methodology with inputs and feedback from both the technical and clinical sides.

The work results thus in a preliminary pre-clinical prototype that brings closer the trials on volunteers and patients. Even if the next step in clinical translation of the microwave-based imaging system will not be straightforward, the knowledge gained thanks to this thesis constitutes a solid and precious basement for continuing.

Contents

List of Figures

List of Tables

Chapter 1

Introduction

Imaging-based technologies are essential to support instruments for diagnosis, planning intervention, and monitoring of Acute Cerebrovascular Diseases referred to as brain stroke. However, current solutions lack aspects such as portability or non-continuous follow-up capabilities, leading to unmet medical needs and opening to alternative technologies, like microwave the Microwave Imaging (MWI), that fill the gaps. After being on the air for at least three decades, MWI devoted to the medical application is gaining momentum and engagement within the medical community, a fundamental factor in its success. The growing computational power partially pushed this engagement, jointly with improved performance of MW devices with reduced costs, all supported by a matured theoretical background. With this encouraging panorama, this thesis accelerates the development of the MWI technology via developing a full-fledged low-complexity system for imaging and follow-up cerebrovascular diseases, encountering the imaging as both a medical and an engineering problem.

This introduction, divided into four main sections, contextualizes stroke as a medical and engineering problem, baring the motivation behind an MWI device. The first section points to the medical problem of the stroke, getting into the main medical aspects, its relevance and impact, and the driving factors of this thesis. It identifies the need and possible use of an MWI system and its complementarity with the current gold standard imaging-based techniques. It contains a general description of the pathology and their different classifications and including an overview of the medical protocol from the moment of the onset toward the diagnosis and later treatment

and monitoring. The second part illustrates the electric contrast mechanism, MWI principle, and its relation with the studied clinical scenario. It also overviews the state-of-the-art and technological challenges. Then, the thesis objectives are stated and the followed methodology is introduced in the third part. Finally, the last section outlines the remaining chapters and list the publication linked to this work.

1.1 Stroke, a Serious Issue

Cerebrovascular diseases are one of the major causes of death and permanent disability, affecting more than thirteen million people per year worldwide [1] and impacting significantly the burden of healthcare systems and their repercussion is aggravated with the aging of the global population, which is more susceptible to them. These diseases comprehend pathological disorders that temporarily or permanently affect the normal blood flow through one or more vessels in the brain causing an improper rich-oxygen blood supply and thus the permanent damage or death of brain cells at a rate of millions per minute, which cannot regenerate. Then, the stroke affection results in severe long-term physical, cognitive, mental disabilities, or even death [2].

The brain is one of the more complex organs in the human body that controls thought, memory, emotion, touch, motor skills, vision, breathing, temperature, and every regulated process in our body. It is made up of more than 100 billion nerves that communicate in trillions of connections called synapses, though it is oxygen-blood fed and nourished by just two sets of arteries, carotid and vertebral, being very sensitive to any anomalous variation of the blood flow. The carotid arteries provide blood to the frontal two-thirds of the brain through two large intracranial arterial branches– the anterior cerebral and middle cerebral arteries and several smaller arteries –. The vertebral arteries join the basilar artery forming the vertebrobasilar system, located close to the skull base and brain stem, which supply the posterior third of the brain [3].

The flow alterations may occur from the stenosis (vessel narrowing), thrombosis (clot formation), embolism (blockage) that provokes a lack of sufficient blood flow (ischemia), affecting brain tissue and causing an ischemic(IS) stroke, which is the most frequent stroke category, counting for around 85% of the cases [4]. During an IS stroke, commonly, the arteries are not entirely obstructed, and a meager bloodstream trickles to the brain. Hence, the affected area comprehends a core and

a penumbra. In the core, the blood is almost completely cut off, starving the cells within minutes. The penumbra is a much more extensive area surrounding the dead cells in the core, consisting of injured and malfunctioning cells (idling cells), which can remain in this state for about three hours before they die. Depending on the time window, physicians treat the IS stroke by removing the blocking and restoring blood flow to the brain using thrombolytic drugs or mechanical devices. However, the medication increases the risk of intracranial hemorrhage. The remained 15% of stroke cases count for hemorrhagic stroke, which is the most deadly. In this case, blood vessel rupture (hemorrhage) may cause bleeding and damage to the brain. If the vessel breaks inside the brain, it is an intracerebral hemorrhage(ICH), while it is a subarachnoid hemorrhage if it breaks on the brain surface. It is usually surgery treated to relieve intracranial pressure (within the skull) caused by bleeding.

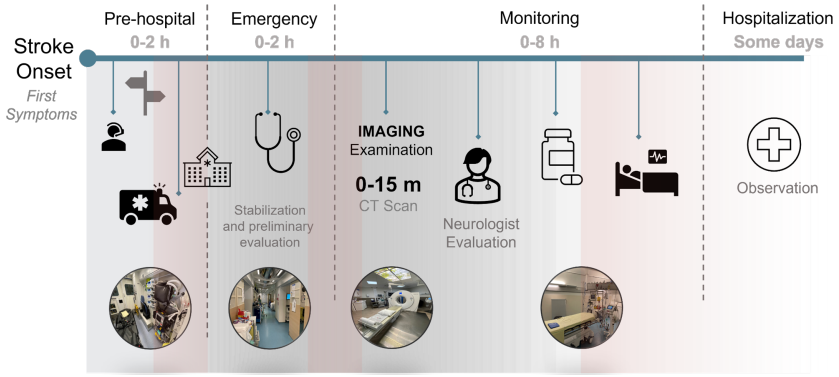

Fig. 1.1 Medical protocol for an stroke case

Regardless of the stroke typology, it is primordial that the victims receive a prompt diagnosis (detection, classification, and localization) and subsequent emergency medical care to restore the proper blood flow and oxygen as soon as possible to reach the best possible outcome and try to mitigate the devastating consequences of this disease. However, according to the European Stroke organization, less than 10% of patients reach the hospital within 60 minutes of stroke onset [5]. Once the stroke onset and first symptoms appear, the protocol suggests calling for an ambulance or approaching a dedicated medical center/hospital immediately. Then, the medical personnel stabilizes the patient and preliminary assess his condition. The next 8-hour stage is pivotal, there, clinicians and therapists monitor and evaluate the patient supporting generally their prognosis and intervention with imaging-based technologies such as magnetic resonance imaging (MRI) and computerized X-ray tomography

(CT). Finally, after some hours, the patient is referred to hospitalization, remaining for some days due to the high risk of a second stroke event. Fig.1.1 illustrates the emergency stroke protocol, where the red stripes signal potential time windows in which an additional MWI procedure could be applied without effect significantly on the standard protocols.

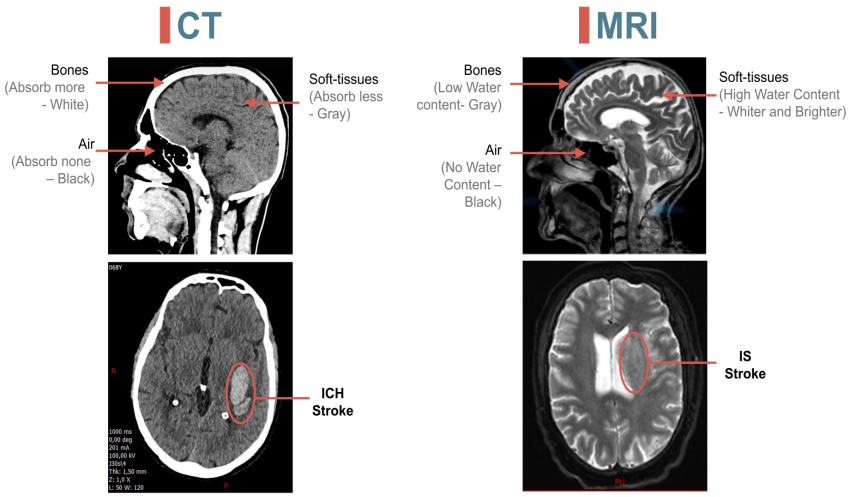

Fig. 1.2 Examples of CT and MRI images.[1]

MRI and CT are the current gold standard for medical imaging support, these are well-established and deliver highly reliable diagnostic information (see Fig. 1.2). Depending on the installations and availability, the patients with stroke symptoms undergo either MRI or CT examinations, which allow physicians to identify the stroke-affected area. However, these techniques still have intrinsic drawbacks in terms of availability, portability, cost, time-consume, and safeness (for CT only) that limit their applicability [6]. Regarding the availability, it has to be considered first the equipment at hand in the emergency and neurological departments, and second, the number of patients arriving and under observation at the moment of the emergency. As result, even in big hospitals, the imaging-based support is limited to the initial assessment, which might take between 15 to 30 min depending on the exam, and a follow-up examination hours after the onset and the initial treatment. This situation aggravates in developing countries [7]. Moreover, MRI and CT scanners are bulky devices, and cannot be normally installed in an ambulance or

[1] Anonymized images provided by the Emergency Medicine Dept. of Lariboisière University Hospital, Paris (FR).

mobile care unit(see Fig. 1.3 A-C,F), doing unable the pre-hospital diagnosis, or directly set in the bedside in the emergency department (see Fig. 1.3 D-E) or later during the observation period. Sum to the mentioned points, these machines are very expensive and required specialized operators, and in the CT case, it employs ionizing radiations, making it risky repetitive monitoring even with new low dose devices. In this context, microwave imaging is an attractive technological solution, non-ionizing, non-invasive, cost-effective, and complementary to current solutions, which have the potential to perform pre-hospital diagnosis and continuous bedside follow-up during the post-acute stage, albeit at the cost of a lower resolution.

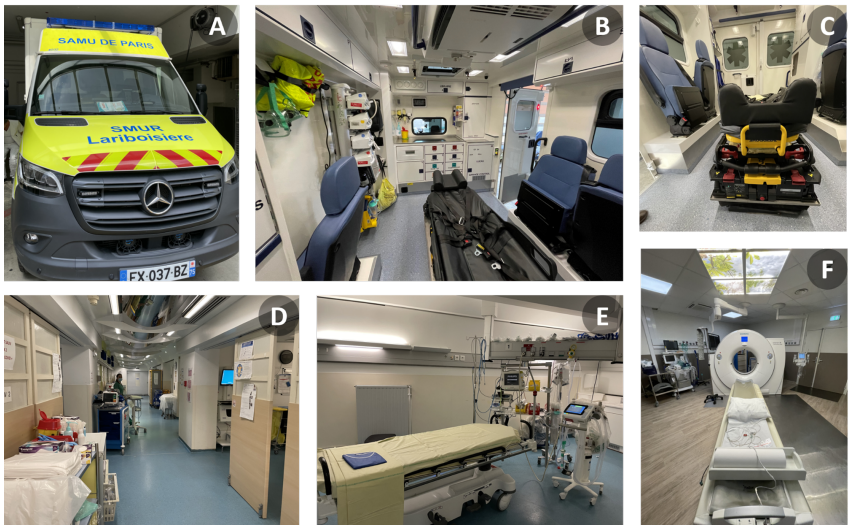

Fig. 1.3 Emergency installations. A: Movil Emergency Care Unit (Ambulance); (B) A interior; (C) A gurney; (D) emergency department; (E) emergency room; (F) CT Scanner[2].

1.2 MWI as an Alternative

Microwave imaging (MWI) is a technology that generates images of the body's internal structures using the resultant backscattered signals after illuminating it with low-power EM waves (in the GHz range of the spectrum, called microwave spectrum). Thus, it penetrates opaque media while maintaining a spatial resolution compatible with some medical diagnostic modalities. MWI aims to provide correlated images of the presence of pathology with either qualitative or quantitative

[2]Original pictures of the Emergency Medicine Dept. of Lariboisière University Hospital, Paris (FR), taken during a visit to its installations.

maps of the region under study, relying on the contrast of the electrical properties (permittivity and conductivity). For instance, in the stroke case, the endogenous dielectric property contrast between the healthy brain tissues, e.g., gray matter and white matter, is present compared to stroke-affected (ischemic or hemorrhagic) zones. Hence, reducing the blood flow, an IS case drops the injured zone's electrical properties, passing from a relative permittivity and conductivity of around 45 and 0.8 S/m, respectively, for the healthy brain to 36 and 0.7 S/m, at 1 GHz. Conversely, in the ICH case, the blood accumulation presents higher properties, reaching permittivity values over 60 and 1.5 S/m at 1 GHz.

Microwave-based medical-oriented imaging technology began in the early 80s, and has ongoing development since, distinguishing two development periods. The first, maturation, extended until the mid-1990s, considers preliminary investigations on samples or isolated organs and paves the MWI concepts [8]. The second, clinical acceptance, concentrates on developing the first generation of operational imaging systems dedicated to early preclinical assessment. This period extends until our days when the move to pre-clinical trials is expected and is impulsed by the growing involvement of electromagnetic science and engineering communities, boosting computing power for system design and optimization, high-fidelity synthetic assessment, and new retrieval algorithms.

Focusing on the second period, let first consider the significant efforts toward microwave breast imaging resulted in multiple pre-clinical systems motivated by the fact that there is considerable dielectric contrast between malignant and normal tissue. The earliest drives assume the breast tissue is primarily fatty compared to the tumors that contain more water. Though, later studies have shown a more nuanced breast tissue composition. The development of the area has taken more than expected. Nevertheless, today, we can find a growing number of devices worldwide giving crucial clinical trials. For example, as one of the pioneers, we found Dartmouth's device, which first pre-clinical prototype was launched in the mid-90s, and from those has been upgraded to a low-cost and entirely custom hardware device in our days. Another example is Maria, a device born initially at the University of Bristol and later transitioned to a spin-off, Micrima. Similarly, we found Wavelia by MVG Industries, Mammowave by UBT, a spin-off of the University of Perugia, MBT (Microwave Breast Tomography) by Mitos Medical Technology, a spin-off of Istanbul Technical University, and WaveViwe Imaging device, a spin-off of the University of Calgary. Moreover, still in the academy, stand out the works from

McGill University and McMaster University. The extensive work on breast imaging has first allowed gaining a very significant amount of knowledge on reconstruction algorithms, imaging system setups, mimicked virtual and experimental validations, calibration techniques, and clinical approaches, which to some extent acts like a trampoline for the brain stroke application. Also, and evenly important, these developments have been pushing the acceptance of the technology.

Fig. 1.4 Examples of MW systems. (left):Stroke finder[9], (middle):the EMTensor BrainScanner[10], (right):EMVision Scanner[11].

Now, moving to the brain stroke application, several MWI devices have recently been proposed by academia and industry communities and mix-collaboration. Starting with systems already tested on humans and under clinical investigation, we find three notable examples of portable devices, the Strokefinder, the EMTensor BrainScanner, and the EMVision Scanner (see Fig. 1.4). Medfield Diagnostics developed the Strokefinder, a compact, low-complexity, and patient-adaptable device made of 8 antennas, aiming to discriminate the stroke typology early in the pre-hospital stage [9, 12]. This first case does not aim to generate images of the stroke, though it is an excellent example of narrowing the clinical problem and the system functionalities that still retrieves a piece of vital information for doctors and physicians, being an ideal complement to current imaging-based solutions. The second example, EMTensor BrainScanner [13], has its beginnings in the early-90s and our days are in the process of FDA release approval. Its technology performs brain tomographic imaging via a portable system, which allows it to approach in-ambulance and bedside scenarios. However, EMTensor uses a highly complex system consisting of 177 loaded and truncated waveguides(radiating elements) in its initial version, increasing the complexity of data processing inherently. The last one, EMVision Scanner [11], is a tomographic imaging device born from the research at The University of

Queensland that has migrated to the industry in the last decade with encouraging results in the undergoing clinical trials.

Moreover, we can also find notable developments from the academy in the preliminary stages. The King's College London group developed a device with an 8-antenna array submerged in glycerine as a matching medium, performing a 3-D non-linear microwave tomography imaging via a distorted Born iterative method DBIM with GPU-accelerated FDTD [14]. In [15, 16], authors present a 2-D tomographic approach to resolve a non-linear inversion in Lebesgue spaces, which is tested in a system with a 16-antenna array ring, where the matching medium consist of heat-sealed polyethylene bags filled up with a water-glycerine-based liquid. There are also multiple efforts from the University of Queensland group, which in [17] show 14-antenna array and a novel polar sensitivity encoding (PSE) algorithm to locate the stroke. Moreover, in [18], they propose a flexible-24-antenna cap and 3-D tomography imaging technique, achieving the location of the stroke in complex scenarios, yet with limited shape retrieval and non-monitoring testing. Another example is [19], where is presented a novel hybrid system using both a radar approach and a frequency approach for the imaging using an 8-element array of UWB Bowtie Antenna in a 2-D configuration.

Following the growing machine learning interest, have emerged recently several works related with the brain stroke imaging and classification [20–26]. In [25] is reported a clinical study where scattering data measured on patients and healthy volunteers are used in a supervised algorithm aimed to differentiate HEM from IS stroke, by creating two different linear sub-spaces sharing common features. An unsupervised ML method is implemented in [22] to localize brain anomalies, while it is not meant to discriminate stroke type. Here the statistical fields between antenna pairs in a ring array are computed and merged within the imaging domain and the pixel intensity is interpreted as the likelihood of an anomaly being present, obtaining good 2D reconstruction in experimental scenarios.

Hence, exploiting the non-invasive and harmless nature of microwaves and the current high-performance microwave hardware and computing power, MWI solutions arise as a complement to overcome the limitation of cost, portability, and harmfulness of traditional diagnostic techniques. For example, there are a rising number of day-to-day medical problems that are beginning to be explored. In [27], the authors explore the traceable variations in time as breast cancer. [28] applies

the methods to knee injuries. [29] preliminary validates MWI applied to cervical diseases. Auxiliary lymph node detection is being studied in [30, 31]. Also, MWI is a promising candidate for non-invasively monitor the tissue temperature during hyperthermia treatment [32], or real-time monitoring thermal ablation treatments of liver tumors [33]. Summing up, MWI technology:

- exhibits favorable penetration depths that allow imaging of tissues deeper in the human body as compared to other emerging modalities (e.g., optical techniques);
- is entirely harmless since the involved waves are non-ionizing and used in very low doses (low-power EM waves);
- is economic-efficient for the healthcare system. Back up for advancement in the mobile industry and microwave devices in recent years, it has the potential to provide mobile, low-cost imaging platforms.

1.3 Objectives and Methodology

The preliminary sections glimpse the significant clinical challenge that represents cerebrovascular diseases nowadays, both owing to their pervasiveness (related to the aging of the population), and the intrinsic limitation of current imaging modalities—for instance, the non-viability for a repeated operation that would allow a continuous post-event monitoring of stroke, improving the effectiveness of treatments. Moreover, it shows the potential of microwave-based imaging technologies to overcome these issues as supplementary and complementary support alternatives, filling an unoccupied segment of the medical imaging market.

Considering the typical evolutionary timeline of a medical imaging modality [34], MWI technologies are reaching the maturation stage, thanks to the extensive experience gained in the past three decades, and is moving through the clinical acceptance stage, which is characterized by the clinical focusing and technology refinement that results in application-based imaging systems, continued investigation, and early(pre) clinical trials. In this context, this thesis is framed within EMERALD (ElectroMagnetic imaging for a novel genERation of medicAL Devices), a European cohort working on accelerating the translation of the electromagnetic (EM) technology for medical imaging from the research bench to the patient bedside, promoting a

multi- and inter-disciplinary collaboration between engineers groups with clinicians and stakeholders (hospitals and university medical centers).

In the specific, this work aims to accelerate the translation of research on EM medical imaging into clinical prototypes by advancing the technology and developing a low-cost pre-clinical mobile device for imaging cerebrovascular diseases, wherein MWI technology can play a significant role in real-time managing traumatic events, such intracranial hemorrhages, which is currently an unmet clinical need. Hence, in order to accelerate the technology, this works aim to develop an MWI device for cerebrovascular imaging, covering both the software and hardware elements, and then the design, implementation, and validation.

Moving to the methodology and being conscious that the clinical translation requires not only a further investment in the technology but also well-planned research, training, and multi-disciplinary collaboration, this work strives first to build the common ground upon which promotes a feedback loop between technology, clinical needs, and user awareness. The thesis copes with this challenge by starting with the medical consideration (protocols and pathological process) to adjust the scope according to the current operational capabilities and clinical needs, approaching a user-center solution instead of a general one. This preliminary step has a two-fold purpose. First, increase the engagement of the clinical community, which is an essential driver for technology take-off. Second, a clear understanding of the medical situation, that might guide a reduction in the complexity of the imaging process, converging toward a clinically acceptable solution. In colloquial words, the idea was to keep it simple!. Thus, the clinical target is application-driven adjusted, and focused on continuous follow-up of the stroke-affected area in accordance with the operational capabilities currently offered.

Addressing the above issues represents an engineering effort regarding designing and implementing properly composed and dedicated hardware and software and their respective integration. Then, the radiation elements (antenna) are optimized and initially tested synthetically for the former. Similarly, once validated the performance of the antenna is, the complete system is also synthetically tested using different virtual scenarios, providing a first view of the system's capabilities. In this first stage, the EM modeling of the virtual twin plays a pivotal role in guiding the tuning of the system. Also, this preliminary stage appraises the imaging algorithm. After the synthetic test and following an equivalent approach, the antenna module is tested first,

and then the whole system is assessed under different mimicked clinical scenarios. Here, the imaging algorithms are tailored, and calibration and artifacts removal techniques are included. Summing up, the whole design loop was repeated two times, including the feedback from both the technical and clinical parts in each iteration.

1.4 Thesis Outline

The remaining part of this work is composed of four chapters that collect the materials, methods, and results used and reached to get a low-complexity MWI device for real-time monitoring of brain stroke.

Chapter 2 covers the fundamentals behind microwave imaging retrieval. Starting with the general description of MWI, first, the forward problem is stated, and then the ill-possess and the inversion is approached. Later, qualitative and quantitative techniques are described, highlighting the factors considered in our selection, i.e., a linearization using the Born approximation and the regularization and inversion using a truncated singular value decomposition (TSVD). Here, details, pros, and cons of the technique are commented on. The last section explores different calibration techniques required during the experimental procedures.

Chapter 3 focuses on the design and implementation of the prototype, paving the way toward the validation chapters. The section covers design constraints such as operation frequency, number of antennas, layout and matching medium, and the followed process to face them. Then, a section presents the EM modeling, a crucial tool for speeding up the design process and the imaging algorithm, including a description of the FEM solver and the high-realistic modeling of the problem. With a base design, the next section moves to the prototype implementation, commenting on its different components, i.e., switching matrix, vector network analyzer (VNA), and antennas. Lastly, the chapter closes by presenting the manufacturing of the experimental phantoms, head (average and multi-tissue), and stroke, including the recipes and characterization of the tissue-mimicking liquids.

Chapter 4 approaches the validation of the system in two parts, a synthetic Validation and an experimental one. Worth mentioning that, as the design process includes two full iterations, meaning two versions of the system, each of them

is covered synthetically and experimentally. The synthetic validation starts with the single antenna element and then the full system, creating digital twin models of the system that are employed for the building of the imaging kernel and as a preliminary analysis instrument of the capabilities of the system. The synthetic analysis gives an indication of the performance of the system in ideal conditions and helps to understand also the limitation of the practical implementation. The second chapter part is dedicated to the experimental validation, including the experimental procedures, results, and analysis of them. An initial section approaches the first prototype, focusing on the detection and localization of the stroke. The second section, then, concentrates on the monitoring aspects, which are explored using the last version of the device.

Finally, the conclusion chapter gathers the take-home message of the work, considering the learning points from it and the step-forward contribution. Moreover, the last part includes the perspectives, future research directions, and final remarks and consideration towards the clinical acceptance of MWI technology for brain stroke.

1.5 List of publications

Book Chapter

D. O. Rodriguez-Duarte, J. A. Tobon Vasquez, R. Scapaticci, G. Turvani, M. R. Casu, L. Crocco and F. Vipiana, "Towards a Microwave Imaging Device for Cerebrovascular Diseases Monitoring: from Modeling to Experimental Testing," in Electromagnetic Imaging for a Novel Generation of Medical Devices - Fundamental Issues, Methodological Challenges and Practical Implementation, Springer, 2022

Journals

D. O. Rodriguez-Duarte, C. Origlia, J. A. Tobon Vasquez, R. Scapaticci, L. Crocco and F. Vipiana, "Brain Stroke Live-traking via a Microwave Scanner," in IEEE Open Journal of Antennas and Propagation, 2022, 11, (Submitted)

D. O. Rodriguez-Duarte et al., "Experimental Validation of a Microwave System for Brain Stroke 3-D Imaging," in Diagnostics, 2021, 11, 1232, doi: 10.3390/diagnostics11071232

D. O. Rodriguez-Duarte, J. A. Tobon Vasquez, R. Scapaticci, L. Crocco,and F. Vipiana, "Assessing a microwave imaging system for brain stroke monitoring via high fidelity numerical modelling," *IEEE Journal of Electromagnetics, RF and Microwaves in Medicine and Biology*, vol. 5, no. 3, pp. 238–245, 2021, doi: 10.1109/JERM.2020.3049071

D. O. Rodriguez-Duarte, J. A. Tobon Vasquez, R. Scapaticci, L. Crocco and F. Vipiana, "Brick Shaped Antenna Module for Microwave Brain Imaging Systems," in IEEE Antennas and Wireless Propagation Letters, vol. 19, no. 12, pp. 2057-2061, 2020, doi: 10.1109/LAWP.2020.3022161

J. A. Tobon Vasquez, R. Scapaticci, G. Turvani, G. Bellizi, **D. O. Rodriguez-Duarte**, et al., "A Prototype Microwave System for 3D Brain Stroke Imaging," in Sensors, vol.20, no. 9, May 2020, doi: 10.3390/s20092607

Conferences

D. O. Rodriguez-Duarte, C. Origlia, J. A. T. Vasquez, R. Scapaticci, L. Crocco, and F. Vipiana, "Wearable Microwave Imaging System for Brain Stroke Imaging," 2022 IEEE International Symposium on Antennas and Propagation and USNC-URSI Radio Science Meeting (APS/URSI), 2022

D. O. Rodriguez-Duarte, J. A. T. Vasquez, and F. Vipiana, "Moving forward to real-time imaging-based monitoring of cerebrovascular diseases using a microwave device: Numerical and experimental validation," in 3rd URSI Atlantic/Asia-Pacific Radio Science Meeting 2022(3rd URSI AT-AP-RASC), Gran Canaria, Spain, 2022 (*Young Scientists Award*)

J. A. T. Vasquez, **D. O. Rodriguez-Duarte**, C. Origlia, and F. Vipiana, "Microwave imaging device prototype for brain stroke 3d monitoring," in International Workshop on Antenna Technology(iWAT), Dunlin, Ireland, 2022. (*Invited*)

D. O. Rodriguez-Duarte, S. de Luque Arias, J. A. Tobon Vasquez, R. Scapaticci, L. Crocco, and F. Vipiana, "A portable microwave scanner for brain stroke monitoring: Design, implementation and experimental validation," in 2022 16th

European Conference on Antennas and Propagation (EuCAP), 2022, pp. 1–5, doi: 10.23919/EuCAP53622.2022.9769048 (*Finalist in the category Best Propagation Paper Award*)

C. Origlia, **D. O. Rodriguez-Duarte**, J. A. Tobon Vasquez and F. Vipiana, "Microwave Antenna Array Calibration via Simulated and Measured S-parameters Matching," in 2022 16th European Conference on Antennas and Propagation (EuCAP), 2022, pp. 1–4, doi: 10.23919/EuCAP53622.2022.9769081.

D. O. Rodriguez-Duarte, C. Origlia, J. A. T. Vasquez and F. Vipiana, "Hybrid Resolvent Kernel Calibration Technique for Microwave Imaging Systems," 2021 IEEE International Symposium on Antennas and Propagation and USNC-URSI Radio Science Meeting (APS/URSI), 2021, pp. 2014–2015, doi: 10.1109/APS/URSI47566.2021.9704044. (*C. J. Reddy Travel Grant for Graduate Students*)

D. O. Rodriguez-Duarte, J. A. T. Vasquez and F. Vipiana, "Multi-shot Calibration Technique for Microwave Imaging Systems," 2021 IEEE Conference on Antenna Measurements & Applications (CAMA), 2021, pp. 476-480, doi: 10.1109/CAMA49227.2021.9703495. (*IEEE AP-S Tapan Sarkar Best Student Paper*)

D. O. Rodriguez Duarte, J. A. Tobon Vasquez and F. Vipiana, "Microwave Brain Imaging System Validation via Realistic Experiments," 2021 URSI Gaas. (Second Prize - Student Paper Competition)

J. A. Tobon Vasquez, **D. O. Rodriguez-Duarte**, R. Scapaticci, G. Turvani, G. Bellizi, et al., "Experimental Imaging Issues of a 3-D Microwave Brain Scanner," 2021 IEEE ICEAA.

E. Razzicchia, N. Ghavami, **D. O. Rodriguez-Duarte**, J. A. Tobon Vasquez, F. Vipiana and P. Kosmas, "Benefits of Employing Metasurfaces on the Design of a Microwave Brain Imaging Scanner," 2021 IEEE ICEAA.

D. O. Rodriguez-Duarte, J. A. Tobon Vasquez and F. Vipiana, "Hybrid Simulation-Measurement Calibration Technique for Microwave Imaging Systems," EuCAP, 2021

D. O. Rodriguez-Duarte, J. A. Tobon and F. Vipiana, "Realistic Numerical Modelling for 3-D brain stroke monitoring," 2020 IEEE AP-S

D. O. Rodriguez Duarte, J. A. Tobon Vasquez and F. Vipiana, "Electromagnetic Virtual Prototyping of a Realistic 3-D Microwave Scanner for Brain Stroke Imaging," EuCAP, 2020

D. O. Rodriguez Duarte, J. A. Tobon Vasquez, R. Scapaticci, B. Kolundzija, L. Crocco and F. Vipiana, "High Fidelity Modelling of a Microwave Imaging Device for Brain Stroke Monitoring," PhotoIncs & Electromagnetics Research Symposium(PIERS), Xiamen, China, 2019

J. A. Tobon Vasquez, **D. O. Rodriguez Duarte**, R. Scapaticci, G. Turvani, G. Bellizi, N. Joachimowicz, B.Duchene, M.Casu, L. Crocco and F. Vipiana, "Experimental Testing and Calibration Issues in the Realization of a Microwave Imaging Device for Brain Stroke Monitoring," PhotoIncs & Electromagnetics Research Symposium(PIERS), Xiamen, China, 2019

D. O. Rodriguez Duarte, M. A. Mansoori, J. A. Tobon Vasquez, G. Turvani, M. R. Casu and F. Vipiana, "Development of an EM Device for Cerebrovascular Diseases Imaging and Hardware Acceleration for Imaging Algorithms within the EMERALD Network," EuCAP, 2019

Chapter 2

Microwave-based Live-tracking Imaging

This chapter examines the principles and mechanisms associated with the MWI, discussing first the inverse problem as a general physical problem and then as an electromagnetic inverse scattering problem (ISP). Hence, the imaging algorithm is studied considering the followed strategies for dealing with the non-linearity and ill-possness in a realistic scenario of brain stroke imaging in real-time, i.e., a linearization using the Born approximation and the regularization and inversion using a truncated singular value decomposition (TSVD). Additionally, considering that the second part of the validation is experimental, it describes calibration techniques that are required during the practical functioning.

2.1 The inverse Problem behind the imaging

The direct problem, termed also forward (**FW**), in general physics alludes to calculating the consequences of given causes, whereas the inverse problem seeks to discover unknown causes of known effects. To solve an inverse problem, the direct-inverse pair's foundation must be described in well-established physical principles, establishing the relationship, or equation, between the effects and the causes. In a wave-propagation situation, for example, the forward problem computes the radiated field owing to a source, while the inverse problem derives the source from the radiated field knowledge. **FW** is both a cause-and-effect problem and one oriented

toward information loss, as its solution transits from a given information content inside a physical amount to another lower information quantity. Thus implying the direct solution is smoother than the data, meaning for instance that the scattered wave due to a rough object will be smooth [35].

Moving on to the inverse problem, it has a conceptual challenge in aiming for a transformation that corresponds to a gain of information, which is known as ill-posedness. A direct one, on the other hand, is well-posed, implying that its solution is unique, exists for any data, and is continuously dependent on the data. The first point in approaching a direct-inverse problem is to define the class of the objects to be imaged, which will be described by suitable function with certain properties. We also need a distance in this class to determine when two items are near together and when they are not. In this manner, our object class adopts the form of a metric space of functions. This object space is denoted here by χ. The second point is to address the direct problem, namely to calculate the appropriate image for each element, which is referred to as the computed image or the noise-free image. Because the direct problem is well-posed, we just link one image with each item. As previously said, because the information content of this image is smaller than the information content of the related item, it may appear smooth. This smoothness attribute, on the other hand, could not correspond to a noise-free picture corrupted by the noise impacting the measuring process. As a result, the third objective is to define the image class in such a way that both noise-free and noisy images are included. The equivalent function space is denoted by Υ and is referred to as the image space.

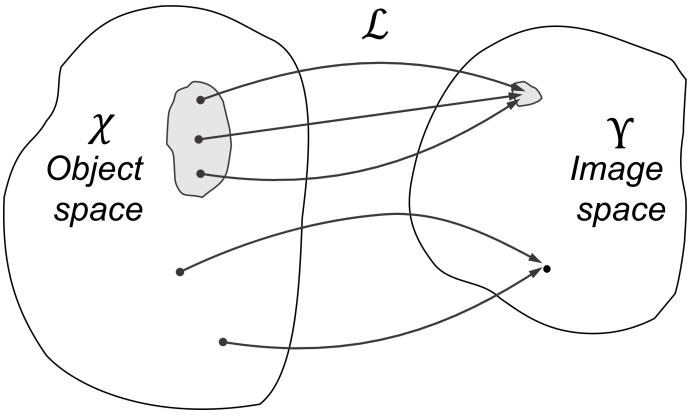

Fig. 2.1 Simplify imaging scheme.

Finally, the direct problem's solution specifies a mapping(operator), indicated by $\mathcal{L}$, that turns every object in space χ into a noise-free picture in space Υ. Because the direct issue is well-posed, this operator is continuous, i.e. the images of two near objects are also close. In mathematics, the set of noise-free images is known as the range of the operator, and, as we previously said, this range does not correspond with the image space Υ because this space also contains noisy images.

The mathematical description, $\mathcal{L}\chi = \Upsilon + w$, where w is the noisy, shows the loss of information occurring in the solution of the direct problem, as previously stated. It has two implications, illustrated in Fig. 2.1, each of which is mathematically described differently, despite the fact that their practical effects are very similar.

To begin with, it is possible that two or more elements share the same image. In the case of a linear operator, this is connected to the presence of an object whose image is exactly zero –Invisible objects–.Then, given an item in space Υ, we may add an invisible object to it to create a new object with the exact same image. Second, and this is a far more general statement than the last one, two rather quite apart objects can have very close images, meaning there are huge sets of unique objects that project to tiny sets of images.

Looking into the inverse problem, that is, discovering the item that corresponds to a given image, we see that it is ill-posed as a result of the information loss inherent in the direct solution, i.e., the ill-posedness is a consequence of the fact that the system operator does not transmit complete information about the imaged object. Thus, solving the problem is even challenging in noiseless scenarios. Indeed, if we have an image that corresponds to two different objects, the inverse problem's solution is not unique. If we have a noisy image that is outside of the range of the operator $\mathcal{L}$, the inverse issue has no solution, or when existing in a discretized problem, is deprived of physical meaning. The solution to the inverse problem does not depend on the data continuously if we have two nearby images with very distant equivalent objects.

In this framework, we can not expect an exact solution for the inverse problem. Instead, we aim for approximated solutions that reproduce the noisy object. Moreover, because of the ill-posedness, the space of approximated solution may be too broad containing not only the physical acceptable objects but also large and oscillating solutions. Then to deal with the ill-posedness the golden rule is to look for approximated solutions that fulfill extra constraints(prior information) imposed by the problem's physics [35], which is called the *regularization*.

The previously mentioned mathematical and graphical description can be used to clarify these ideas. The set of approximate solutions for the same data function is just the collection of objects with images that are close to the measure one (see the shaded areas in Fig. 2.1), which is a product of the information loss caused by the imaging process. Thus, to be able to solve the inverse problem is needed additional information, also, known as a-priory or prior information. It is unique and cannot be deduced from the image or the base mapping $\mathcal{L}$ features, which describe the imaging process, indicating certain predicted physical qualities of the object. For example, in practical application, the problem can be limited including detailed information about practical setup, e.g, geometrical one. The purpose of the prior information is to reduce the number of objects compatible with the given images or to distinguish between the actual and spurious objects caused by uncontrolled propagated noise.

Hence, the idea behind the regularization relies on limiting the family of an approximated solution, depending on a *regularization parameter*, in a way that in the case of a noise-free data, the functions of the family converge to the exact solution, while in the case of noisy data we obtain an optimal approximation of the exact one. Regularization acts with the premise of intentionally using additional information to generate families of approximate solutions that are consistent with the given image.

2.2 Inverse Scattering Problem

As aforementioned, one of the conditions to solve an inverse problem relies on having a set of equations that describe the cause-effect problem, forward one, that can be used a-posteriori to solve the inverse problem. Therefore, this section describes the scattering field problem's forward formulation, representing an MWI system applied to brain stroke monitoring. From the electromagnetic point of view, the scattering occurs when scatters (imaged objects) are illuminated by a radiation source (see Fig. 2.2), e.g., the stroke. The perturbation field due to the presence of the scatter is referred to as a scattered field.

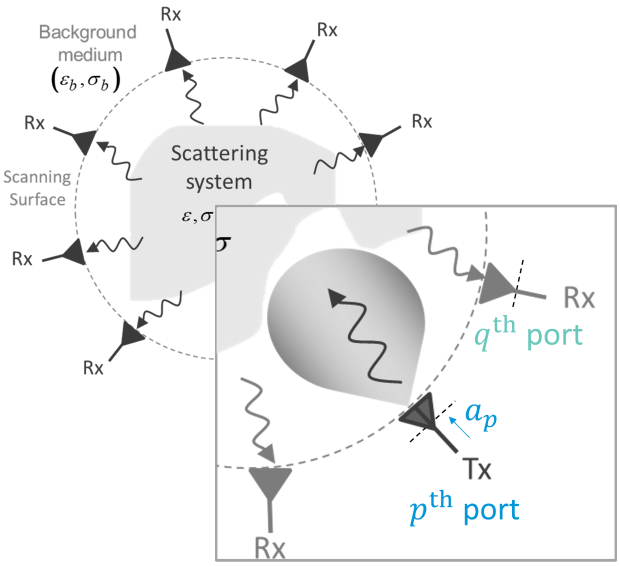

Fig. 2.2 General scheme of a MWI system

Figure 2.2 represents a schematic abstraction of an inverse scattering problem or an MWI system, where the unknown scatter is localized within the domain of interest (DOI), which is surrounded by the scanning surface. In terms of MWI, the DOI is used to represent also the domain of imaging. The transceivers, antennas that can act as either transmitter(Tx) or receiver(Rx), illuminate in Tx-mode the domain using incoming waves, which are then measured by an array of receivers. Hence, the solution to the inverse problem aims to determine the shape, position, and material of the scatter(Scattering system) from the measured scattered fields.

Now that a global picture of the problem was established, we move to the mathematical formulation of the problem. Thus, to define a common framework Maxwell's equations are stated as starting point. These are a set of fundamental equations that govern all macroscopic electromagnetic phenomena. These can be

written in differential as Eqs. 2.1 – 2.5

$$\nabla \times \mathbf{E} = -\frac{\partial \mathbf{B}}{\partial t} \qquad \text{(Faraday's law)} \tag{2.1}$$

$$\nabla \times \mathbf{H} = -\frac{\partial \mathbf{D}}{\partial t} + \mathbf{J} \qquad \text{(Maxwell-Ampère law)} \tag{2.2}$$

$$\nabla \cdot \mathbf{D} = \rho \qquad \text{(Gauss's law)} \tag{2.3}$$

$$\nabla \cdot \mathbf{B} = 0 \qquad \text{(Gauss's law–magnetic)} \tag{2.4}$$

$$\nabla \cdot \mathbf{J} = -\frac{\partial \rho}{\partial t} \qquad \text{(equation of continuity)} \tag{2.5}$$

where

$$\begin{aligned}
\mathbf{E} &= \text{electric field intensify (volts/meters)} \\
\mathbf{D} &= \text{electric flux density(coulombs/meter}^2\text{)} \\
\mathbf{H} &= \text{magnetic field intensify (amperes/meter)} \\
\mathbf{B} &= \text{magnetic flux density (webers/meter}^2\text{)} \\
\mathbf{J} &= \text{electric current density (amperes/meter}^2\text{)} \\
\rho &= \text{electric charge density (coulombs/meter}^3\text{),}
\end{aligned}$$

and in the case of time-varying fields there are three independent equation, either Eqs. 2.1 – 2.3, or Eqs. 2.1 – 2.2 with Eq. 2.5. Depending on the selection, the remaining two are called auxiliary or dependent equations. Moreover, to define Maxwell's equations are defined the following constitutive relations between the field quantities, which describe microscopically the properties of the medium.

$$\mathbf{D} = \varepsilon \mathbf{E} \tag{2.6}$$

$$\mathbf{B} = \mu \mathbf{H} \tag{2.7}$$

$$\mathbf{J} = \sigma \mathbf{E}, \tag{2.8}$$

where the constitutive parameters of the medium are defined as: permittivity ε (farads/meter), permeabilityμ(henrys/meter), and conductivity σ(siemens/meter). These are tensors in the case of anisotropic media and scalars for isotropic media. Also, for the latter in the case of homogeneity do not depend of the position. Moreover, when the Maxwell's equation are applied to harmonic fields with single

frequency, the field is refered to as time-harmonic, and these can be represented as

$$\nabla \times \mathbf{E} = -j\omega\mathbf{B} \tag{2.9}$$

$$\nabla \times \mathbf{H} = j\omega\mathbf{D} + \mathbf{J} \tag{2.10}$$

$$\nabla \cdot \mathbf{J} = -j\omega\rho. \tag{2.11}$$

With Maxwell's equations defined, we move to the formulation of the scattering problem. First, we assume that the scatter is immersed in a homogeneous background medium such as the air. Second, as we see from Fig. 2.2, and previously described, the scatter is illuminated by a primary source located outside of it.

Hence, using the linear superposition principle, we can decompose the fields $\mathbf{E}$ and $\mathbf{H}$ in terms of incident and scatter fields. The former, $\mathbf{E}^{inc}$ and $\mathbf{H}^{inc}$, is generated in absence of the scatter. Instead, the latter, $\mathbf{E}^{sc}$ and $\mathbf{H}^{sc}$, are due to the scatter itself. Then, in the scatter presence, the total fields in the close vicinity of the scatter are

$$\nabla \times \mathbf{E} = j\omega\mu\mathbf{H} \tag{2.12}$$

$$\nabla \times \mathbf{H} = -j\omega\varepsilon\mathbf{E}, \tag{2.13}$$

and the incident fields in the vicinity of the scatter in absence of it

$$\nabla \times \mathbf{E}^{inc} = j\omega\mu_b\mathbf{H}^{inc} \tag{2.14}$$

$$\nabla \times \mathbf{H}^{inc} = -j\omega\varepsilon_b\mathbf{E}^{inc} \tag{2.15}$$

Since $\mathbf{E} = \mathbf{E}^{inc} + \mathbf{E}^{sc}$ and $\mathbf{H} = \mathbf{H}^{inc} + \mathbf{H}^{sc}$, Eqs. 2.12–2.15 conduct to

$$\nabla \times \mathbf{E}^{sc} = j\omega\mathbf{H}^{sc} \tag{2.16}$$

$$\nabla \times \mathbf{H}^{sc} = -j\omega\varepsilon\mathbf{E}^{sc} - j\omega(\varepsilon - \varepsilon_b)\mathbf{E}, \tag{2.17}$$

where b stands for background. Thus the last term in Eq. 2.17 plays the role of electric current density, being a secondary source(induced source), that produce the same scattered field as the objected. Moreover, we can define the dielectric contrast as $\chi_e = (\varepsilon - \varepsilon_n)$.

$$\mathbf{J}_e = j\omega(\varepsilon - \varepsilon_b)\mathbf{E} = j\omega\chi_e\mathbf{E} \tag{2.18}$$

The next step consists in computing the radiated field from the induced currents. Then, we can start from the wave equation which can be obtained by eliminating $\mathbf{H}$,

by taking the curl of Eq. 2.9 and then using Eq. 2.10.

$$\nabla \times \nabla \times \mathbf{E} + k^2 \mathbf{E} = j\omega\mu\mathbf{J} \tag{2.19}$$

where k is the wave number. So, using the concept of the Dyadic Green's function, $\bar{G}$, which satisfy

$$\nabla \times \nabla \times \bar{G} + k^2 \bar{G} = \bar{I}\delta(\mathbf{r} - \mathbf{r}'), \tag{2.20}$$

and $\bar{I}$ is a unit dyad that can be represented by a unit diagonal matrix [36]. Through the superposition principle for linear problems, the radiation fields can be formulated as the convolution of the dyadic Green's function with $\mathbf{J}(r)$ as

$$\mathbf{E}(\mathbf{r}) = j\omega\mu_0 \iiint \bar{G}(\mathbf{r}, \mathbf{r}') \cdot \mathbf{J}(\mathbf{r}') d\mathbf{r}'. \tag{2.21}$$

Therefore, the scattered field can be written

$$\mathbf{E} - \mathbf{E}^{inc} = \mathbf{E}^{sc} = j\omega\mu_0 \iiint \bar{G}(\mathbf{r}, \mathbf{r}') \cdot \mathbf{J_e}(\mathbf{r}') d\mathbf{r}' \tag{2.22}$$

However, it should be noted that the right-hand side of the below equation cannot be computed yet, since the induce current $\mathbf{J_e}$ depends on the electric field $\mathbf{E}$. For further details on the formulation of the inverse scattering problem refer to [36].

S-parameter Data Equation

Until this point, we worked with field values. However, these are sampled via the S-parameter recovered from the antennas in a real system. These describe the performance of the microwave (MW) devices in terms of the incoming and outgoing port waves, named a_n and b_n, respectively. Thus, deriving their respective Green's vector enables the construction of the S-parameter data equation, which is vital for the retrieval imaging algorithm.

Considering the Green's vector function $\mathbf{E}'_{inc}$ associated with the outgoing power wave b_i at the i-th (receiving) port of a MWI network, which serves as the kernel for the scalar-response integral equation. So, knowing the Green's vector function, b_i is the response to the source function $\mathbf{J}$ as

$$b_i = \iiint \mathbf{E}'_i(\mathbf{r}') \cdot \mathbf{J}(\mathbf{r}') dv' \tag{2.23}$$

Then, because in imaging we are interested in the scattering component of outgoing wave, $b_{i,sc}$, due to the induced sources of scattering $\mathbf{J}_e$. Hence,

$$b_{i,sc} = \omega^2 \mu_0 \iiint \chi_e(\mathbf{r}') \mathbf{E}_i'(\mathbf{r}') \cdot \mathbf{E}(\mathbf{r}') dv', \tag{2.24}$$

being $\mathbf{E}$ the total internal field.

After that, the Green's vector function for b_i is obtained using the generic formula Eq. 2.20 for the auxiliary source generating Green's vector function and the relationship between the outgoing wave and the field solution, as

$$\mathbf{E}_{inc}' = \frac{\mathbf{E}_i^{inc}}{j\omega\mu_0 2a_i}, \tag{2.25}$$

where $\mathbf{E}_i^{inc}$ is the field generated from the i-th port when it is excited by a_i.

Finally, to obtain an expression for the S_{ij} parameter may be joined the Eq. 2.24 and Eq. 2.25, obtaining the base equation for our algorithm of imaging [37],

$$S_{ij}^{sc} = \frac{-j\omega}{2a_i a_j} \iiint \chi_e(\mathbf{r}') \mathbf{E}_i^{inc}(\mathbf{r}') \mathbf{E}_j(\mathbf{r}') dv'. \tag{2.26}$$

2.3 Live-tracking Imaging Algorithm

This section outlines the image reconstruction procedures based on frequency-sweep measurements, i.e. the multi-frequency scattering parameters collected via the microwave antenna array in a multi-view scheme as shown later in Ch. 3, to obtain a complex contrast mapping in real-time, a 3-D image, of the imaged volume.

The imaging algorithm used here is projected for an imaging-based follow-up of a brain stroke condition in almost real-time. Then the algorithm outputs contrast maps indicating the physical temporal variation, i.e. location, and estimated shape, that occurs during two different studied clinical scenarios. Figure 2.3 depicts a general scheme of the procedures, where on top is indicated imaging part, and at the bottom a simplified and illustrative view of the calibration procedures, which is studied in Sect. 2.4.

The MWI algorithm searches for the unknown dielectric contrast distribution by processing the measured data, differential S-parameters, ΔS, through a well-

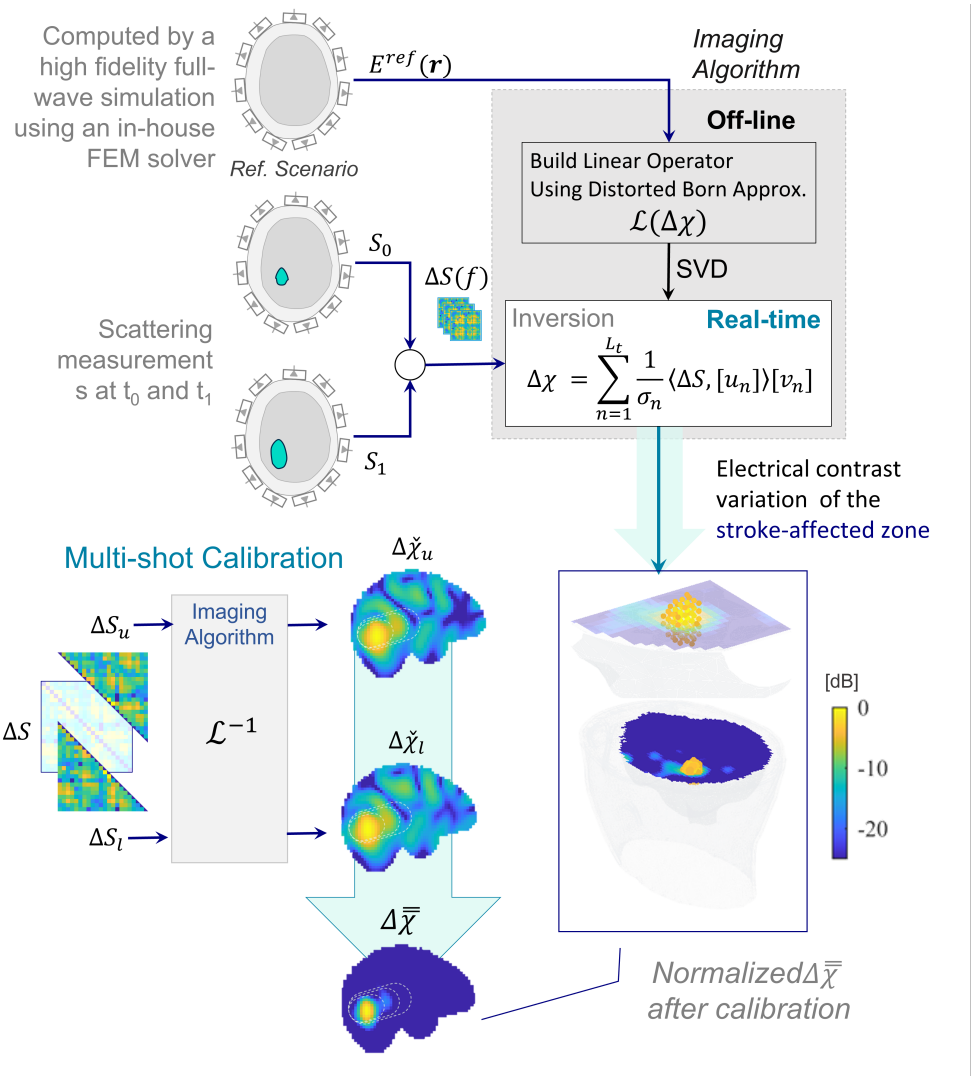

Fig. 2.3 Differential imaging algorithm scheme.

assessed approach, based on the singular value decomposition (SVD) of the imaging kernel operator, which describes the EM scattering problem [35]. ΔS represents the sensitivity response of the imaging device to the gradient in the space of the stroke-affected area, e.g., the shape and/or its constitutive parameters. It is obtained by subtracting the measured $N \times N \times f_n$ S-parameters matrix at two different time instants, t_0 and t_1 (see Fig. 2.3:top), as a differential scattering matrix, where N stands for the number of transceivers, antennas, and f_n for the number of frequency points considered.

Moreover, because we are dealing with a reciprocal network, ΔS is expected to be symmetric as the imaging domain, the head, is composed of living tissues (electrically mimicked during the experimental validation), i.e. linear matter whose constitutive parameters do not depend on the field strength, and the antennas are not integrated with nonlinear detectors and/or amplifiers. Thus, in an N-port network, only $N(N+1)/2$ S-parameters are independent, representing the upper/lower triangular part of ΔS. Though, because we do not employ the reflection self elements for the imaging, further explained in Ch.3, the number of independent parameters is reduced to $N(N-1)/2$.

In the specific, we approach the whole imaging algorithm as both an off-line and heavy computational part where the imaging kernel is generated and decomposed, but just done once, and an online (fast) part facing the inversion and calibration procedures.

2.3.1 Off-line Procedures

The inverse scattering problem acts as a parameter-identification problem that aims to determine the nature of an unknown scatter i.e. its location, shape, and material. Thus, in the imaging-based brain stroke monitoring the output is associated with the spatial distribution of the normalized contrast variation within the head between t_0 and t_1,

$$\Delta\chi(t_0,t_1) = \frac{\varepsilon(t_1)-\varepsilon(t_0)}{\varepsilon_b}, \tag{2.27}$$

where ε is the complex permittivity distribution, and b indicates a reference background scenario. Hence, the sensitivity response is represented by the frequency-domain analytical formula in Eq. 2.28 (rewritten version of Eq. 2.26), i.e., it does not depend on the particulars of the numerical method or the simulator, indicating the scene variation with respect to a constitutive or shape object parameter and the field distribution [37].

$$\Delta S(t_0,t_1) = -\frac{j\,\omega\,\varepsilon_b}{2\,a_p\,a_q}\int_D \mathbf{E}_p(t_0)\cdot\mathbf{E}_q(t_1)\,\Delta\chi\,d\mathbf{r}, \tag{2.28}$$

where D is the volume of the domain of imaging, j is the imaginary unit, $\omega = 2\pi f$ is the angular frequency, and a_p and a_q are the incoming root-power waves given at the p-th and q-th antenna ports, respectively (See Fig. 2.2). Moreover, the symbol "$\cdot$"

denotes the dot product between the nominal electric field vectors $\mathbf{E}_p(t_0)$ and $\mathbf{E}_q(t_1)$, i.e. the fields radiated by the p-th and q-th probe inside D at the respective state, respectively.

Eq. 2.28 represents a non-linear problem, which can be solved by iterative methods posing the problem as an optimization problem as shown in Fig. 2.4. Then, in each iteration the algorithm minimizes the mismatch between measured and predicted data by adjusting the unknowns used by the prediction. Examples of these methods are the Distorted Born Iterative Method (DBIM) and the Contrast Source Inversion (CSI)[36]-Ch.6, which are used to retrieve the electrical properties of the studied domain in a quantitative way. However, iterative methods have the drawback that requires solving the forward problem, the heaviest computational part, in each iteration. Therefore, these are not convenient for the targeted real-time application. Also, the non-linearity of the problem is a non-convex one. Thus, the optimization may get trapped in false solutions, i.e., local minimum.

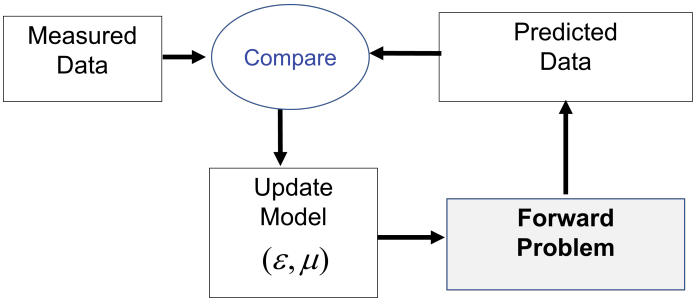

Fig. 2.4 Iterative full inverse scattering imaging scheme

Another way to solve the nonlinear problem is to linearize it, considering a "weak" and localized scatter, approximating the problem to a linear one. In this case, the solution has less information but can work in specific cases. Fortunately, these conditions are fulfilled by our problem. For the application target here, a brain stroke and controlled time-variable examination, which means a small EM perturbation between scenarios, t_0 and t_1, the distorted Born approximation is employed to linearize the formulation. Then, the forward formulation of the problem can be rewritten as Eq. 2.29, where the field distributions at t_0 and t_1 are replaced by nominal reference one, $\mathbf{E}^{ref}$. It consists here, of a scenario representing the head as a single-tissue organ with the average complex permittivity of a brain.

$$\Delta S(t_0,t_1) = -\frac{j\,\omega\,\varepsilon_b}{2\,a_p\,a_q}\int_D \mathbf{E}_p^{ref}\cdot\mathbf{E}_q^{ref}\,\Delta\chi\,d\mathbf{r}, \tag{2.29}$$

Then, the linear imaging system may be represented in a compact mathematically format as Eq. 2.30, where $\mathcal{L}$ is the linear operator from the object space into the image space, and w is an element of the latter describing the noise contribution due to the measuring. This operator describes the system's response to a point scatter as a function of the observation position, forming the so-called point-spread function (PSF) of the imaging system, which has intrinsically associated a smoothness attribute related to the loss of information during the translation of domain. In a practical scenario, PSF is an indicator of the resolution of the system.

$$\Delta S = \mathcal{L}\{\Delta\chi\} + w, \tag{2.30}$$

Moving to the implementation, it is clear from Eq. 2.29 that to resolve the problem is needed to have the a-priori information of the electric field of the reference. So, to obtain the fields vectors E^{ref}, in Eq. 2.29, we compute them via a highly realistic EM full-wave simulation of the reference scenario using an in-house 3-D Finite Element Method (FEM) solver and 3-D CAD models, for details see Ch. 3[38, 39]. The solver applies the curl-curl formulation for the electric field and Galerkin testing and discretizes the whole domain in a tetrahedral mesh. The metal elements, e.g. within the antenna, are considered perfect electric conductor (PEC) surfaces, and the dielectric sub-volumes, e.g. the head and dielectric parts of the antenna, are modeled with the respective complex permittivity. Moreover, the antenna feeding, which is a crucial part of accurately calculating the scattering parameters, is modeled as a section of a rigid coaxial cable [39]. This part of the imaging process is the most time-consuming and computationally expensive, which requires dealing with matrices in the order of millions of elements, defined by the meshing. Though, it is an off-line process that is only required once in our algorithm.

After obtaining the reference multi-frequency E-fields, the imaging kernel is built by applying a singular value decomposition (SVD) to the discretized integral operator. Here, it is worth mentioning that in order to reduce the size of the operator and make it compatible with the post-processing algorithm of imaging that works on Cartesian meshes, fields are interpolated into a 3-mm side Cartesian mesh placed around the upper part of the head. Also, considering the aforementioned symmetrical aspects of the problem, the elements of the field matrix concerning are removed. As a result, the decomposed operator, $\langle [u], [\sigma], [v] \rangle$, obtained via the SVD of the

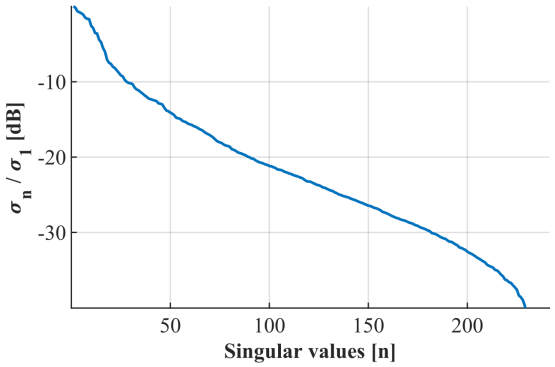

Fig. 2.5 Singular values of the multi-frequency operator.

discretized operator $\mathcal{L}$, can be pre-loaded on the laptop running the imaging, where σ_n, u_n and v_n are the n-th singular value, right and left singular vectors, respectively.

2.3.2 Real-time Procedures

The real-time (live) procedures of the imaging denote the inversion mechanisms, Though, the calibration and recovery tracking techniques described in the next sections can be also considered live procedures. The inversion provides the contrast distribution expressing it as the projection of the ΔS onto the decomposed discretized integral operator as described in Eq. 2.31, where truncation index T acts as a regularizer parameter [35]. Even though the inversion uses a multi-frequency, it does not invert the problem frequency by frequency using an individual operator by frequency point, instead, the inversion is done at once via a single extended operator that includes the multi-frequency responses concatenating each frequency contribution with the others in single extend matrix.

Then the imaging algorithm exploits the simplified linear approximation of the problem to resolve the problem in a single iteration, ensuring fast reconstruction times. Indeed, once the compute-intensive building of the linear operator is completed offline, the imaging task is achieved in a few seconds. Fig. 2.5 shows the normalized singular values of the imaging operator obtained for the second version of the system, where the T parameter has been set to -30 dB. An equivalent figure for the first version of the system is reported on [40].

$$\Delta\chi = \sum_{n=1}^{T} \frac{1}{\sigma_n} \langle \Delta S, u_n \rangle v_n, \tag{2.31}$$

Here, it is worthy to recall that using this technique the amount of information would be limited. So, it is not expected that it can arrive directly at the actual constitutive values of complex permittivity, as an iterative method does. However, the retrieved information contains enough information to be able of determining and indicate qualitatively:

- **Detection of a contrast variation** indicates if there was a change in the stroke-affected area with respect to a first measured scenario.
- **Localization** signals the position within the head of the variation, which is vital from the medical point of view.
- **Shape retrieval** presents graphically the volume variation.
- **Contrast sign** is a parameter that may indicate the clinical change of state of the stroke-affected area.

The output image is usually reconstructed as the normalized modulus of the complex differential contrast (see Fig. 2.3), indicating qualitatively the estimated location and shape of the stroke variation. However, the real and imaginary parts may also be evaluated separately, aspects exploited later for the tracking of recovery status.

2.4 Multi-shot Calibration

Once one moves to the practical validation of an MWI prototype, a very complex system, one may find the algorithms, previously tested in ideal(virtual) scenarios perform worse or do not work. This could be due to many reasons and factors. For instance, the experimental performance would be degraded due to the lack of imaging kernel fidelity in comparison with the actual system, e.g., an operator assuming that the fields in the MWI system arise from point sources, plane waves, or other idealized sources, instead of the ones generated by the used antennas. Hence, to reduce this kind of degradation, one solution is to use high-fidelity full-wave simulations that

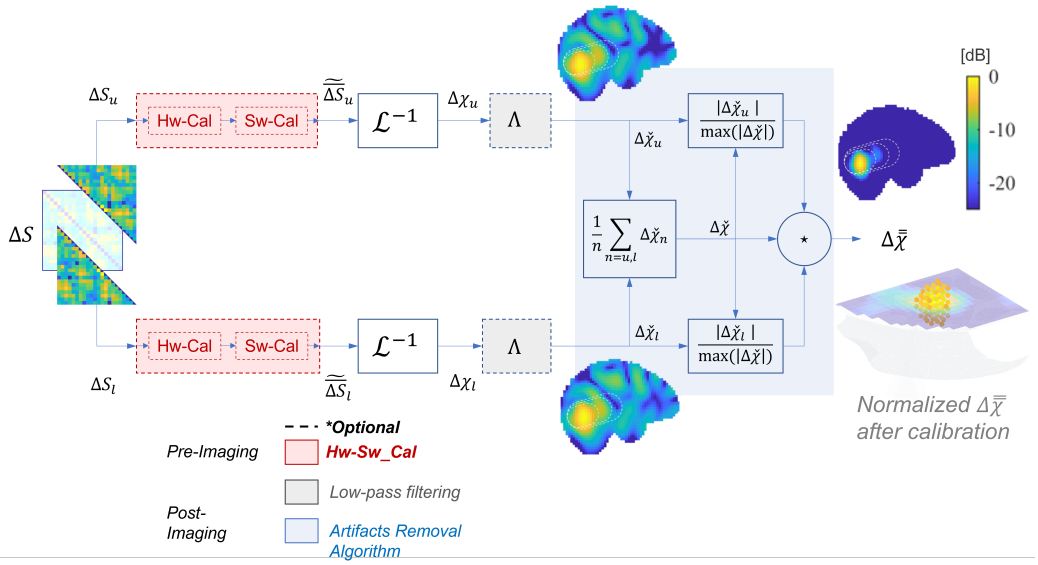

Fig. 2.6 Multi-Shot calibration scheme.*Note that even if the slide views are normalized version of the contrast, the method actually works on complex values.

consider and model all these effects as we see later in Ch. 3-4. Though, even using accurate modeling and reliable EM solvers, the system model might not reflect the actual due to manufacturing tolerance of the components, inclusion of additional components as a switching matrix, noise, non-controlled environmental variations, etc.

A complex and distributed system such as MWI prototype make introduce an enormous systematic error, thus, the differential nature of the algorithm is the first intrinsic calibration that deals with those. When the scattering difference is applied, we remove to some extent this kind of error. However, even after the differentiation, the remaining non-modeled stuff affects negatively the obtained images.

Therefore, to deal with mentioned experimental degradation, it is proposed to use a real-time multi-shot calibration scheme, illustrated in Fig. 2.6, which substantially reduces artifacts on the reconstructed images, increasing only marginally the computational burden. In a general view, the calibration mechanisms are divided into two families, pre-and-post imaging thus applied as is indicated by their names, and further explained in the following sections. In a general view, the multi-shot name refers to different kinds of calibrations, concatenated, and can be applied at different instants. Though, not all have to be applied always to get good results, so retrieving the meaningful information from the raw data.

2.4.1 Pre-Imaging Calibration

This section describes calibration mechanisms applied on the measured S-parameter directly attempting to mitigate the effects of multiplicative errors using two different strategies. On the one hand, the Hw-Cal aims to compensate for non-modeled temporal variation happening during the measuring period. On the other hand, it is the Sw-Cal, which attempts to calibrate the data to the inverse model.

De-embedding the Data

As it will be explained in more detail in the implementation chapter, to measure the whole scattering matrix of the multi-port system with a 2-port VNA, we use a switching matrix sequentially multiplexing signals. At the same time, a script builds the entire matrix. However, the introduction of the matrix adds non-modeled features to the imaging kernel, which assumes the face of the coaxial as the phase reference plane. Then, to render more faithful the measured S-parameters to the numerical ones, we applied a de-embedding aiming to remove mainly the phase shift to the VNA reference (pre-set with the 3-standard VNA calibration) added by the internal path within the switching matrix and coaxial cables connecting the antennas.

Before applying the multi-shot calibration, a pre-stage of data adjusting is applied to the raw measured S-parameters to render them close to the nominal condition, defined in the operator. In other words, we want to report the reference phase of the measure to the antenna ports, which is shifted due to the path through the switching matrix that connects the 2-port Vector Network Analyzer (VNA) with the receiving/ transmitting (RX/TX) antennas, as shown in the system diagram in Fig. 2.7. Ideally, at this point, a standard multi-port VNA calibration would resolve the problem, but it is high time-consuming requiring connecting and disconnecting the antennas multiple times before each operation set. Then, we opt for, first, off-line characterization of each channel, i.e. coaxial cables, electromechanical switches, and cable connectors, and then, remove their phase-shifting effect via de-embedding. Regarding the attenuation, it has been experimentally observed that the path introduces slight attenuation of the signal (no more than 2 dB).

In particular, it follows the procedures reported in [41], where, for each pq-antenna pair, the measured scattering matrix at the VNA ports, S^{pq}, includes the scattering matrix of the left path (from the VNA port to p-antenna port), S^{p}_{L}, the

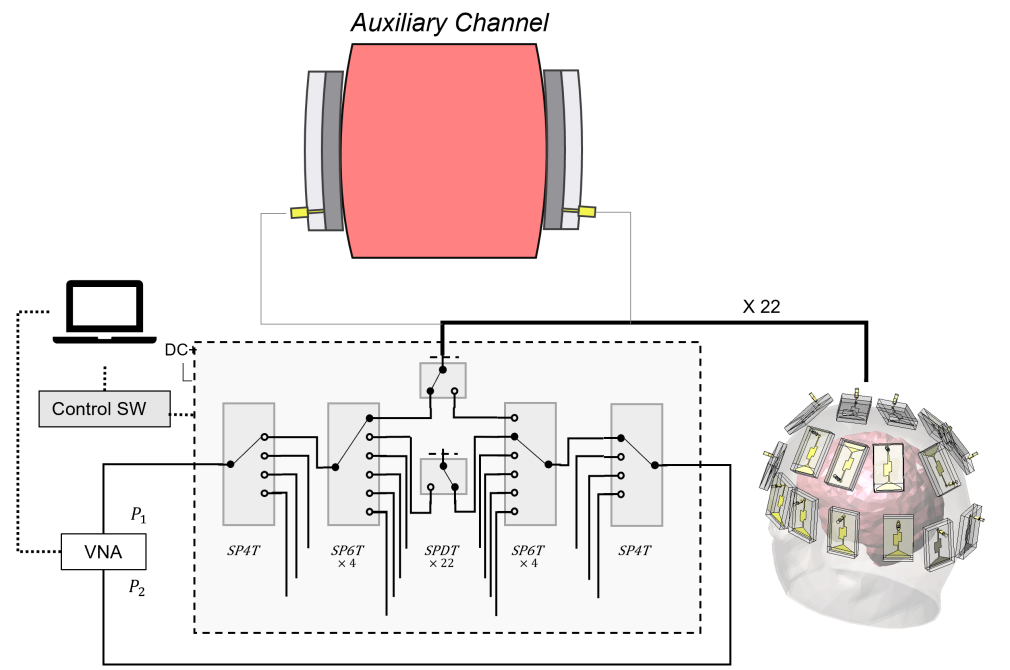

Fig. 2.7 MWI system scheme with auxiliary channel.

scattering matrix at the antenna ports, S^{pq}_{DUT}, and the scattering matrix of the right path (from the q-antenna port to the VNA port), S^{q}_{R}. Considering the corresponding transmission matrices, T^{pq}, T^{p}_{L}, T^{pq}_{DUT}, and T^{q}_{R}, respectively, the following represents their relationship:

$$T^{pq} = T^{p}_{\mathrm{L}}\, T^{pq}_{\mathrm{DUT}}\, T^{q}_{\mathrm{R}}. \tag{2.32}$$

Thus the T^{pq}_{DUT} can be retrieved as

$$T^{pq}_{\mathrm{DUT}} = (T^{p}_{\mathrm{L}})^{-1}\, T^{pq}\, (T^{q}_{\mathrm{R}})^{-1}, \tag{2.33}$$

and, finally, rewritten as a scattering matrix, S^{pq}_{DUT}, whose amplitude and phase are now compensated. The de-embedding stage is essential to recover the real and imaginary parts of the dielectric contrast, which is required to characterize the dynamic behavior of the stroke as described in the following section.

HwSw Calibration

The accuracy of the input differential scattering matrix, built with the measured at different time instants, impacts the quality of the generated reconstructions directly.

However, in real-world circumstances, disturbances may contaminate the input data, lowering the system's total performance. So, in the following, two calibration strategies are provided to limit the undesirable measured data deterioration and improve the reconstructed images.

The first calibration scheme is dubbed in the following "hardware calibration" (Hw). It attempts to compensate for multiplicative inaccuracies in scattering transfer parameters across all antenna pairs owing to measurement uncertainties and performance changes due to ambient circumstances (such as room temperature fluctuations) or drift errors in the VNA and/or switching matrix. We move from the assumption that $\Delta S_{p,q}(t_0,t_1)$, where p and q indicate the antenna index and instant times t_0 and t_1 refers to the measuring times, is only associated to the contrast variation on DOI. Then, *Unwanted* additional variations due to changes over time on the measurements, which can corrupt the input data and thus possibly hide the *searched* variation, can be modeled as

$$\Delta S_{p,q}(t_0,t_1) = S_{p,q}(t_0) - S_{p,q}(t_1) = \alpha\,\bar{S}_{p,q}(t_0) - \beta\,\bar{S}_{p,q}(t_1), \tag{2.34}$$

where $\bar{S}_{p,q}(t_0)$ and $\bar{S}_{p,q}(t_1)$ correspond to the ideal measured scattering parameters in a scenario without inaccuracies, i.e. the ideal input data for the imaging algorithm, and α and β are complex unknown coefficients modeling the possible data multiplicative inaccuracies due to measuring, at time instants t_0 and t_1, respectively, with respect to the ideal ones.

Then, to collect enough information to compute these coefficients, we use the transmission coefficients measured in the reference channel. It consists of a couple of antennas, facing each other, placed on the sides of a simplified head model made of a container filled up with a liquid mimicking the dielectric properties of an average brain. In this case, no variation is applied to the scenario, and the transmission coefficient in the reference channel, measured in the same time instants t_0 and t_1, can be written using the same notation as $S^{\mathrm{REF}}(t_0) = \alpha\,\bar{S}^{\mathrm{REF}}(t_0)$ and $S^{\mathrm{REF}}(t_1) = \beta\,\bar{S}^{\mathrm{REF}}(t_1)$, where we know that $\bar{S}^{\mathrm{REF}}(t_0) = \bar{S}^{\mathrm{REF}}(t_1)$ because the *not* change. Thus, the calibrated differential scattering parameters, $\overline{\Delta S}_{p,q}(t_0,t_1)$, correspond to the difference of the ideal corresponding scattering parameters as in Eq. 2.35, where the multiplication factor $1/\alpha$ can be neglected because it is in common for all the

antenna pairs.

$$\begin{aligned}\overline{\Delta S}_{p,q}(t_0,t_1) &= \bar{S}_{p,q}(t_0) - \bar{S}_{p,q}(t_1) \\ &= \frac{1}{\alpha}\left[\alpha\,\bar{S}_{p,q}(t_0) - \frac{\alpha}{\beta}\,\beta\,\bar{S}_{p,q}(t_1)\right] \\ &= \frac{1}{\alpha}\left[S_{p,q}(t_0) - \frac{S^{\mathrm{REF}}(t_0)}{S^{\mathrm{REF}}(t_1)}\,S_{p,q}(t_1)\right] \end{aligned} \tag{2.35}$$

The second calibration, termed "software calibration" (Sw), attempts *tunning* the measured scattering parameters using syntactical ones, obtained numerically. Hence, this technique proposes to use the scattering parameters of a known scenario, numerically and experimentally, to calibrate the differential input data of the imaging algorithm. In this case, we consider the healthy head, without the stroke, as know scenario. Hence, applying both hardware and software(Hw-Sw), the calibrated scattering data is expressed as

In addition to the described Hw calibration, a second calibration, dubbed in the following "software calibration" (Sw), can be also applied. Its aim is to *tune* the measured scattering parameters with the system numerical modeling [39] used to generate the discretized scattering operator in Eq. 2.31 The basic idea is to consider the same known scenario in both the numerical modeling and the real system [42]. The scattering data, measured and simulated in the known scenario, are then used to calibrate the scattering matrices, measured at different time instants, in the scenario under test (that can be a real-world one). Here, we consider as known scenario the head under test in healthy conditions, i.e. without the stroke. Hence, the hardware and software (Hw-Sw) calibrated differential scattering parameters can be written as

$$\widetilde{\overline{\Delta S}}_{p,q}(t_0,t_1) = \frac{\tilde{S}^{\mathrm{H}}_{p,q}}{S^{\mathrm{H}}_{p,q}}\,\overline{\Delta S}_{p,q}(t_0,t_1), \tag{2.36}$$

where $\tilde{S}^{\mathrm{H}}_{p,q}$ and $S^{\mathrm{H}}_{p,q}$ are the simulated and measured scattering parameters, for the generic p,q antenna pair, in the case of the healthy scenario, respectively.

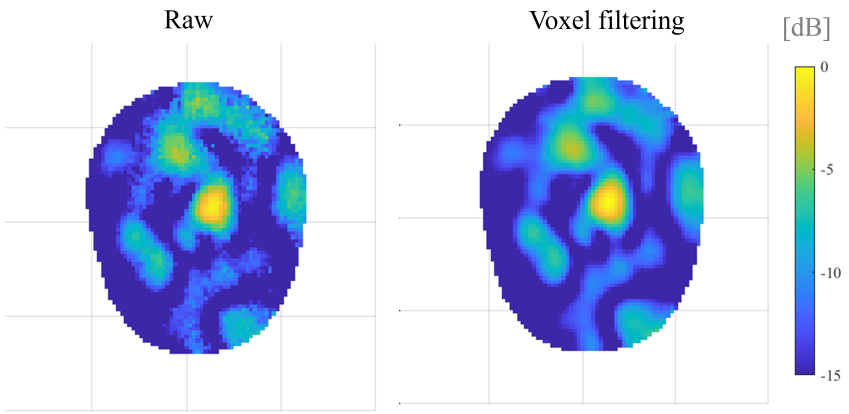

Fig. 2.8 Reconstruction applying and without applied voxel filtering.

2.4.2 Post-Imaging Calibration

Low-pass Filtering the imaging

This calibration applies a low-pass filtering technique, traditional in imaging processing, extending it to a 3-D concept. The reason behind this is to remove the outlier from the mapping, that offsets the normalized visualization, hiding the information of interest. Moreover, it is also smooth and give a more natural finish to the images as shown in Fig. 2.8.

This technique is applied directly to the retrieved contrast when this used a cubic-based voxel mesh, though if the mesh has a different kind of mesh element as a tetrahedral, has to be interpolated first. Indeed, for the preliminary presentation of this technique in [43], it includes the additional step of the interpolation. Once the data is interpolated in the required mesh to apply the 3-D average window filter, it is applied as illustrated in Fig. 2.9 , where the voxel in blue is averaged with its neighbors. Thus, depending on the voxel's position in the domain, it enters one of the depicted cases. Though, most of the voxels consider its 26 closest surrounding neighbors.

Artifacts Removal Algorithm

This is the core of the post-imaging calibration, being jointly a powerful, novel, and non-complex technique that deals with the artifacts consequence of error propagation

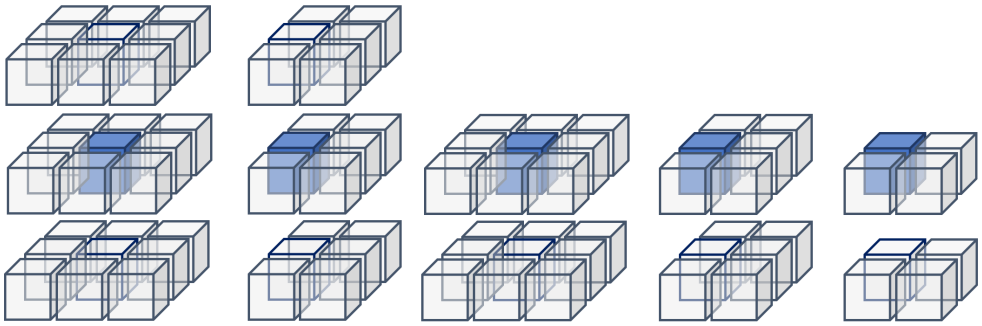

Fig. 2.9 Volxel filtering considering the different vicinity configurations. The blue voxel indicates the filtred one.

and amplification from the data solution to the solution, which is deprived of physical meaning. This is also the result of neglecting the w in Eq. 2.30, so that the range of the operator $\mathcal{L}$ does not include the noisy images.

The preliminary idea of the multi-shot calibration was presented in [43], taken it named of the fact it can concatenate different calibration approaches to generate a couple of twin images, as briefly illustrated at the bottom of Fig. 2.3. However, in [43], the technique was projected using two different sets of measures for each of the differential states, despite here, the updated version of the calibration does not require an additional set of measures, while exploits the symmetric nature of the problem. The calibration starts with the assumption that input S-parameters are symmetric, so the information contained in each of the either upper or lower is the same. Therefore, the retrieval image made from the upper part of the differential S-matrix must be identical to the one retrieved using the lower part, instead. However, the assumptions are not fulfilled in real-life experimentation due to different factors. Firstly, the noise generates unwanted spurious signals that even after the regularization, may cause artifacts in the reconstructed images. Secondly, though, the paths are designed to have the same electrical length, there have small symmetrical discrepancies due to the internal switches, the connectors attachments, and the coaxial cables, i.e. for a measure at t_n the corresponding $S_{i,j} \neq S_{j,i}$. Thus, considering the latter, the multi-shot calibration here will pair always the respective upper/lower part of the S-matrix at t_0 with its corresponding partner at t_1, ensuring that the pair share the same non-pre-calibrated path effects. Then, the calibration considers that the differences between images, generated with either the upper or lower part of the differential

matrix, are actually due to random processes that can be removed leaving only the information of interest.

Now, starting from the twin images, for instance, $\Delta\chi_u$ and $\Delta\chi_l$ in Fig. 2.3, we compute the average among the different retrieved contrasts as in Eq. 2.37, where the mathematical expression in the following is stated in a general way because, theoretically, it could extend to a greater number of combinations with a better pre-calibration of the data.

$$\Delta\bar{\chi} = \frac{1}{2}\sum_{n=u,l}\Delta\chi_n \tag{2.37}$$

Then, we apply a kind of mutual spatial-band filter multiplying, projecting, twin the normalized twin contrast as described in Eqs. 2.38 and 2.39, where the final contrast with removed artifacts is referred as $\Delta\bar{\bar{\chi}}$.

$$\Delta\tilde{\chi}_n = \frac{|\Delta\chi_n|}{max(|\Delta\bar{\chi}|)} \tag{2.38}$$

$$\Delta\bar{\bar{\chi}} = \Delta\bar{\chi}\prod_{n=u,l}\Delta\tilde{\chi}_n \tag{2.39}$$

The final averaging acts similarly to the MUSIC algorithm, but here instead of overlapping between frequency responses, it uses the response to different reconstructions of the same scenario, at the close-by instant, at the same frequency. Also, it bears similarities to traditional averaging used by VNAs to improve their Signal-to-noise-ratio (SNR)[44]. Still, in this case, it is considered the noise propagation on the imaging algorithm.

2.5 Recovery Tracking

Considering the normalized/non-normalized magnitude of the retrieved contrast after the imaging, one is able to build an intensity map. Thus the map may indicates the mentioned parameters of shape and location of the contrast variation. However, looking into the images, it is not possible determines the direction of the variation. In other words, the qualitative contrast of a big stroke at t_0 that evolves to smaller one at t_1, would be equivalent to the one obtained from the inverse situation, small stroke at t_0 and bigger at t_1. So, with this preliminary information, the medical stuff cannot identified if the stroke is growing or shrinking.

To deal with this issue, we recall the dielectric contrast definition (Eq. 2.27), noticing the sign of the real part of $Re(\Delta\bar{\bar{\chi}})$ might depend on two factors in the case of brain stroke monitoring. First, the order of subtraction terms, and second, the type of stroke. The latter considering the fact that hemorrhagic zone, mostly blood, has higher permittivity than its surrounding healthy brain tissues (either gray and white matter). Conversely, an ischemia present lower values.

In this simple scenario, the real-part sign will have two degrees of freedom. Therefore, in the case one knows already the type of stroke at the moment of start the monitoring, which is highly probable in a follow-up situation, the unknowns determining the evolution sense reduce to one. Then, adopting a positive convention to indicate the stroke is spreading and a negative one in the case is reducing, we can determine this pathological parameter as

$$\phi = st\frac{Re(\Delta\bar{\bar{\chi}})}{|max(Re(\Delta\bar{\bar{\chi}}))|}, \tag{2.40}$$

where *st* takes the value of 1 in a HEM case, and -1 in an IS case.

Chapter 3

Methods

This chapter approaches the development of the MWI prototypes by planting the basis of the EM modeling initially, getting on the fundamentals of the Finite Element Method used for producing most of the numerical tests. Also, this first part comment on aspects in the actual application of the FEM to execute high-fidelity full-wave EM simulations that generate a reliable electric field used for building the imaging kernel and the scattering parameter of the virtual trials. The section discusses the design guidelines used to develop the MWI prototype. Then, the second section moves on to implementing all the different modules of the prototype. Here is discussed the design of the two microwave antennas used in each of the system versions. It closes by detailing the procedures to set up representative clinical scenarios in a lab environment, using a realistic anthropomorphic phantom filled with liquids mimicking the properties of the head. Finally, the last section describes the experiments used later to validate the system both numerically and in real life.

3.1 On the EM Modeling of a MWI system

In MWI, faithful and accurate modeling is a fundamental stone of the development and functioning of the system. It is transversal to all prototyping stages covering from the design to the validation of the device. Indeed, it can be considered a catalyst that speeds up the whole device development, reducing the times significantly at each stage by providing meaningful information supporting the validation stages' analysis. This section collects all the different pieces on the ideation, building, and validation

that are linked in some aspects with the EM modeling of an MWI system. First, the fundamentals of the leading used EM solver, an in-house FEM, are described, then finishing with a description of how it models the system using the FEM and the design guidelines.

3.1.1 The Finite Element Method

Considering the core of the numerical validations of this thesis is performed using an in-house EM Finite Element Method(FEM) solver, this section introduces, first, the concepts and rudiments behind it (for a detailed development of the method refer to [45]) and then describes its application in case of realistically full-wave modeling the MWI system.

As mentioned in the chapter about the imaging algorithm, to solve the inverse problem, it needs to build the imaging kernel (operator), which within the possibilities adds as much as feasible apriori information about the MWI system and, in general, the studied scenario. Hence, discarding the option of building the kernel using measures of the SPF of the system due to its intrinsic technical difficulties makes it unpractical in the studied scenario. The practical alternative is to model the system and obtain analytically or numerically the required fields and scattering parameters. Though the analytical solutions are desirable because their exact solutions, these only can be obtained for a few particular problems, then let us with the numerical option. The numerical modeling approximates the solutions, specifically Maxwell's equations in our application case. Though, the electromagnetic simulators or field solvers are the most versatile and effective way of approach complex problems in our days, reaching accurate and reliable solution as long as the problem is well set up. For instance, in our case, they provide accurate EM fields of the scenario under test used to build the operator and scattering parameters at the antenna ports.

The numerical option approximates the exact solutions as closely as possible, for example, by following procedures known as the method of weighted residuals (MWR)[46], which has been developed for solving linear and nonlinear differential equations, and which FEM is part of. FEM is a numerical technique used to obtain an approximated solution to boundary-value problems describing mathematically physic scenarios, which beginnings go back to the 1950s. Historically, it was devised to perform structural analysis, though the electromagnetism community

has already used it for more than three decades. The method's versatility lies in adapting to systems described and governed by either differential or integro-differential equations, such as the Maxwell's equations and derivation, integral, with the form:

$$\mathcal{L}\phi(r,\omega) - f(r,\omega) = 0, r \in \Omega, \tag{3.1}$$

defined in a domain Ω, which can be a boundary contour, a surface, or a 3-D volume, and with boundary conditions on the boundary Γ, enclosing the domain. $\mathcal{L}$ is the operator, ϕ is the unknown quantity, signal or field function to be determined, f is the excitation or forcing function, r is the space vector, ω is the angular frequency, that changes to t for time domain solutions. In electromagnetics, the form of the governing equations might range from the Poisson equations to the vector wave equation, used here. Also, the boundary condition can consider the Dirichelet and Neumann conditions, or even more complicated higher-order ones.

Maxwell's equations have solutions that are functions of space, time, or frequency, which projective representation occurs in function space, also called "inner product space." Known basis or expansion functions with unknown coefficients span the function space. The solution method, MWR, is then to discover the values of these coefficients so that the resulting linear combination or expansion approximates the precise solution through two consecutive phases. The first one expresses the unknown solution as a sum of known (pre-selected) basis or expansion functions with unknown expansion coefficients. The second identifies the coefficients that render the approximation close to an accurate solution.

Therefore, MWR comprehends the function expansion and the determination of the unknown coefficients by minimizing the so-called residuals with another function expansion. The procedure starts with the approximation of $\phi(r,\omega)$, unknown solution, to a trial function, $\tilde{\phi}(r,\omega)$, expanded in a set of pre-selected basis functions $u_n(r,\omega)$ as bellow, where a_n are the expansion coefficients.

$$\phi(r,\omega) \approx \tilde{\phi}(r,\omega) = \sum_{n=1}^{N} a_n u_n(r,\omega). \tag{3.2}$$

Then, it defines the residual error $R(r,\omega)$ as by substituting the approximated solution($\tilde{\phi}$) in Eq. 3.1, the original operator.

$$\mathcal{L}\tilde{\phi}(r,\omega) - f(r,\omega) = R(r,\omega), r \in \Omega. \tag{3.3}$$

Continuing with the procedure, in the next step one chooses a set of weighting (or testing) functions that expand the residual function, and then equal it to zero. Here, the method is called as Bubnov–Galerkin procedure, or just Galerkin, if the weighting functions and basis functions are selected the same.

$$\langle R(r,t), w_m(r,t) \rangle = 0. \tag{3.4}$$

Finally, replacing the approximated trial function Eq. 3.3 into the inner product Eq. 3.4, and applying its properties, we obtain a linear system of equations as expressed bellow in Eq. 3.5. Therefore, the approximated solution, Eq. 3.2, is reached once a_n coefficients are found since the expansion functions and their coefficients are known at this point.

$$\sum_{n=1}^{N} a_n \langle \mathcal{L} u_n, w_m \rangle = \langle f, w_m \rangle. \tag{3.5}$$

Now that MWR procedure is described, we can abstract it to the FEM case, when the aim is to resolve boundary-value problems replacing an entire continuous domain by a finite number of subdomains in which the unknown function is changed by simple interpolation functions with unknown coefficients. FEM thus resolves the original boundary-value problem by an approximated solution with a finite number of unknown coefficient. Then the system of equations can be obtaining, for instance, applying the Galerking procedure, and the final solution by solving this system. Summarizing, the FEM follows:

- **Discretization of subdivision of the domain** This is probably the mos important part of the FEM procedures, because the way in which is done affect directly the computer storage requirements, the computation time and the results accuracy. Here the whole domain of the problem ω is splitted into smaller domains, stated as $\Omega^e (e = 1, 2, 3, \cdots, M)$, where M denotates the number of subdomains, which are typically referred as elements. For instance, in a one-dimensional domain, the elements are usually short line segments, in a two-dimensional one the elements are small triangles and rectangles, and in a third-dimensional are tetrahedra, triangular prisms, or rectangular bricks. In this work, we use tetrahedra because are the simplest and best suited for arbitrary-volume domains, such as the tissues and organs within the head.

- **Selection of the interpolation functions** provides an approximation of the unknown solution within the element. This is usually a first order polynomial(linear), second(quadratic), or higher. Worth mention, that although higher-order one are very accurate, their formulation is more complicated than the lower ones, which is why low-order formulation are still widely used, indeed, a linear one is used in this work. The unknown solution in an individual element, e, can be derived as:

$$\tilde{\phi}^e = \sum_{j=1}^{n} N_j^e \phi_j^e = \{N^e\}^T \{\phi^e\} = \{\phi^e\}^T \{N^e\}, \tag{3.6}$$

where n states for the element nodes, ϕ_j^e is the value of ϕ at e-element, and N_j^e is the interpolation function(also called as the expansion or basis function) for the respective node, j. Moreover, note N_j^e vanishes outside the element, being zero, and is nonzero within the element.

- **Formulation of the system of equations** can be done using either the Ritz variational method [45] or the Galerkin one, which is used here. Then, the residual for the eth element is defined as

$$R_i^e = \int_{\Omega^e} N_i^e (\mathcal{L}\tilde{\phi}^e - f) d\Omega \quad i = 1,2,3,\cdots,n, \tag{3.7}$$

that substituting Eq. 3.6 into Eq. 3.7 yields

$$R_i^e = \int_{\Omega^e} N_i^e \mathcal{L}\{N^e\}^T d\Omega \{\Omega^e\} - \int_{\Omega^e} f N_i^e d\Omega \quad i = 1,2,3,\cdots,n, \tag{3.8}$$

and can be written in matrix form as

$$\{R^e\} = [K^e]\{\Omega^e\} - \{b^e\}. \tag{3.9}$$

The residuals are the gathered as $\{R^e\} = [R_1^e, R_2^e, R_3^e, \cdots, R_n^e]^T$, and $[K^e]$ is $n \times n$ matrix and $\{b^e\}$ an $n \times 1$ column vector, which elements take the following form, respectively.

$$K_{i,j}^e = \int_{\Omega^e} N_i^e \mathcal{L} N_j^e d\Omega \tag{3.10}$$

and

$$b_i^e = \int_{\Omega^e} f N_i^e d\Omega. \tag{3.11}$$

The expansion, and thus the weighing function associated with the node, spans all elements directly connected to the node. Therefore, the weighted residual R_i with the node i is a summation over the elements directly connected to it, and Eq. 3.9 can be expanded using local and global relation, and then summing over each element finding

$$\{R\} = \sum_{M}^{e=1} \{R^e\} = \sum_{M}^{e=1} ([K^e]\{\Omega^e\} - \{b^e\}), \tag{3.12}$$

that seeting to zero, results in

$$\sum_{M}^{e=1} ([K^e]\{\Omega^e\} - \{b^e\}) = \{0\}, \tag{3.13}$$

which in matrix form can be rewritten as

$$[K]\{\phi\} = \{b\}. \tag{3.14}$$

Additionally, and before to solve the problem, the boundary condition of the specific problem have to be applied. Summarizing, this stage requires three sub-steps. First, the elemental equation (Eq. 3.9) is formulated. Second, the whole system is assembled by summing the elemental equations over all elements. Finally, the imposition of the boundary conditions gives the final form of the system of equations.

- **Solution of the system of equations** is the last step of the finite element analysis. In electromagnetics, Eq. 3.14 is usually associated with problems where exists a source or excitation, e.g. scattering problems. After solve the system of equation for $\{\phi\}$, desired parameter, such as the scattering ones, can be computed separately in a postprocessing step.

1-D example

To exemplified and demonstrate the an applied formulation of the method, and for convenience, in this section the FEM procedures is used to solve a one-dimensional boundary-value problem. Though, the procedures can be extended to the 3-D case formulation (see [45]–Ch.5).

Then we can derive the inhomogeneous wave equations from the Maxwell's equation, stating a set of differential equation involving only either electric and magnetic fields. Hence, to obtain the equation for **E**, one can eliminate **H** from 2.9 and 2.10 using the curl-curl formulation, and with the support of Eqs. 2.6–2.8, obtaining

$$\nabla \times (\frac{1}{\mu} \nabla \times \mathbf{E}) - \omega^2 \varepsilon \mathbf{E} = -j\omega \mathbf{J}. \tag{3.15}$$

Considering we are here applying the method to a 1-D problem varying in the x-axis, the governing differential equation that we are solving, vector wave equation 3.15, is reduced to its scalar form as in Eq. 3.16(exact solution), assuming and invariant system along y and z.

$$\partial_x^2 \mathbf{E}_x + \omega^2 \varepsilon \mathbf{E}_x + j\omega \mathbf{J}_x = 0, \tag{3.16}$$

and the bounded domain Ω comprehends from x_0 to x_N. Besides, applying simple Dirichlet (PEC-perfect electric conductor) condition, we have that $\mathbf{E}_x(x_0) = E_x(x_N) = 0$.

Moving to the FEM formulation, Eq. 3.16 is approximated assuming $\tilde{\mathbf{E}}_x \approx \mathbf{E}_x$ as

$$\partial_x^2 \tilde{\mathbf{E}}_x + \omega^2 \varepsilon \tilde{\mathbf{E}}_x + j\omega \mathbf{J}_x = R_x \neq 0, \tag{3.17}$$

where R_x is the residual, and is orthogonal to the function space spanned to $\{w\}$ (testing functions). Then, projecting the residual onto a set of test function $\{w\}$, and forcing it to vanish

$$\int_\Omega \mathbf{R}_x \cdot w_i dx = 0, \tag{3.18}$$

and replacing Eq. 3.17 into Eq. 3.18, it is rewritten as

$$\int_\Omega (\partial_x^2 \tilde{\mathbf{E}}_x + \omega^2 \varepsilon \tilde{\mathbf{E}}_x + j\omega \mathbf{J}_x) \cdot w_i dx = 0, \tag{3.19}$$

which can be split in two parts, aiming to eliminate the higher order derivation and simplify the forcing of the boundary condition, and moving the forcing element $\mathbf{J}_x$ to the right-hand-side(RHS)

$$\int_\Omega (\partial_x^2 \tilde{\mathbf{E}}_x) w_i dx + \omega^2 \int_\Omega \varepsilon \tilde{\mathbf{E}}_x) w_i dx = -j\omega \int_\Omega \mathbf{J}_x w_i dx. \tag{3.20}$$

Then, applying integration by parts ($\int rds = rs - \int sdr$), and defining the RHS as F_i, one obtains

$$-\int_{\Omega}(\partial_x\tilde{\mathbf{E}}_x)(\partial_x w_i)dx+\omega^2\int_{\Omega}\varepsilon\tilde{\mathbf{E}}_x w_i dx+[(\partial_x\tilde{\mathbf{E}}_x)w_i]_{x_0}^{x_N}=F_i \tag{3.21}$$

where the boundary condition are referred to the third element of the left-hand-side. Now, one can also expand $\tilde{\mathbf{E}}_x$ into a set of basis functions u_i, so that

$$\tilde{\mathbf{E}}_x=\sum_{j=0}^{N}e_j u_j, \tag{3.22}$$

where a_j are the expansion coefficients. Thus, it is assumed that the value of $\tilde{\mathbf{E}}_x$ is going to be closer to $\mathbf{E}_x$, when the N, number of basis functions, is larger. Next, substituting Eq. 3.22 into 3.21, the system equations is assembled as

$$\sum_{j=0}^{N}\left(\omega^2\int_{\Omega}\varepsilon w_i u_j dx-\int_{\Omega}(\partial_x w_i)(\partial_x u_i)dx+[(\partial_x u_x)w_i]_{x_0}^{x_N}\right)e_j=F_i, \tag{3.23}$$

that assumes $u_j = w_j$ in the case of use Galerkin's method. The final equation 3.23, can be also referred, because historical antecedents, in terms of four matrix equations named as:

$$\begin{aligned} M_{ij} &= \int_{\Omega}\varepsilon w_i u_i dx && \text{Material Matrix Element}\\ S_{ij} &= \int_{\Omega}(\partial_x w_i)(\partial_x u_i)dx && \text{Stiffness Matrix Element}\\ G_{ij} &= [(\partial_x u_x)w_i]_{x_0}^{x_N} && \text{G Matrix,} \end{aligned}$$

where $\mathbf{M}$ contains the information about the materials, $\mathbf{S}$ relates with the stiffness as cover the derivatives, and $\mathbf{G}$ consider the boundary conditions of the problem. Finally, the whole system can be expressed as a matrix-equation as follow, taking the form of Eq. 3.14,

$$(\omega^2\mathbf{M}-\mathbf{S}+\mathbf{G})\mathbf{e}=\mathbf{F}. \tag{3.24}$$

3.1.2 Applying the FEM-based modeling

As aforementioned at the beginning of this section, the FEM is an optimum alternative to approach problems with complex architectures describing scenarios with arbitrary shapes and complex permittivity distributions, where interact, for example, biological tissues, as the head, with close-by radiating elements. FEM faces the scattering problem by subdividing the whole simulation domain, which contains the imaging domain, into a finite number of subdomains. Allowing, then consider different density-mesh levels depending on the precision and importance of the volume discretized, e.g., on the port of the antennas. Also, it permits the use of homogeneous and non-homogeneous materials, permitting the assignation of diverse characteristics to each mesh element.

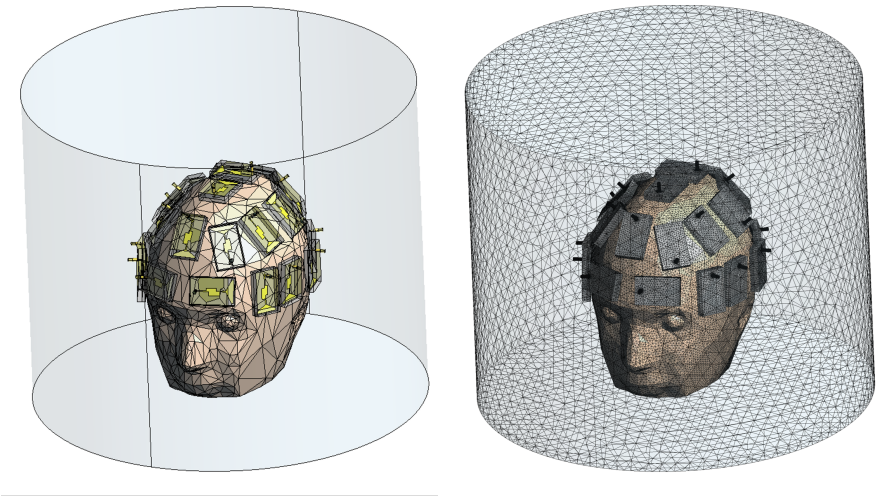

Fig. 3.1 Geometrical realistic representation of the MWI system (a): 3-D models; (b): Superficial mesh view.

In this specific case of this thesis, it employs a 3-D in-house FEM that uses edge-basis functions for the expansions, the curl-curl formulation for the electric field, and the Galerkin approach for testing. Also, regarding the boundary conditions, first, it applies the Dirichlet condition to the metallic surfaces, such as the radiating element of the antenna and the coaxial connectors, thus stating them as perfect electric conductors (PEC) surfaces. Secondly, it forces absorbing boundary conditions (ABC) on the contour surfaces of the cylindrical volume [38], simulation domain, that holds the whole system. Then, to mimic an MWI scenario, we used anthropomorphic stereolithography CAD models for the head, extracted from human models [47], and

the stroke, and faithful reproduction of the imaging system, which are all immersed within a bounded container(see Fig. 3.1).

After the geometrical modeling, it is meshed using a tetrahedral base, and material assigned to each meshed element, i.e., a value of relative permittivity, ε_r, and conductivity, σ. For example, the tetrahedrons in the container are set like air, the organic tissues designed according to [48], and the stoke is filled with a material mimicking dielectric properties of the hemorrhagic or ischemic stroke conditions [49, 50]. Further details on the antenna are described later in this chapter.

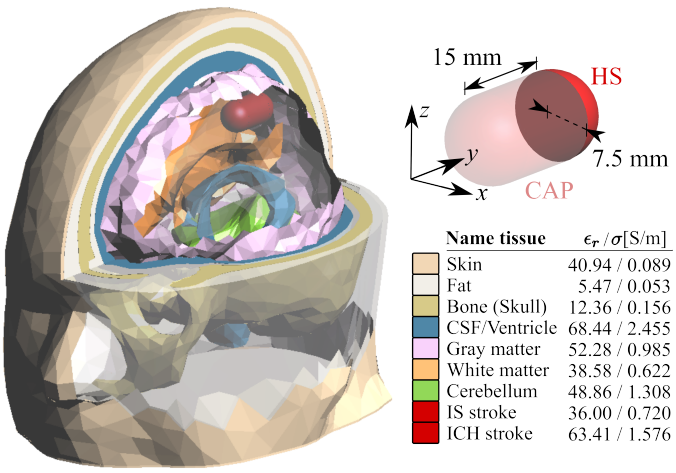

Fig. 3.2 (Left): multi-tissue head model; (top-right): half-sphere (HS) and capsule-shape (CAP) stroke models; (bottom-right): dielectric properties at 1 GHz of all the head tissues and hemorrhagic and ischemic strokes.

At this point, just remain to define the forcing elements of the system, which are then included via the antennas' feeding, essential components to retrieve the fields and compute the scattering parameters accurately. In the specific, the ports are modeled as a section of a rigid coaxial cable, as shown Fig. 3.3(b), and which length depends on the system version. The coaxial interior is filled with lossless Teflon with associated $\varepsilon_r = 2.2$ and finely discretized. The metallic parts are modeled with interior and exterior PEC surfaces and no tetrahedral mesh inside the metal.

The port section, S_p, where the tangential electric field, $\mathbf{E}^{\text{inc}}$, is enforced when the antenna is excited, is at the end of the coaxial cable [green part in Fig. 3.3(b)]. On S_p proper boundary conditions are applied in order to emulate a matched coaxial cable [45], while above S_p a no-meshed PEC "cup" is placed to avoid a nonphysical coupling between the port section and the meshed parts outside the cable.

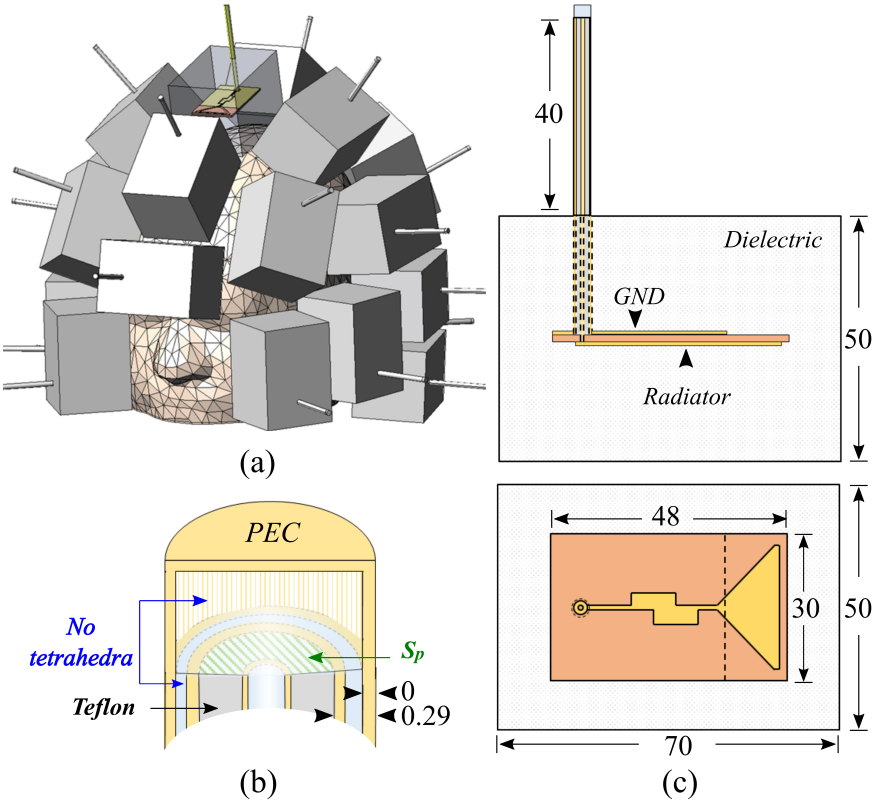

Fig. 3.3 Realistic geometrical models, units in mm; (a): conformal distribution of the antenna array around the head; (b): CAD model of the antenna feeding; (c): monopole antenna embedded into the dielectric brick.

The scattering parameter for each pair of antenna ports, labelled as m and n, is then evaluated as

$$S_{mn} = \begin{cases} \dfrac{\iint_{S_p} \mathbf{E}_m \cdot \mathbf{E}_n^{\text{inc}^*}\, dS}{\iint_{S_p} |\mathbf{E}_n^{\text{inc}}|^2\, dS} & \text{if } m \neq n \\ \dfrac{\iint_{S_p} \mathbf{E}_n \cdot \mathbf{E}_n^{\text{inc}^*}\, dS}{\iint_{S_p} |\mathbf{E}_n^{\text{inc}}|^2\, dS} - 1 & \text{if } m = n \end{cases} \tag{3.25}$$

where $\mathbf{E}_n^{\text{inc}}$ is the electric field forced in the excited port n and $\mathbf{E}_m$ is the electric field evaluated at the port m via the FEM solver. $\mathbf{E}_n^{\text{inc}}$ can be represented with the transverse electro-magnetic (TEM) mode of the coaxial cable as

$$\mathbf{E}_n^{\text{inc}} = \frac{V}{\sqrt{2\pi \ln(b/a)}} \frac{\hat{\rho}}{\rho}, \tag{3.26}$$

where a and b are the internal and external radii of the coaxial cable, and ρ and $\hat{\rho}$ are the radial coordinate and radial unit vector from the center of the coaxial cable in the port plane [45]. The coefficient V is chosen equal to 1 V.

3.1.3 Design of low-complexity MWI device

This section describes the design guidelines, previously presented in [51, 52], for selecting the working frequency and the coupling medium employed later during the antenna design and the implementation of the imaging algorithms. Moreover, it also presents the points assessed for choosing the number of antennas to obtain a good performance, keeping the low-complexity system features, and then the antennas' positioning.

Coupling Medium and Operation Frequency

The frequency and coupling medium play a vital part in imaging-based microwave devices, determining both the maximize the fraction of incident power into the head and the spatial resolution. These parameters are direct degrees of freedom for the device's design since the wave penetration depends on the electrical discontinuity, and the wavelength in the coupling medium dictates the resolution. Then, the rigorous procedure proposed in [51] and numerically validated in [53] is used to select them. It considers a simplified mathematical transmission line model to describe and study the propagation and the interaction between the head, the coupling medium, and the electric incident field, guaranteeing low computational effort.

Thus, exploiting the transmission line formalism, the multi-tissue head scenario is represented as a layered structure modeled as a parallel transmission line network. The model considers, then, the matching medium and the head tissues as line segments, characterized by the estimated length of its actual radial thickness and its corresponding impedance, $Z_n = \sqrt{\mu_0/\varepsilon_0\varepsilon_t}$, where ε_t is the complex permittivity of each tissue while ε_0 and μ_0 are the permittivity and permeability, respectively, of the free space. Specifically for the studied case, the power source is merged in the matching medium in direct contact with the head, which considers the skin, fat, bone, cerebrospinal fluid (CSF), and average brain (grey and white matter). The latter is used as the load.

Then, taking advantage of the equivalent model is computed the transmittance coefficient T, which reveals the amount of power penetrating the head, defining it as [54]:

$$T = 1 - |\Gamma|^2, \tag{3.27}$$

where Γ is the reflection coefficient referenced to the interface plane entering the head. The reported results in [51] show a forbidden band between 1.5-2.5 GHz, where the transmittance is low for any value of relative permittivity from 1 to 80. Also, cases considering frequencies higher than 2.5 GHz may not be convenient due to 2 cm or less penetration depth, d_p for tissues such as skin, bone, or CSF [48], where d_p can be computed in terms of the complex permittivity, $\varepsilon = \varepsilon' - j\varepsilon''$, of the respective tissue as

$$d_p = \frac{c}{2\pi f \sqrt{2\varepsilon' \left[\sqrt{1 + (\frac{\varepsilon''}{\varepsilon'})^2} - 1\right]}} \tag{3.28}$$

where $c \approx 3 \cdot 10^8$[m/s], speed of light, and f stands for the frequency. Moreover, below 0.6 GHz, low-frequency cases reduce the spatial resolution too much, dictated by the background medium wavelength [55]. Finally, the band from 0.6 to 1.5 GHz is identified as an adequate operation frequency range. While values of relative permittivity of the coupling higher than 10 and lower than 40, and low losses, are preferable.

Considering the guidelines below, the 1 GHz frequency point is selected as the target frequency for designing and optimizing the antennas proposed here and presented in the next section of this section. Also, 1 GHz is used later, like operation frequency in the single-frequency-based imaging and the band 0.8-1.0 GHz for the multi-frequency one. Regarding the coupling medium, here is proposed the use of solid and flexible materials, with adjustable permittivity, which is set around 20—further details in the implementation section.

Optimal Antenna Array Layout

This section describes and gathers the method and primary outcomes of [56, 52], exploited here for selecting the system layout. So, the procedure consists of a numerical analysis based on the SVD of a variable imaging operator, where the variable is the number of antennas, N_a, and the head is an average single tissue.

In the following, we assume a frequency of operation of 1 GHz considering the previous section. Then, the study evaluates, first, the robustness of the inversion to higher-level noise and modeling errors via the operator condition number (CN), i.e., the ratio between the largest (first) and smallest(last) singular values. Thus, the lower CN is more robust the inversion is, but when Na increases, whatever the antenna polarization, CN increases too. This fact is explained if we consider that the higher N_a, the closer the antenna element would be. Thus, the information from close array elements would be strongly dependent, in other words, redundant, while the measurement noise is independent.

However, if the number of antennas is around 24, CN remains lower than the dynamics and the SNR of a standard measurement system, about 90 dB. Concluding the preliminary analysis, on the one hand, N_a larger than 48 shows to be unfeasible, being below the 100 dB. On the other hand, when N_a equals 48, the CN is still around 100 dB, which is reasonable, but this implies higher cost and complexity during the implementation.

The other aspect to consider is the effect of the number of antennas on the imaging retrieval accuracy, which decreases due to the loss of information caused by a loose discretization. Therefore, an MWI system has to find a good trade-off between stability and accuracy. Then, a way to quantify the effect of the accuracy is in terms of the discretized error, a metric defined in [56], that considers the normalized difference between a case using a continuous (ideal) scanning surface(infinite number of antennas) and a truncated case(limited number of antennas). Though considering the discretized error as a design parameter must also consider the actual dynamic range of the MWI system aiming at a monitoring application, e.g., an input differential scattering signal for our case is about 70 dB below, and the dynamic range of a medium-performance VNA is 90 dB. Therefore, the actual dynamic range available is around 20 dB, and with this condition, a good compromise is obtained by working with about 24 antennas, again with minor effect due to the polarization.

Finally, to assess the effect on the performance, the point spread function(PSF) was evaluated by projecting an ideal contrast point, mesh element, on the operator, defining the resolution as the points at -3 dB of the normalized image. The results demonstrate a resolution spanning around 1.6 cm to 1.9 cm (around $\lambda/4$), using 79 and 16 antennas—values agreeing with the theoretically estimated one. Moreover, [52] shows that the resolution is stable in the head domain, being just a little low for

the z-axis. Also, the properties obtained with the ideal monopoles remain even in the case of the use of actual antennas.

Summarizing the design procedures, we can state:

- For better matching, penetration of the impinging wave and thus resolution is advisable to immerse the antennas in a coupling medium with relative permittivity around 20 and losses as low as possible.
- In the case of head stroke monitoring, a suitable frequency band is around 1GHz, reaching good levels of transmittance and penetration.
- A 24-antennas MWI device presents a good compromise between performance, cost, and complexity. Also, the polarization of the antennas is a minor design degree of freedom.

However, remains open the issues of the actual implementation and the numerical and experimental validation that validates the design premises. Hence, the following sections and chapters face them.

3.2 System Implementation

This section focuses on implementing a functional MWI prototype using as a starting point the consideration expressed in the design section and preliminary numerical validation presented in the next chapter. It is divided into three main subsections. The first describes the general system getting into detail on the hardware components, from the electronics collecting the signals produced by the antenna array to the processing unit, but letting the antenna aspects for the following subsection. Then, the last part covers the experimental setup, including the manufacturing of phantoms, mimicking liquids, and experimental procedures used during the validation.

3.2.1 MWI Prototype

As was viewed in the design section, to reach a good performance with low complexity requires a system working with around 24 antennas, implying the need for instrumentation able to generate radiating stimulus and gather the back-scattered

signal in a multi-view. This device is generally a vector network analyzer, which characterizes the system as a network via the S-parameters. However, the VNA are expensive devices that increase their price depending on the number of ports, and even if a 24-port VNA is available in the market, its use highly boosts the cost of the prototype. Then, the proposed prototype opts for a system architecture using a typical 2-port VNA and a 24×2 switching matrix multiplexing the signal, allowing the acquisition of the complete scattering matrix for the imaging. The switching matrix thus connects a pair of antennas at once and, through a loop, fills the 24×24 matrix. This dynamic measuring approach adapts to the prototyping and the lab validation, where the system's variational conditions are controlled during the experimental procedures. So, there are no expected significant changes in the studied scenarios during the measuring time, except for the effects of noise that would also be present in the case of an instantaneous measurement. However, it is also applicable in more realistic clinical scenarios since the stroke variation is slow compared to the measuring times.

On the one hand, the switching matrix is a good alternative for prototyping and even a pre-clinical device. Though on the other hand, it also has associated drawbacks. It would limit the system's speed depending on the type of switches and the isolation between ports. It includes additional hardware, increasing the overall complexity of the system and the risk of failures, which are not always easily detectable. Moreover, it is difficult to accurately model it so that its effects can be added to the imaging kernel later. Thus, it is generally needed to include additional calibration that brings the measures S-parameter to the reference used during the building of the imaging operator. After weighing the pros, cons, and

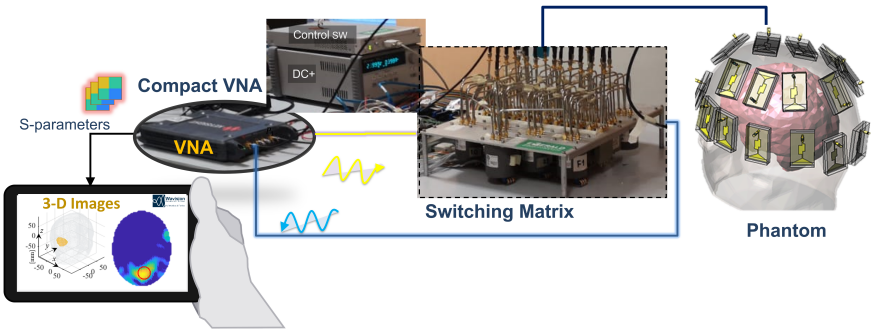

Fig. 3.4 Schematic view of the implemented MWI prototype.

available resources, this work uses an architecture consisting of a compact 2-port

VNA and a 24-to-2 switching matrix, as illustrated in Fig. 3.4. The whole system elements, from left to right in the figure, are listed below:

- **Laptop or portable device** where are loaded the imaging software and switching control scripts, and visualized the retrieval images. Finally, a laptop allows controlling the switches, collecting, and processing of the data.
- **Vector Network analyzer(VNA)** that provides the stimulus to the radiating unit, antenna coupling-medium pair, and receives the response.
- **Source power** feeding the Switching matrix (DC+ in the figure).
- **Control SW**, is a card acting as the interface between the Switching matrix and the switching control scripts.
- **Switching Matrix** is a controlled 2×24 multiplexer.
- **Antenna array(Helmet)** contains the Tx/RX antennas that radiate and sample the field.
- **Phantom** mimics an actual head shape and dielectric properties.

The next subsections extend the description of the main hardware parts: VNA, switching matrix and antenna, and the mimicked clinical scenarios.

Vector Network Analyzer

The VNA is one of the most advanced microwave devices our days, consisting of broadband sources and high-speed and high-dynamic-range receivers. It measures the S-parameters or the constituent wave quantities (e.g. a_1, b_1) of passive and active devices under test, which in the MWI problem are sensitive variables sampling the field variation response within the head. So, in general, it gathers incident and reflected waves at each port of interest while delivering input signals at the different ports. Therefore, a VNA, as shown in Fig. 3.5, consists of a signal source(shared or individual for each port), some receivers, and a mechanism to separate the incident and reflected ones, which is typically a microwave directional coupler.

VNA measurements can be done using one or many ports, over swept frequency, or swept power, depending on the measurement requirement. In this case, the VNA

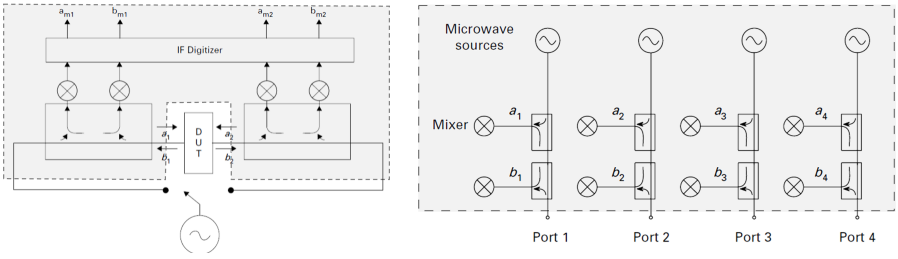

Fig. 3.5 Vector Network Analyzer scheme. (left):2-port network; (right):4-port network.

was set up for either mono-frequency(1GHz) or multi-frequency(0.8-1GHz), and the power was between -5 dBm and 0 dBm.

Considering the performance degrades as frequency increases, the features of the device must guarantee linear operation in the working band. This requirement does not represent a big issue for the studied application since the band around 1GHz is even covered by mid-range devices.

Moving to the implementation, the two VNA ports are connected to the switching matrix via flexible coaxial cables. The function then is to generate and collect signals for the multiple antennas around the head, as a multi-view system requires, by sets of 2 by 2 S-matrix. Information that is provided as input data for the implemented imaging algorithm. Because here are presented two systems, it is worth mentioning that two different models of VNA were tested during different moments of the experimentation. Initially, it was used the standard VNA (Keysight N5227A, 10 MHz – 67 GHz), where the input power is set to 0 dBm and the intermediate frequency (IF) filter to 10 Hz, and second, the compact Streamline USB Vector Network (P9375A Keysight, 10 MHz–26 GHz)[57], setting the power to -5 dBm and the IF filter to 100 Hz. Note that decreasing IF BW will reduce the noise floor by filtering the portion that is outside the bandwidth of the digital filter.

The chosen VNA setups allow reaching the VNA noise floor at about -110 dB (at 1GHz), optimizing the measuring time and thus most affected for the switching times. Also, and most importantly, these levels are below the differential scattering matrix measures that are above -100 dB, guaranteeing the information content.

Moreover, the VNA is used with the 85070D Keysight dielectric probe to measure the phantom materials' dielectric.

To conclude, the VNA is an essential device for the prototyping of MWI devices that bring a lot of flexibility to the design process, being essential for the proof-of-

concept of the technology. However, moving to clinical prototypes, the VNA may be an oversized device, requiring the development of ad-hoc hardware.

Switching Matrix

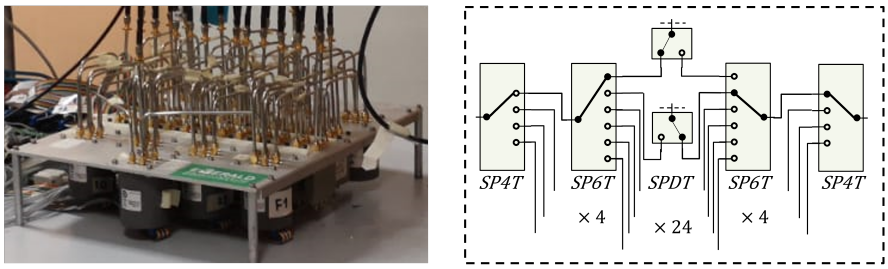

Fig. 3.6 The 2×24 Switching matrix. (left):Picture of the implemented system; (right): scheme of the matrix.

The switching matrix allows the MWI system to acquire the multistatic multiview scattering matrix used for the imaging, i.e., the switching permits each antenna to transmit or receive, sequentially completing the full matrix by segments. A variety of high-quality electromechanical coaxial switches with low insertion(<0.3 dB) loss and high isolation(>90 dB) compound the switching matrix in a way that does not negatively limit the overall dynamic range of the prototype.

The switching matrix involves a two-arms architecture using three types of switches [41], single-pole-four-throw (SP4T), single-single-pole-six-throw (SP6T), and pole-double-throw (SPDT), as shown in Fig 3.6. Then, each antenna connects to the pole of the single-pole-double-throw (SPDT) switch via a flexible coaxial cable. Instead, each VNA port connects via a flexible coaxial cable to the pivot of the single-pole-four-throw (SP4T). Moreover, semirigid coaxial cables connect the switches using pieces of similar length, so both left and right connections for any antenna pair have the same distance.

Finally, a Matlab script automatizes the measuring flow control and communication(via Ethernet) with the switches through a control card that uses the VISA/TCPIP (VXI-11) protocol. Then, the measuring code is integrated within the same application with the imaging algorithm, allowing efficient reconstruction in almost real-time, running from a standard laptop.

The time for complete measurement set acquisition is around 6 min, and depends on the setup of the VNA and the speed switching matrix. Though it is worth noticing that the measuring time is mainly affected by the mechanical switching time in the multiplexing matrix, thus, replacing the actual one with solid-state switches would improve the time performance of the prototype [58].

Brick-shaped Antennas and layouts

The antenna array is critical in MWI systems because it must supply accurate data to the algorithm that generates the image of the examined scenario, entailing a good radiating element design in selecting a suitable operating frequency band and coupling medium. The frequency determines a better spatial resolution for higher frequencies compared to lower ones reaching deeper wave penetration, affecting the receiver's dynamic range and sensitivity. In addition to the frequency degree-of-freedom, a coupling medium placed between the antenna array and the head also improves the penetration.

This section presents the design of two antennas keeping the mentioned trade-off in mind. Then the antenna design targets an antenna working in the band around 1 GHz, while possibly being immersed in a coupling medium with high relative permittivity. Regarding the latter, the coupling medium is not required when utilizing (rigid or flexible) on-body antennas, which might increase penetration by being connected in practically direct contact with the skin. This approach has been tested for biomedical imaging by different authors. For instance, [59] proposes planar bowties, [60] a F-like cavity-backed antennas, and [61, 17, 18] flexible antennas and arrays. However, if the antenna is mounted to the head, tissues in the very near field of the antenna would unpredictably change the antenna reflection coefficient (due to human variability), potentially causing problems for the imaging algorithm. Furthermore, near-field effects are difficult to predict and only contribute slightly to reconstructing the interior imaged region.

On the other hand, the coupling medium is generally a liquid-based(or gel) one, e.g., water mixtures with glycerine or Triton X-100. This approach, while simple, has problems in terms of mobility, operability, and complexity of experimental(clinical) procedures since the antenna array must be immersed in the liquid media. Thus, the execution of the imaging on mobile media, such as an ambulance, would be more tedious. Also, even in monitoring bedside scenarios, the need for coupling liquids

would increase the protocols' complexity, difficulting the clinical trials and possibly diminishing the medical community's interest. Furthermore, it may restrict the array elements' conformal displacement around the head.

Table 3.1 Materials Composition and Permittivity - G# Mixture

	Graphite [%]	Rubber [%]	ε_r (1 GHz)	σ [S/m]
Matching	25	75	13	0.18
Substrate	35	65	18	0.3

Here it is proposed to overcome the issues mentioned above exploiting a semi-flexible custom-made material as a coupling medium and even substrate in the second version of the antenna. It is made of a mixture of urethane rubber and graphite powder. The former is used as cohesive, while the latter is a permittivity booster. Table 3.1 presents two example of percentage mix variations of graphite and rubber with their respective values of complex permittivity at 1 GHz, which are used later in the manufacturing of the antennas. In the table and the following, we refer to the material as G#, where the G stands for graphite and the number,#, for the percentage of it in the mixture. Thus, G25 indicates a material where 25% is graphite and 75% rubber in weight, respectively. Notice also from the table that the increase of graphite percentage besides of increase in the relative permittivity also raises the losses, being this one of the reasons for not raising more it. The second reason relies on the mechanical and chemical properties of the materials. For cases upper to the G35, achieving a homogeneous and consistent mixture is really difficult. Also, the flexibility of the material is inverse to the increase of graphite.

The next sections present two different evolving antenna designs, which take as starting point of optimization a monopole antenna designed to work in a liquid media. Figure 3.7 illustrates, from left-to-right, first, the antenna base used as a reference and previously tested in [41], second, the v.1.0 of the brick-shaped antenna proposed here, and last, the v.2.0 a more flexible, lighter, and less bulky version. As can be seen from the figure, in both cases graphite-based materials are used.

Brick-shaped Antenna 1.0

In the first version of the antenna, v.1.0 (reported in [62]), the main idea relays on building a non-liquid and discrete domain when a monopole can be embedded,

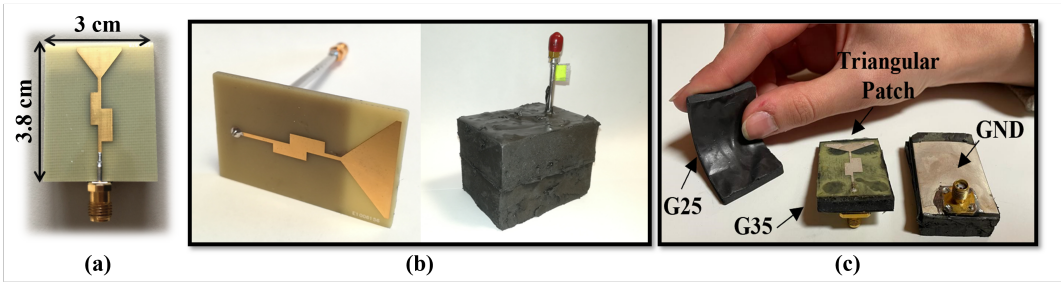

Fig. 3.7 Antenna evolution (a):Antenna base; (b):brick-shaped antenna(v.1.0); (c):flexible brick-shaped antenna(v.2.0).

retaining the advantages of the full extended liquid-based ones. Thus, avoiding near-field effects and making more stable the antenna reflection coefficient. Additionally, this approach aims to gain operability freedom and maneuverability for antenna conformal positioning around the head.

Considering the points discussed in the Sect. 3.1.3 and proposed in [53] and [63, Ch. 2], the antenna is projected to work in the frequency band around 1 GHz, while the coupling medium permittivity is $\varepsilon_r \cong 20$, presenting a good compromise between the spatial imaging resolution and the electromagnetic (EM) penetration inside the head tissues. Then, as aforementioned, the antenna optimization starts with the monopole antenna reported in [41], which is designed to work in a liquid coupling medium. So, for the first prototype, the objective was to optimize the antenna in a way that it could operate in a discrete coupling medium, which should be realizable with a G# mixture. The optimized antenna consists of a triangular-shaped radiating element, a trimmed back-placed ground plane, and a line, with two stubs designed to improve the antenna matching at the port, fed by a rigid coaxial cable on the back, adding stability and reducing the unwanted variation in the vicinity of the port. The final geometrical is shown in Figure 3.7 and its dimensions are listed in Table 3.2. This design then presents and front area (radiating) part of the proposed brick antenna equal to 5×7 cm^2, considering the average area of the upper part of a human head is about 1000 cm^2, makes possible to place up to 28 brick antennas around it, which is slightly larger than the number of antennas identified by the design procedure in [52, 56]. Though, during the actual placing, there was used a 3-D printed helmet acting as support of the 24-antenna array as shown in Fig. 3.9, which does not let considerable spaces between antennas.

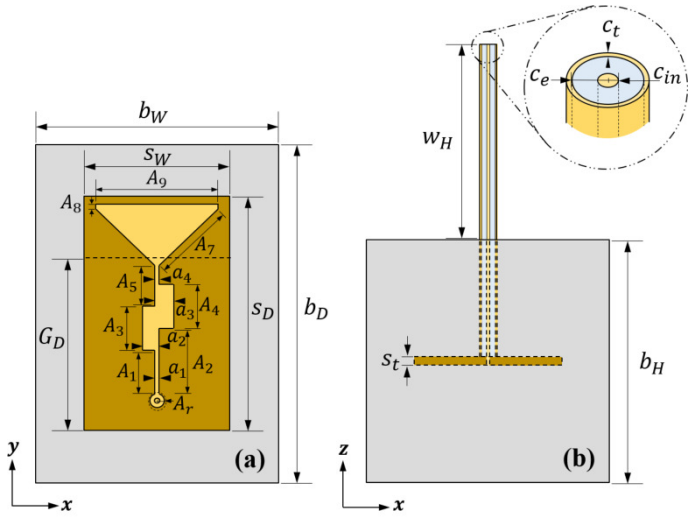

Fig. 3.8 Antenna geometry; (a): top-view on the antenna plane; (b): side-view on the antenna port. (Original figure reported in [62])

The coupling medium keeps a distance of 25 mm between the monopole plane and the brick-head surface in a perfect attaching condition, corresponding to about 0.4 times the wavelength in the coupling medium at 1 GHz. It diminishing near-field effects, which are hard to adequately model and scarcely contribute to the image reconstruction [64]. The brick-radiator pair within an MWI system produces a single unit that can be easily integrated into an array arrangement conforming to the head. Furthermore, the semi-flexible solid medium provides extra mechanical rigidity and stretchiness to the antenna, increasing its durability and allowing low-degree bends, which are necessary to cover the head. Furthermore, the brick is portable and enables various antenna distribution schemes while lowering manufacturing and maintenance costs.

Table 3.2 Dimensions (mm) of the brick antenna (see Fig. 3.8)

Label	Value	Label	Value	Label	Value	Label	Value
A_1	9.09	A_7	1.00	a_4	1.00	b_W	50.00
A_2	13.59	A_8	25.28	G_D	35.40	b_H	50.00
A_3	9.00	A_r	1.50	s_W	30.00	w_H	40.00
A_4	9.00	a_1	1.00	s_D	48.00	c_t	0.29
A_5	8.50	a_2	2.44	s_t	1.55	c_e	1.51
A_6	16.72	a_3	2.90	b_D	70.00	c_{in}	0.47

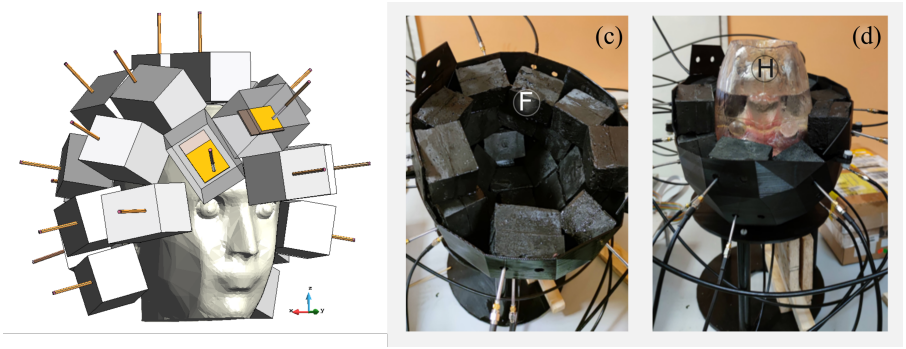

Fig. 3.9 24-element Helmet using the brick-shaped antenna v.1.0, [65, 40]

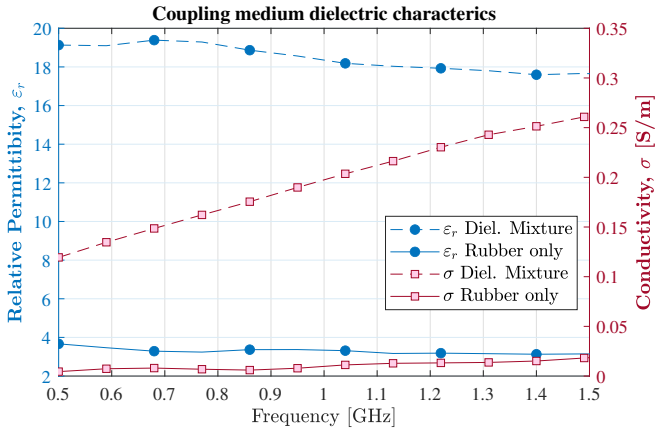

Fig. 3.10 Coupling medium dielectric characteristics versus frequency, [62] ©2020 IEEE

We used an omnidirectional antenna in our design to illuminate the whole area of interest (possibly allowing a reduction of the number of array elements). Furthermore, the effect of an omnidirectional antenna operating in the proximity of an unknown and variable medium (the head) on the near-field antenna pattern is likely to be less prominent.

The brick is made of a semi-flexible G35 mixture, whose dielectric characteristics are shown in Fig. 3.10 (dashed lines). As expected, the graphite powder increases the conductivity (see Fig. 3.10, lines with squared markers), but it remains in the range of other media used in medical MWI [41, 14, 66].

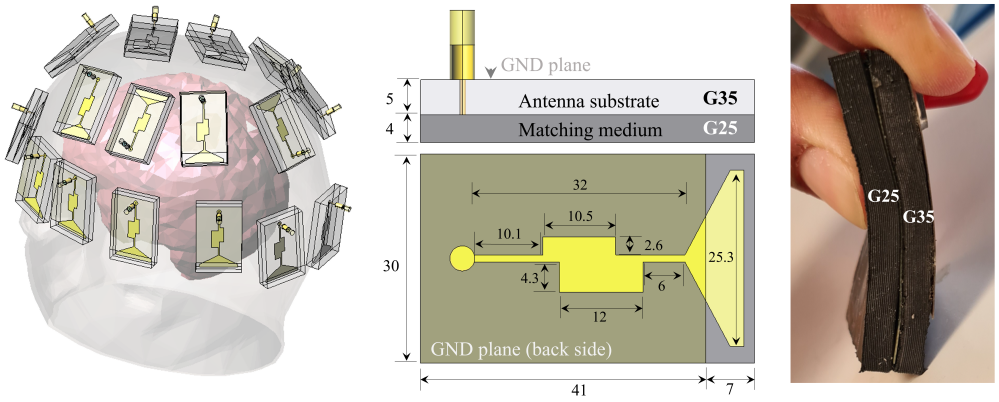

Fig. 3.11 Brick-shaped antenna v.2.0, (left):distribution scheme; (middle): antenna diagram with all dimensions in mm; (right): lateral view with bending.

Brick-shaped Antenna 2.0

For this second prototype, the aim was to reduce the size and weight, the main drawback of the v.1.0, of the device using a more compact and lighter brick-shaped antenna. So, in this case, the starting point of the optimization was the brick-shaped antenna 1.0, which was then optimized to work in closer proximity to a human head. Also, to give the process additional degrees-of-freedoms, the substrate material and thickness were included as optimization parameters, assuming it can be custom-made using the same procedure with the coupling medium.

The optimized antenna is made up of two stacked layers of unique flexible dielectric material with a low-complexity monopole circuit-printed in between and back-fed through a coaxial cable, as shown in Fig. 3.11. The first layer acts as the typical substrate for printed antennas, although it is constructed of a material that may be customized in this case. The antenna ground (GND) plane is printed on flexible commercial 50m thickness polyimid film on the backside, and a printed triangle radiator is put on the front side. The second layer is likewise a dielectrically adjustable medium that minimizes the antenna-to-head mismatch. The customized layers, which are made of urethane rubber and graphite powder combination, are tweaked to reach a reasonable trade-off between high permittivity and low losses. Table 3.1 reports the weight percentage to get both layers, substrate G35, and coupling G25, and their dielectric properties, respectively.

The whole antenna module – substrate, the matching medium, and the printed monopole– reaches enough flexibility to adapt to the head curvature as cab be seen

from Fig. 3.11(right). The optimized antenna works in a -10 dB band from 0.85 to 1.25 GHz, reaching adequate penetration and resolution for the application, as shown later in the validation chapter. As a result, the suggested module combines the advantages of a flexible antenna with the cheap cost, low complexity, and adaptability of a traditional antenna. To put it another way, a modular design makes it easier to grow or upgrade a system while also making it easier to maintain and repair.

Finally, the antenna layout takes a 22-antenna configuration covering the conformally to the upper part of the head, which is still in agreement with the design constraint [52], while reducing the complexity of the system. The performance of the antenna is discussed in the next chapter.

3.2.2 Mimicking the Clinical Scenarios

In order to validate the designed prototypes in meaningful scenarios, this section presents the development of, first, realistic anthropomorphic phantoms, and second, the experimental procedures resembling a monitoring evaluation. The former includes both the phantom printing and the manufacturing and characterization of the liquids mimicking the dielectric properties of the head and strokes. The latter covers the virtual and the in-situ experiments.

Realistic Phantoms

Before moving to clinical, pre-clinical, or even test with animals, it is totally required to extend the validation of the MWI prototypes further than the numerical validation. Thus, it is essential to devise strategies that resemble the clinical scenarios to be sure the system would work in clinical conditions. To achieve then this objective, we used a two-fold strategy. First, to represent the head electromagnetically, we utilize mixtures of liquids that approximate the characteristics of the head in the band of operation of our device. Second, to consider the shape complexity of the head and strokes, we explore the use of realistic 3-D printed phantoms. Overall, using these two approaches gives us certainty in the proof-of-concept applied in realistic monitoring scenarios.

- **Mimicking the properties of Head and Stroke**

Table 3.3 Mimicking Materials Composition and Permittivity[1]

v.1	Triton X-100[%]	Water [%]	Salt [g/l]	ε_r (1 GHz)	σ [S/m]
HEM	50	50	5.2	68	1.5
ICH	14	86	9.4	34	0.6
Brain	38	62	5.2	45	0.7
v.2	·	Alcohol	·	·	·
HEM	33	66.4	5.2	63	1.5
ISC	70.1	29.4	4.3	36	0.7
Brain	59.7	39.9	3.5	45	0.8

To produce the liquids filling the head we use mixtures based on Triton-X and alcohol, mixed in different proportions with demineralized water and table salt(NaCl), following the receipts reported in [67, 68] and [69], respectively. For the alcohol-based one, the recipe is refined to obtain a customized formula with commercial ethylic alcohol. All the recipes obtained for the employed liquid mixtures are reported in Table 3.3, together with the corresponding target dielectric parameters (i.e. relative permittivity, ε_r, and conductivity, σ [S/m]). In Table 3.1, HEM and ISC stand for the hemorrhagic and ischemic stroke cases, which real reference values are taken from [50, 70], and Brain refers to the average dielectric properties of the brain tissues considering a compound of 75% of white matter and 25% of grey matter [67].

The open probe technique was used to evaluate the dielectric characteristics of tissues and liquids. The measuring system comprises the two-port P9375 VNA [57], a low-phase coaxial cable, and the 85070D dielectric probe. The VNA measures the reflection coefficient of a probe that is submerged (as in liquids) and in direct contact (as in the calf brain) with the material under test (MUT) and is dependent on the MUT's unknown dielectric characteristics. A modal expansion at the probe tip, quasi-static techniques, or lumped circuit models can be used to extract the unknown MUT dielectric characteristics from the observed reflection coefficient. In this study, we employed the lumped element model[71], which has been shown to be accurate[72]. A routine calibration process was carried out before the MUT measurement. For that purpose, the probe reflection coefficient was evaluated in three different environments: air(open), closed on a perfect electric conductor (short), and distilled water (well-known load) [73]. Before the MUT measurement, a standard

[1]Table adapted from [40]

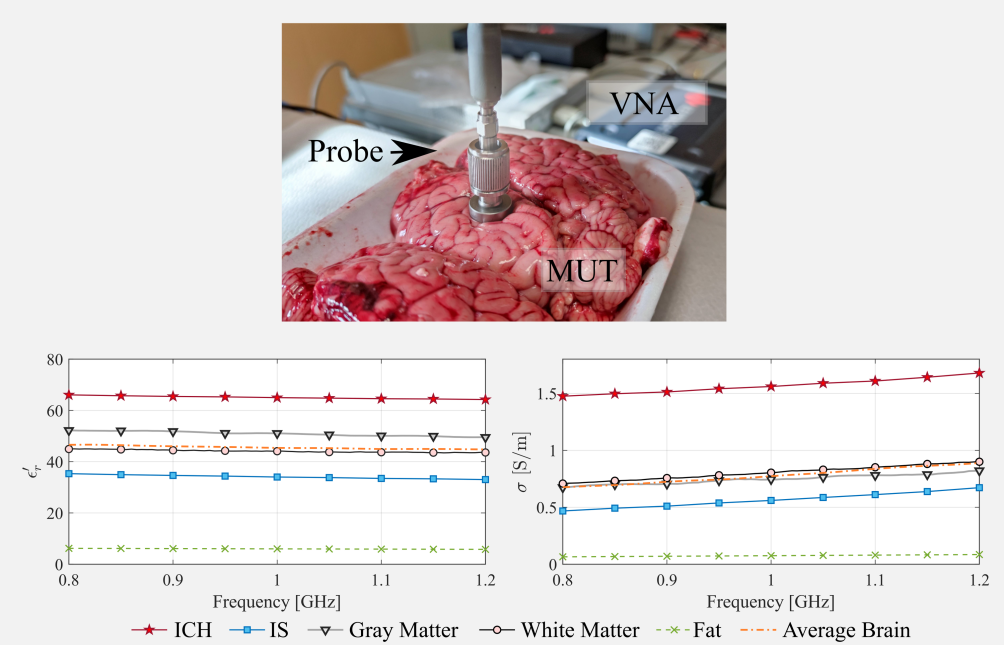

Fig. 3.12 Measured dielectric properties of the multi-tissue head phantom; (top): experimental set-up; (left): relative permittivity; (right): conductivity, [40].

calibration procedure was performed. To this end, the probe reflection coefficient was measured in three known cases: air (open condition), closed on a perfect electric conductor (short) and inserted into distilled water (well-known load) [73].

Figure 3.12 depicts the observed dielectric characteristics as well as the experimental brain characterization setup. White and gray matter are considered independently throughout the characterization phase of a calf-made brain. Details on the calf-made brain in the next section.

For the alcohol-based liquids, the dielectric characterization was performed through an open-ended coaxial probe and the Keysight N1500A materials measurement software suite [74]. The resulted properties in the band 0.5-2 GHz are reported in Fig. 3.13, where the blue band indicates the frequencies used later during the multi-frequency validation.

Each liquid base has its pros and cons to be considered during the validation. First, both show dielectric characteristics stability during a session of measurements (appr. 1 day). The Titron-based one is much more stable, keeping its properties even for weeks after being prepared. The drawback is the fluctuation of its viscosity and consistency depending on the room temperature, e.g., for mixtures like the average

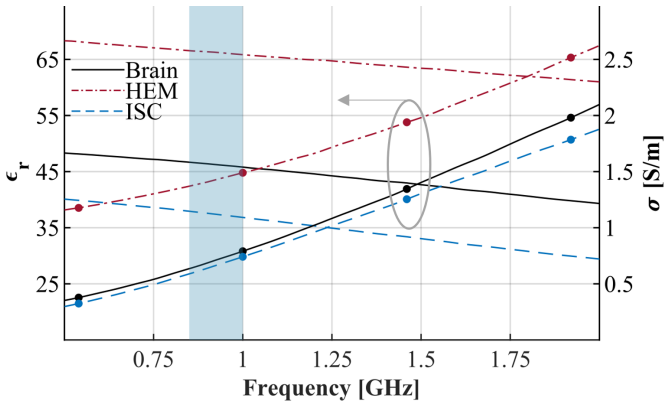

Fig. 3.13 Dielectric properties characterization of the alcohol-based mixtures, [75] ©2022 IEEE.

brain, it solidifies in temperatures lower than 23 degrees. Thus, using this mixture requires a major control of the room and/or being warmed constantly, affecting the water content and degrading the recipe faster. Therefore, if the testing does not require changing the scenario, for example, in a characterization of the noise that requires many measures of the same scene, the solidification is not an issue. Instead, suppose the scenario needs to be changed like in a monitoring test. In that case, the solidification will cause bubbles to get trapped in the mixture, causing much more variation than the one due to the stroke variation.

On the other hand, the alcohol-based ones remain liquid at room temperature or others. Besides, thanks to its liquid nature, the disturbances created during the stroke variation are minimal. Though the alcohol is highly volatile, what causes it quickly evaporates, changing the properties of the mixture and thus requiring more periodic adjusting. In conclusion, the best option would depend on the application.

- **Head phantom: Homogeneous and Multi-tissue**

Starting with the ***"homogeneous phantom" (HP)*** version of the phantom, it consists of a single cavity anthropomorphic 3-D printed adult head derived from a stereo-lithography (STL) file based on MRI scans. The STL file was obtained with computer-aided design (CAD) software by modifying an original file from the Athinoula A. Martinos Center for Biomedical Imaging at Massachusetts General Hospital. The printed head is made of clear resin (polyester casting resin) with dielectric properties similar to plastic $\varepsilon_r \approx 3$ and thickness around 3 mm. So that, electromagnetically it may compares with air gap with the same thickness. This

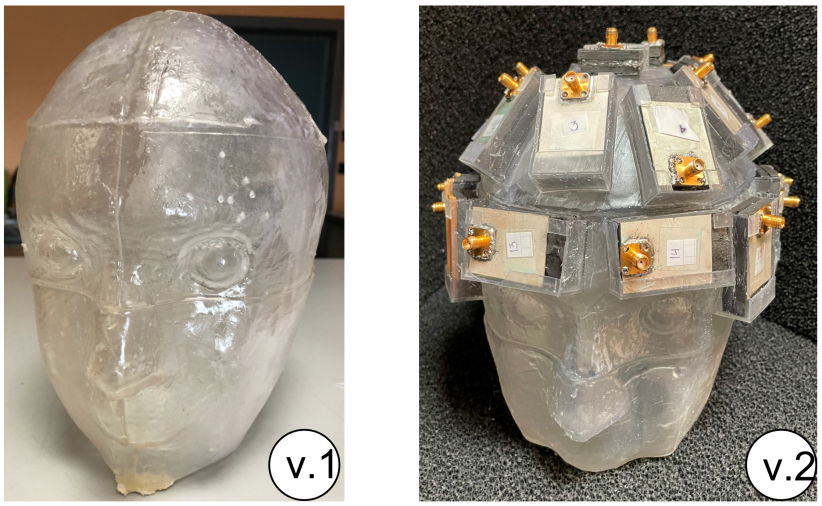

Fig. 3.14 Head phantoms used for test each of the system versions, [65, 40]

effected was studied in [39] and presented in the validation chapter, finding adequate penetration in the range of interest for both homogeneous and multi-tissue heads.

Figure 3.14 depicts two versions of the head phantom used, respectively, for each of the versions of the system. For the first version, the head is upside down and then positioned in the head. Thus, in this case, the phantom is filled up from the neck. The second version, instead, does not need to be turned and is filled up from the top part. This version also includes supports, so that, the antennas can be behold there. This fixed positioning help to reduce the model error due to non-modeled alignments, as well as, to keep the antennas in contact with the head all the time. However, for future versions, the antennas will be held for external support, like the helmet in version 1.0.

The second version of head phantom used, referred to as ***"multi-tissue phantom" (MTP)***, takes as the container the HP.1.0 and introduces an assembled brain made of ex-vivo calf brains, bringing them closer it to actual clinical conditions (e.g., tissue inhomogeneity and complexity), as Fig. 3.15. Figure 3.15(b) shows how each hemisphere of the human adult brain was recreated using two calf brains and molded using a plastic 3-D printed shell. The brain shell was only utilized to form them into human-like shapes and was not utilized in the measuring process. Each hemisphere

[2]The used calf brains were already available in the regular food distribution market, and the authors had no relation to or influence on the butchering.

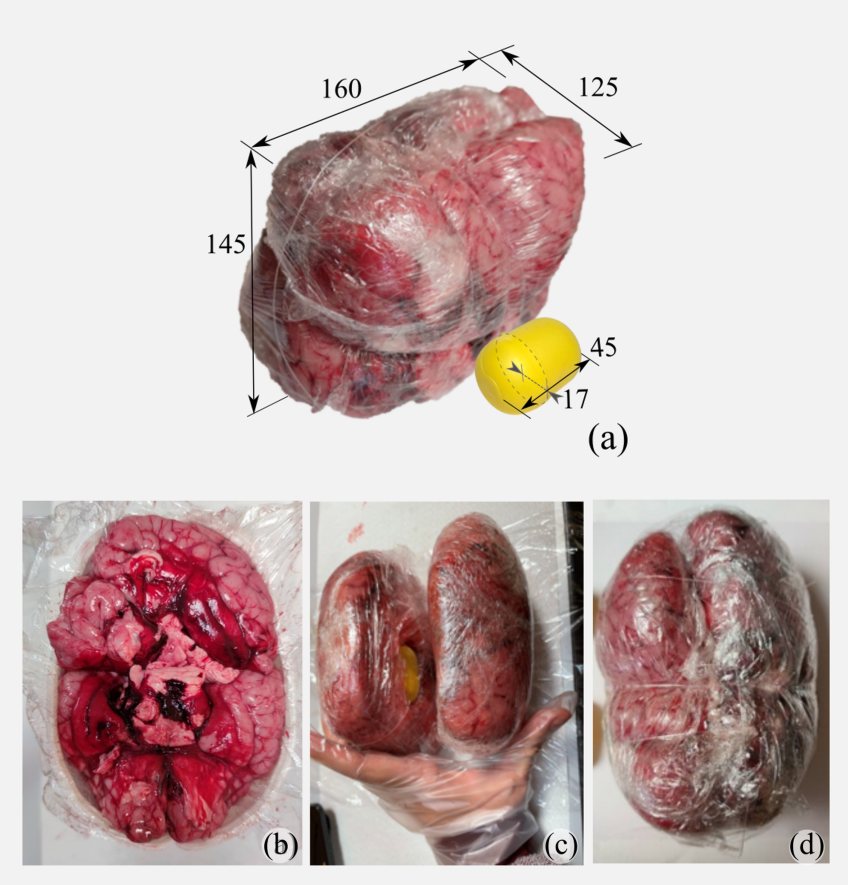

Fig. 3.15 Multi-tissue phantom (MTP); (a): brain and stroke phantom (dimensions in mm); (b): one hemisphere preparation; (c): two hemispheres with inserted stroke; (d): joined brain; (e): head phantom with immersed brain and filled up with electrically fat-mimicking liquid.(original figure in [40]) [2]

of the human adult brain was reproduced with two calf brains and shaped using a plastic 3-D printed shell, as shown in Figure 3.15b. The brain shell was used just to mold them as a human one and is not included in the measurement setup. After that, a plastic film was stretched to the hemisphere and a monofilament polymer line was used to connect it(see Fig. 3.15(c-d)). The acquired brain weighed around 1.5 kg, and had a capacity of about 1200 cm^3. Finally, the entire brain was fitted into the head plastic phantom, which was already filled with the fat-like liquid.

- **Stroke phantom: Static and non-static ones**

A spherical plastic ball was used to create the initial stroke phantom. In the case of cerebral bleeding and ischemia, however, plastic has a larger dielectric contrast within the brain, affecting both the measured signal level and the imaging method [65]. Hence, the stroke is implemented here filling up the already mentioned liquid mixtures mimicking both hemorrhagic and ischemic conditions into a small plastic container as the yellow capsule with a volume of around 50 cm^3 in Fig. 3.15(a). Using this type of stroke, the first version of the system is tested, evaluating its capabilities to detect and localize it.

To emulate a stroke-affected area it is employed a capsule-shaped balloon, which can mainly expand in the longitudinal direction, allowing a more accurate assessment of the differences between the following scenarios. Then it is realized simple support, invisible to EM waves, to fix the capsule in the decided position and avoid undesired movements during the experiments. Determining the typical dimension of strokes (or their volume growth) is a difficult task. A stroke can range in size from 2 to 200 cm^3 in volume, depending on a variety of factors such as the location, the blood vessels involved, and the timing of diagnosis. (see, e.g., [76–79]). The stroke grows fast in the first few hours after it occurs, and clinical investigations suggest that a stroke can continue to progress after 72 hours (rarely more), worsening the patient's health. However, because early stroke follow-up is largely focused on clinical examinations rather than image-based diagnostics, there is no clear benchmark for stroke spread in the first hours after it occurs.

In line with the variability of the stroke, and aiming to develop phantoms that mimic the spatial evolution of the pathology in a relative straight way, the second version of the stroke are non-static ones, i.e. these can evolve during the monitoring, thus, allowing us to assess the capabilities of the system for tracking the change.

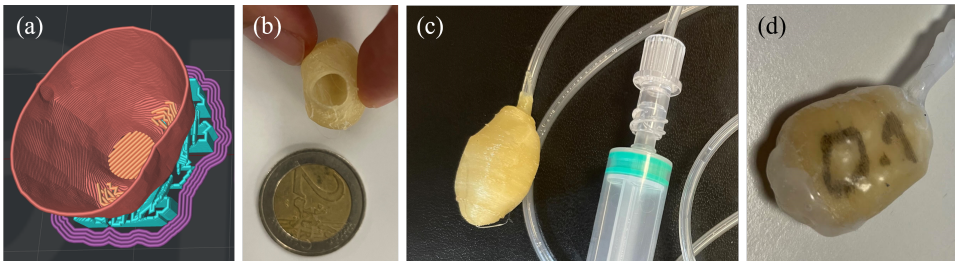

Fig. 3.16 Stroke phantom manufacturing. (a) 3-D model cut view; (b) PVA mold; (c) Model sealed; (d) Stroke phantom before of remove PVA material, [82] ©2022 IEEE.

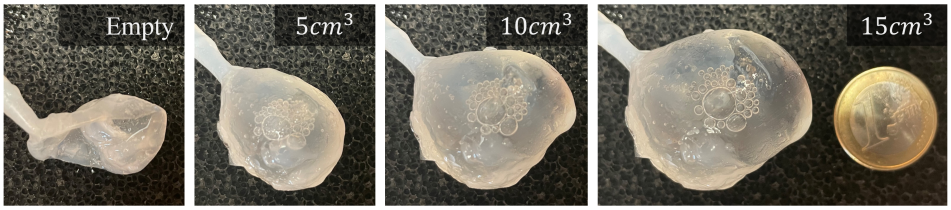

Fig. 3.17 Photo of the non-static stroke phantom growth. From left to right: Empty, 5 cm^3, 10 cm^3, and 15 cm^3, [82] ©2022 IEEE.

Then in the first approach, the non-static phantom was projected as a simplified homogeneous stroke model of an actual one, obtained by segmenting CT medical[3]. Then, the model is 3-D printed with a PVA 3D filament [80], which has the feature that can be dissolved with water, with the printer's minimum thickness extrusion setting (around 0.1 mm) and the number of layers by thickness set to one (see Fig. 3.16a). After that, the printed mold, Fig. 3.16b, is coated using a thin layer(less than 1 mm) of slow-cure platinum silicone layer [81], letting it rest until is totally cured some hours later as shown in Fig. 3.16d. The last step is to remove the PVA by injecting water, and then, removing the residuals via a small hole, which is used later to attach it to a 3mm-radius feeding cannula. The result is realistic stroke, multi-use, and resistance. Figure 3.17 illustrates four different states of the stoke, that are used later to validate the monitoring.

Moreover, to emulate a bigger stroke-affected area it is employed an adapted capsule-shaped balloon, which can mainly expand in the longitudinal direction, allowing a more accurate assessment of the differences between studied scenarios. Figure 3.18 shows, also, four different states the bigger stoke.

[3]Work in collaboration with the Emergency Medicine Dept. of Lariboisière University Hospital, Paris (FR).

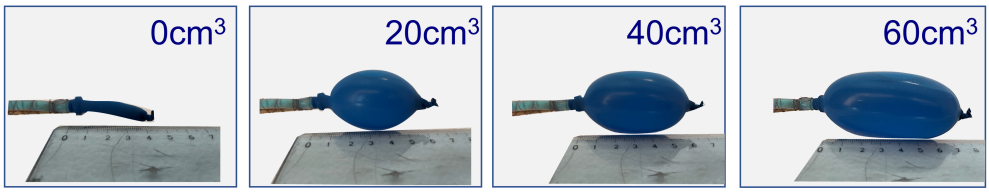

Fig. 3.18 Photo of the non-static stroke phantom growth. From left to right: Empty, 20 cm^3, 40 cm^3, and 60 cm^3

3.3 Experimental Procedures

This section describes the procedure followed during the validation of the device. The first part focuses on the numerical elements that are later fundamental during the experimentation. So this initial part tests the virtually the capabilities that later are emulated experimentally. The second part considers the experimental aspects proposing different assessment tests for the device.

3.3.1 Virtual Experiment

The virtual experiment supports the distinct stages of development of the MWI device, being an essential part of the design of the antenna, the preliminary test of the functioning of the imaging algorithm, and the evaluation of the capabilities and limitations of the system.

Then, as aforementioned in previous sections, the central part of the numerical validation is performed using an in-house FEM EM solver. However, some tests [83, 84] were also done using WIPL-D, a commercial EM solver-based MoM –method of moments–. Here it is worth stressing that the virtual experiments were set looking to render them as close as possible to the real scenarios with the intention that the imaging kernel includes as much information as attainable. For example, the antenna model is highly accurate, including even the coaxial port models, instead of a more straightforward approach as source points.

The virtual validation produces, first, the electric field used to build the imaging operator, and second, the differential scattering parameters of mimicked clinical scenarios. Moreover, the computed EM field may indicate the power penetrating the head or the effect of the non-perfect attachment of the antennas to the head. In

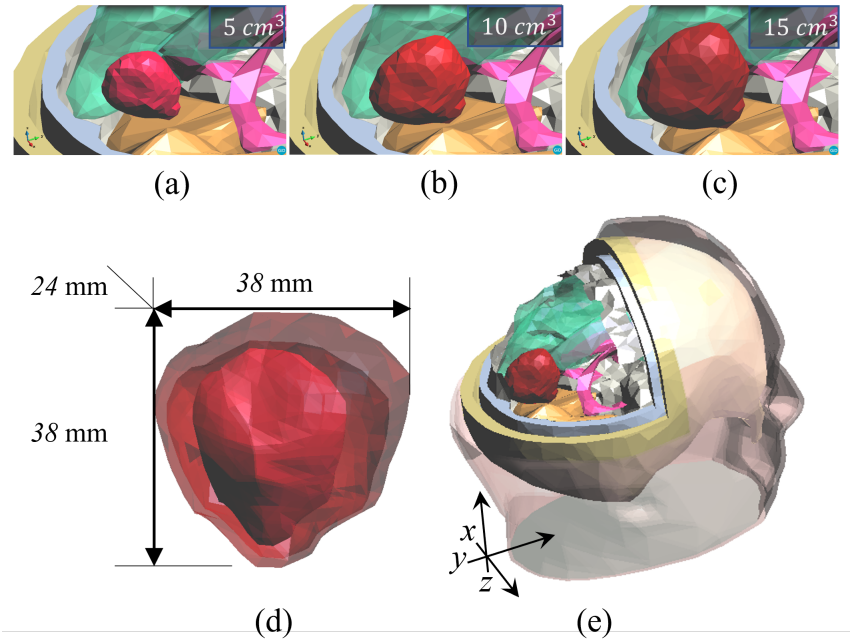

Fig. 3.19 Multi-tissue phantom (MTP); (a): brain and stroke phantom (dimensions in mm); (b): one hemisphere preparation; (c): two hemispheres with inserted stroke; (d): joined brain; (e): head phantom with immersed brain and filled up with electrically fat-mimicking liquid.

the case of the generation of the s-parameters, the numerical twin can evaluate the punctual antenna functioning aspects. Thus, the power of numerical validation relies on the ability to thoroughly study complex problems without the need to implement them or to know in advance what to expect. For instance, Fig. 3.19, illustrates a complex follow-up that can be explored, and that otherwise would be very difficult to implement.

3.3.2 Lab Experiment

The real-life experiments reported in this work can be divided by the version of the system used and the capability assessed. Then, the first section is considered the system 1.0, performing detection and localization of the stroke-affected area. Instead, the second part considers v.2.0 of the system and focused on imaging-based monitoring. Figure 3.20 depicts the top view of the experimental setup for the three main studied scenarios in the following.

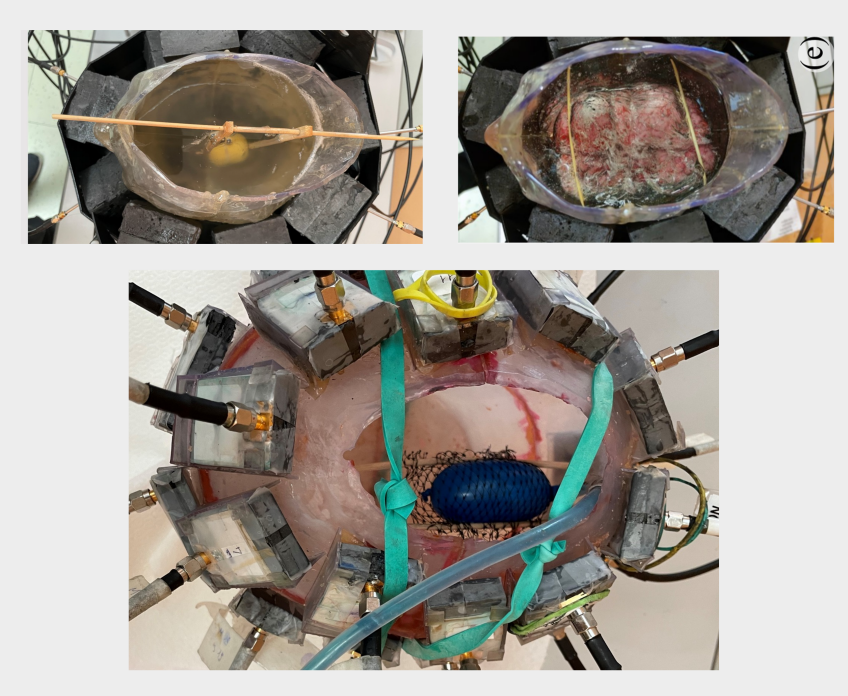

Fig. 3.20 Experiments setup. (Top):System v.1.0, left, homogeneous head, right, multi-tissue head. (Bottom):system v.2.0, homogeneous head, [40].

On the top-left of Figure 3.20, it can found the cases using the homogeneous head. In this case, the differential scenario considers at t_0 a healthy(empty) scenario, and at t_1 a scenario including the HEM/IS stroke, which is positioned using a pair of the coupled stick as can be seen from the image. The second case, Figure 3.20(top-right), represents the multi-tissue one and is assessed in a laboratory using a multi-stage experimental process that simulates brain stroke events. Similar to the homogeneous case, there are measured two sets considering both a healthy reference and an ill one. This setup is a simplified but similar experimental representation of the same fluctuation in the size of the stroke-affected brain area between time instants t_0 and t_1 as it would be in a clinical scenario. Moreover, to test the Hw-Sw-Calibration, transmission parameters of the auxiliary channel are measured in parallel. On the practical part, the first measurement in the MTP model is taken on the brain within the brain-tissue-filled target. Following that, the entire brain is carefully removed, one hemisphere at a time, using fishing lines to avoid it as much as possible the disturbances. The brain is gently loosened once it has been removed, allowing the stroke target to be put in one of the hemispheres. The brain is then sealed and tied

once again. Finally, following the relocation of the brain, this time due to the stroke, a new set of measurements is taken.

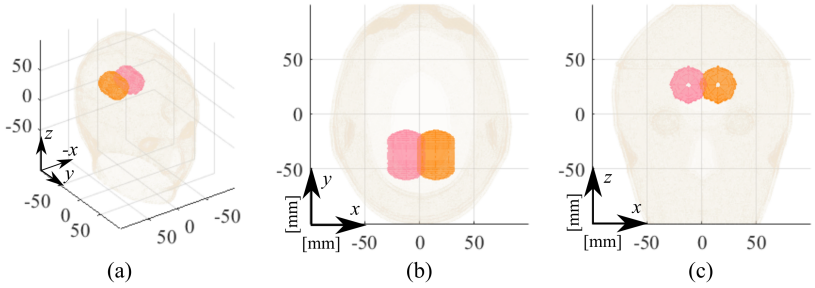

Fig. 3.21 HP estimated stroke position in the experimental testing; I: pink capsule and II: orange capsule. (a): 3-D view; (b): transverse view; (c): frontal view, [40].

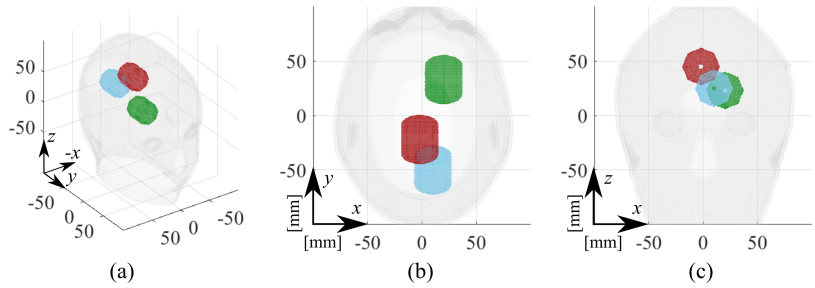

Fig. 3.22 MTP estimated stroke positions in the experimental testing; 1: blue capsule, 2: red capsule and 3: green capsule. (a): 3-D view; (b): transverse view; (c): frontal view, [40].

To assess the MWI system's performance, four cases of hemorrhagic and ischemic strokes in various postures are depicted and described for each phantom model as shown in Figs.3.21-3.22. Table 3.4 summarizes the used labels, and references all studied cases to its corresponding figure.

Table 3.4 Description of all the considered cases.[40]

Label	Stroke	Phantom	Position
ICH_HP-I	Hemorrhagic	Homogeneous	I, pink, Fig. 3.21
ICH_HP-II	Hemorrhagic	Homogeneous	II, orange, Fig. 3.21
IS_HP-I	Ischemic	Homogeneous	I, pink, Fig. 3.21
IS_HP-II	Ischemic	Homogeneous	II, orange, Fig. 3.21
ICH_MTP-1	Hemorrhagic	Multi-tissue	1, blue, Fig. 3.22
ICH_MTP-3	Hemorrhagic	Multi-tissue	3, red, Fig. 3.22
IS_MTP-2	Ischemic	Multi-tissue	2, green, Fig. 3.22
IS_MTP-3	Ischemic	Multi-tissue	3, green, Fig. 3.22

In the case of non-static stroke a three-phase experiment is performed, in which a stroke progresses from a healthy state to a volume of 60 cm^3, in both ischemic and hemorrhagic instances, in order to test the MWI system's performance and assess its capabilities of tracking the pathology stage. The laboratory experiments were designed to mimic various stages of a brain stroke, from the initial deterioration of the illness through the recovery of the damaged area as a result of therapy. During each series of measurements, the target was successively filled with 20 cm^3 of the stroke-emulating liquid using a tube-syringe system, starting with the empty state and progressing to the worst (bigger stroke) scenario. In the range of the estimated resolution, these differences allowed us to assess around 2 cm extensions in the longitudinal direction (sagittal axes of the human head) (about 1 cm). In this case, the position of the stroke does not change.

To recreate the situation at multiple stages/locations, such as 20-0 cm^3, 40-20 cm^3, and 60-40 cm^3, the gathered data were fed into the imaging method as differential scattering matrices. Finally, the same data were used to track the pathology shrinking/enlargement, based on the real part of the dielectric contrast map.

Chapter 4

Validation and Discussion

We have covered the inverse problem fundamentals, the principle and potential of MWI in the case of brain stroke, and the design of a custom prototype (software and hardware). Hence, we have all the tools needed for moving the system validation. This chapter covers the two iterations of the developed MWI system, considering both a numerical part using high-realistic virtual twin models and then an experimental one using lab mimicked scenarios.

Thus, the chapter is structured in two main parts, where different capability tests are performed for each system version. In the first case, the testing on the system v.1.0 focuses on the preliminary imaging validation and hardware setup. This part explores, first, the development of faithful twin numerical models, the build of the imaging kernel, and virtual experiments. Then, it aims to validate: 1. The concept of a modular antenna with an integrated solid matching medium [62], an essential feature from the practical point of view since it avoids the cumbersome use of liquid-based matching. 2. The whole system functioning in complex mimicked stroke scenarios is validated numerically [39], and experimentally [65, 40], corroborating their agreement and validity as a design tool. The second part of the chapter, on the other hand, concentrates on a new system design, i.e., v.2.0, that improves the portability via the use of more compact and flexible antennas and the reduction of the number of them while keeping the use of the discrete custom-made matching medium and imaging features [82, 75]. In this case, the validation turns mainly on the capability to follow up the continuous progression of hemorrhage and ischemia

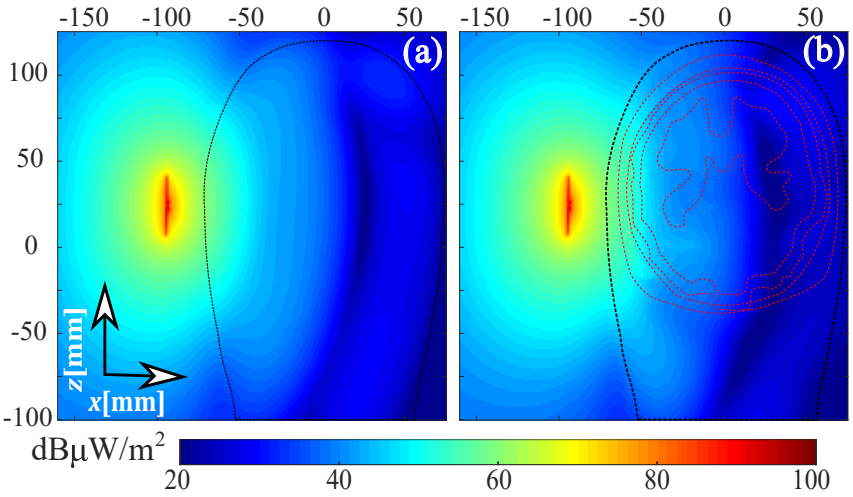

Fig. 4.1 Power density distribution at 1 GHz placing the monopole antenna immersed in the coupling medium infinitely extended around the head, coronal view; (a): UH model; (b) MTH model.([62] ©2021 IEEE)

zones with centimetric spatial resolution and to provide information on whether the stroke is growing or shrinking.

Finally, the chapter concludes with overall system analysis, identifying its novelties, main features, and limitations to be improved.

4.1 System v.1.0: Modularity and Low complexity

4.1.1 Brick Antenna

As aforementioned in the description of the MWI system, the antenna is a determinant element that characterizes the general performance, intrinsically linked with its reached power penetration and reflection and transmission coefficients. Thus, this section evaluates the first proposed antenna for diagnosing and monitoring cerebrovascular pathologies, consisting of a single antenna unit (radiating element and discrete coupling medium). Now, considering the traditional approach submerges the radiating element in an extended medium, it is considered the best-case scenario. So, the first analysis, power density distribution, is done numerically using detailed models and the full-wave solver of WIPL-D Pro software, which is based on method-of-moments with high-order basis functions. This analysis simulates the printed

monopole within an infinitely extended coupling medium (i.e., equivalent to having a liquid coupling medium) surrounding the head, which is modeled as both, a single and uniform tissue one and a multiple-tissue one, having the electric properties of its respective tissue/organ. These are named “UH”and “MTH”, respectively.

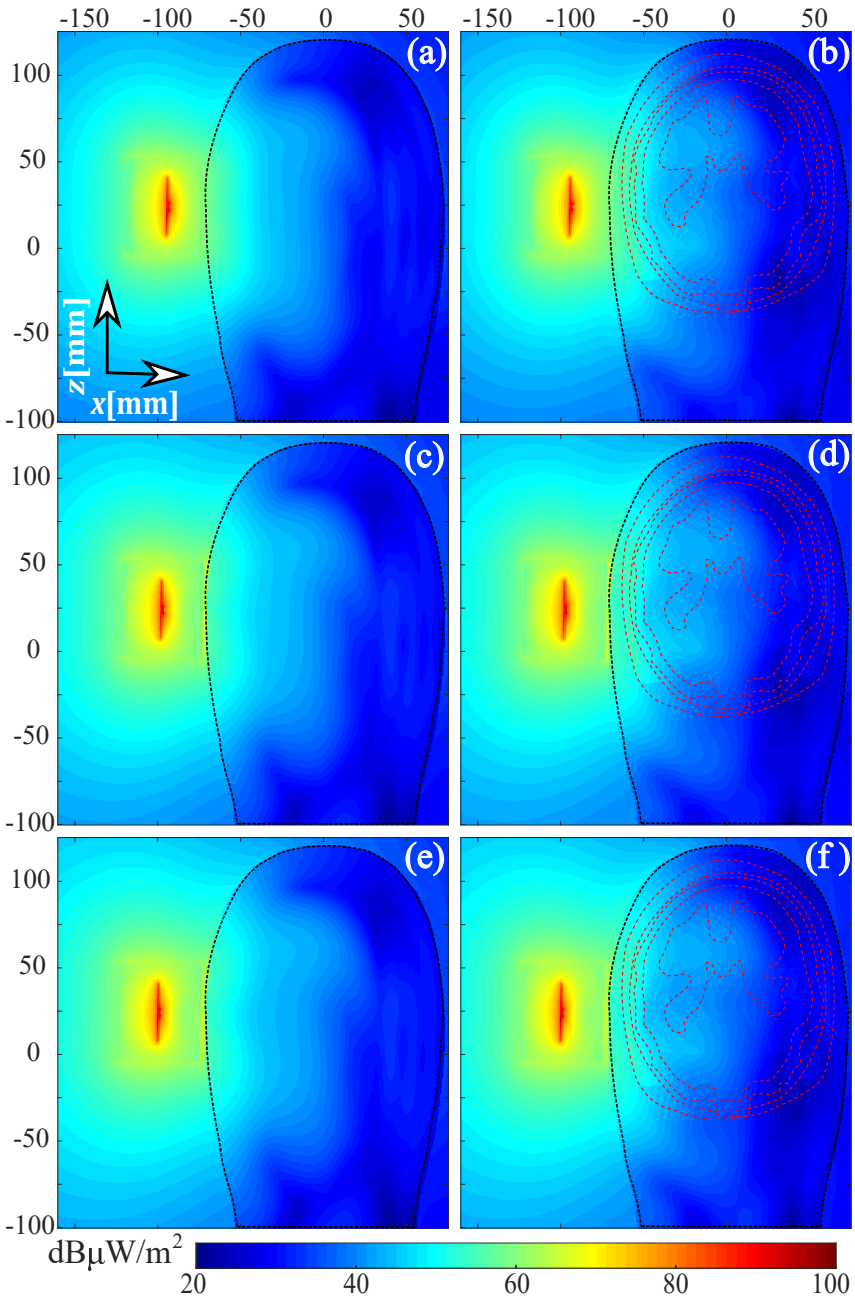

Fig. 4.2 Power density distribution at 1 GHz placing the brick antenna at different air-gap distances from the head surface, coronal view; left column: UH model, right column: MTH model; (a)-(b): no gap; (c)-(d): 1 mm gap, (e)-(f): 3 mm gap.([62] ©2021 IEEE)

Figure 4.1 illustrates the coronal view of the power density distribution cut at the middle of the head when an antenna is placed laterally. These results show the power impinged by the antenna penetrates the head in either case, overpassing the bone and CSF area. Once revealed, an adequated penetration in the reference case, the successive analysis considers the discrete antenna module, i.e., the brick-shaped antenna facing the head models, while the background is air. The examination considers then the minor air gap variations in the interface between the head and the brick frontal plane, which can happen during the experimental stage. Analogously, Fig. 4.2 presents the resultant power distribution for the cases 0 mm (perfect adhesion), 1 mm and 3 mm, top to bottom, for the UH model, to the left, and MTH, to the right. These results reflect the limited effect on the power density distribution of the limitation of the coupling medium (i.e., using the brick antenna) and the presence of small air gaps between the brick antenna and the head surface compared to the best-case scenario. Hence, numerical power distribution analysis confirms the validity of the antenna design in terms of penetration for the aimed purpose.

The second studied parameter is the reflection coefficient, S_{11}, starting with the numerical scenario and then with the experimental equivalent. Here the experiment considers a couple of antennas named "A1" and "A2"m which are positioned laterally to a UH head phantom (see Fig. 4.4(b)). Figure 4.3(a–b) reports the reflections coefficients for both cases, showing a good matching around 1 GHz. The numerical

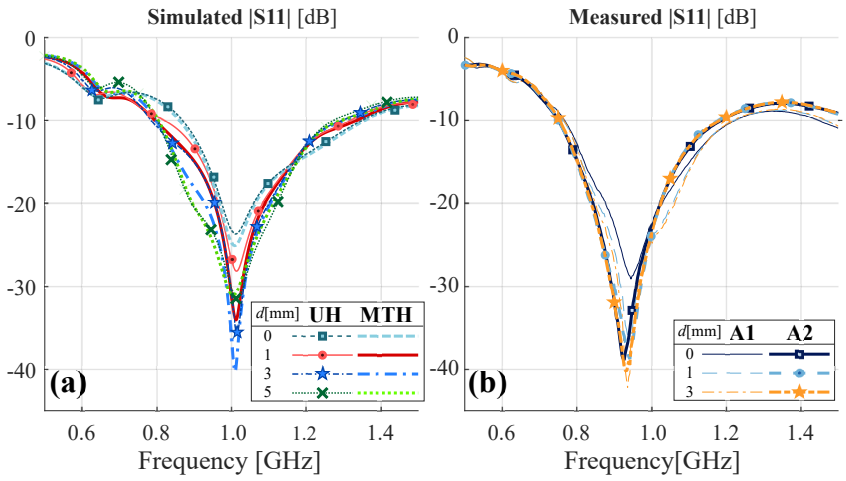

Fig. 4.3 Reflection coefficient amplitude for different air-gaps between the brick and the head surface, d [mm]. (a): simulations, considering the two head models (b): measurements, considering two realized antennas.([62]©2021 IEEE)

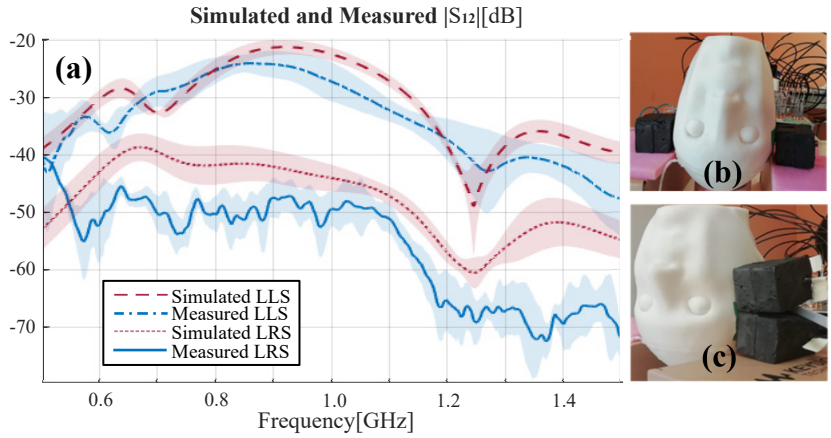

Fig. 4.4 (a): Simulated and measured transmission coefficient amplitudes, $|S_{12}|$, for the LLS and LRS configurations; (b)-(c): experimental setup for the LRS and LLS configurations, respectively.([62]©2021 IEEE)

case indicates a minor variation regarding the head model and/or the air gaps as shown in Fig. 4.3(a), while the experimental results demonstrate a good agreement between the virtual counterpart with just a down-shift of the measured resonant frequency of about 50 MHz as shown in Fig. 4.3(b), possibly due to manufacturing inaccuracies. Overall, the antenna reaches a -10 dB bandwidth from 0.8 to 1.2 GHz. Extending the S-parameter study and considering the relevance of the transmission parameter for an MWI system, these were analyzed using two different scenarios with a couple of antennas. First, the S_{12} coefficient of aclose by antenna pair facing the UH phantom was assessed, labeled as "LLS" (see Fig. 4.4(c)). Then, the second scenario considers a left-to-right-side antenna pair, labeled as "LRS" (see Fig. 4.4(b)). Figure 4.4 shows the average values $|S_{12}|$, with the inner lines of a set of around ten simulations/measurements varying the position slightly and/or the orientation of the brick antennas, and highlighting the range with the color bands. The results compare the numerical parameters with the measured data while is used the UH model and estimated air gap of 3 mm, finding an agreement with each other for both antenna configurations, though the measured LRS one (i.e., with opposite antennas) has a less smooth behavior, possibly due to external and non modeled interference. Besides, all transmission coefficients are well above the VNA noise floor [57].

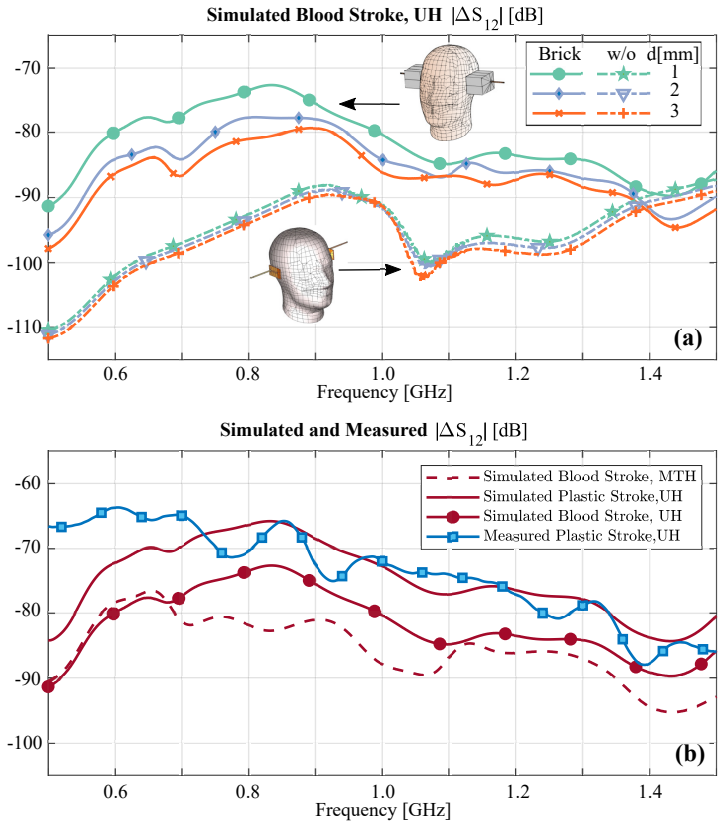

Fig. 4.5 Differential transmission coefficients, LRS configuration; (a): simulated blood stoke using an antenna pair with and without the dielectric bricks; (b): simulated and measured plastic/blood stoke with a pair of brick antennas.([62] ©2021 IEEE)

The last assessment of the brick antennas as a single element consists of introducing a 12.5 mm-radius sphere, mimicking a stroke in the middle of the head, while these are in the LRS configuration (i.e., the worst-case scenario), and then computing the differential transmission coefficient, ΔS_{12} taking the difference between the cases with and without the stroke. This test aims to evaluate the antenna capabilities in an operational monitoring environment. Hence, considering the numerical part, the stroke properties are set first to the blood ones, $\varepsilon_r = 61$ and $\sigma = 1.6$ S/m at 1 GHz, and then to lossless plastic, $\varepsilon_r = 2$ at 1 GHz. The latter, the plastic ball, was considered for experimental convenience at the moment and because it still has representative contrast that allowed the preliminary experimental validation of the antenna. The synthetic hemorrhagic scenarios consider the cases using a brick-shaped module and an antenna without the coupling medium, demonstrating better field penetration if the brick is present, even for different air gaps, as shown in

Fig. 4.5(a). Moreover, two additional numerical cases considering the UH and the MTH are tested, reported in Fig. 4.5(b). Moving to the experimental part, the plastic sphere scenario was measured with the UH head, presenting a good agreement and to some extent validating the virtual twin as an instrument to evaluate the capabilities of the system.

In summary, the preliminary assessment of the modular brick antenna reveals an adequate EM wave penetration inside the head and the potential to discriminate the presence of a small target (stroke). In the following, a system composed of a 24-antenna, brick-shaped array conforming to the head is tested in different mimicked clinical scenarios.

4.1.2 Whole system: Numerical Validation

The numerical modeling of the system is an essential instrument for the design and validation of an MWI system. Thus, the numerical analysis has multiple purposes. First, it speed-up and supports the design process allowing us to foresee the experimental part under some assumptions, which means that we can split the whole engineering problem into small pieces and thus, for example, studying just aspects such as the detection capabilities of the imaging algorithm while we assume noiseless data. Hence, the virtual instruments are vital analysis support for the pre/post-experiment. The second purpose, which in the end will extend to the real-life operation, lies in building and testing the capabilities imaging kernel.

In the following, numerical validation is developed in two phases. In the first part, it is considered the case of using UH, while, in the second one, the MTH head is used. For both cases, the effect of white noise applied to the S-parameter on the retrieved images is approached.

Uniform Average Head and Detection

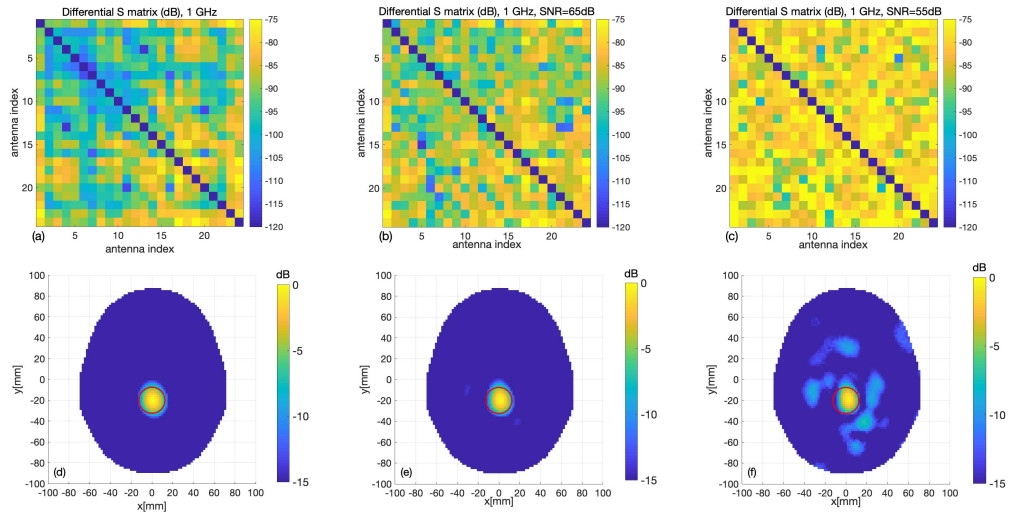

Fig. 4.6 Digital twin: case of a target plastic sphere; the exact sphere location and shape are indicated by red circles; (**a**–**c**) differential scattering matrices, and (**d**–**f**) cross-sections of the reconstructed images at the sphere center, for different values of the signal-to-noise ratio (SNR) (left column: no noise, middle column: SNR = 65 dB , right column: SNR = 55 dB)[65].

The first considered case consists of a single tissue head with the average properties of the head and a 1.25 cm-radius spherical target as the stroke, which initially is set as a plastic one. Then, as a benchmark, a noiseless reconstruction is performed, and later two cases adding Gaussian white noise with SNR levels of 65 dB and 55 dB to the simulated S-matrices of the cases with and without the stroke, respectively. Figure 4.6 summarizes the results, presenting at the top the magnitude in dB scale of the differential scattering matrices, where the reflection contributions are omitted in agreement with the experimental procedures. Instead, the bottom row presents a transverse view of the 3-D normalized dielectric contrast mapping retrieved from the imaging algorithm, centered in the middle of the stroke. From the columns, it is worth noticing that the white noise, even when the SNR is comparable to or higher than the maximum values of the differential S-matrix, slightly corrupts the output image, and the unavoidable artifacts do not restrict the interpretation of the results, until some extent.

After the first validation has shown promising results, the experiment is repeated, changing the stroke's properties to the blood ones, summarizing the results in Fig. 4.7.

These results are comparable to the previous ones, just presenting a not meaningful increase of the artifact in the case with a higher level of noise, expecting thus a homologous experimental scenario would reach similar results.

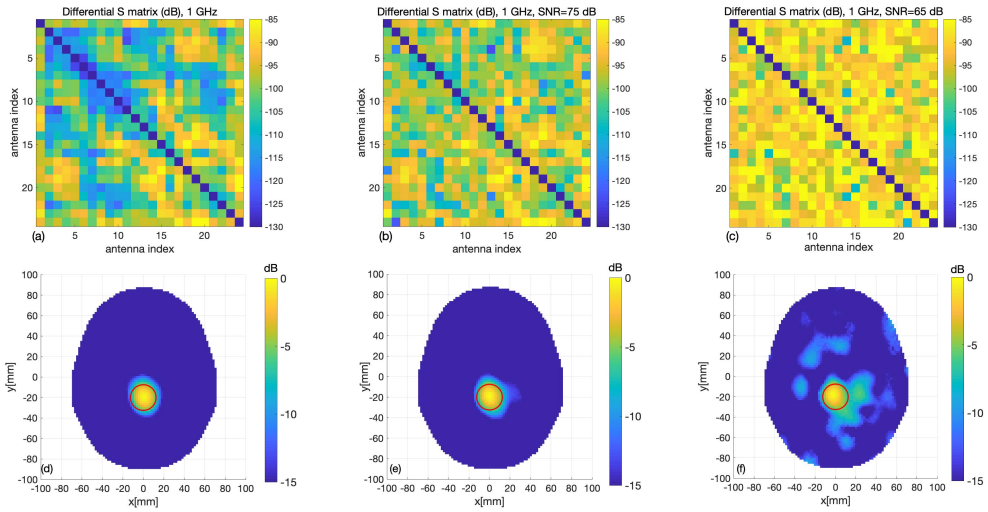

Fig. 4.7 Digital twin: case of a target blood sphere; the exact sphere location and shape are indicated by red circles. (**a**–**c**) Differential scattering matrices; (**d**–**f**) cross-sections of the reconstructed images at the sphere center, for different values of the signal-to-noise ratio (left column: no noise, middle column: SNR = 75 dB , right column: SNR = 65 dB)[65].

Multi-Tissue Head and Monitoring

This section performs the numerical analysis of the functioning of the imaging scheme and the system when the studied head is a multi-tissue head, and the objective of the imaging is to follow up on the progression of the hemorrhagic and ischemic stroke. Here, the full-wave simulations are performed using our in-house FEM solver. Then, first, to corroborate the imaging, the antennas performances of the 24 antennas are verified, checking their reflection and transmissions parameters and the differential values during the different monitoring stages. Then, the imaging is tested, approaching the stroke evolution.

Starting with the validation of the reflections, the Fig. 4.8 presents them, showing a -10 dB frequency band from 800 MHz to 1.12 GHz for all antennas, in agreement with the single antenna validation presented at the beginning of this chapter [62], though variations between the different antenna responses, which can be explained by variability in the proximity and rotation of the antennas respect to the head. The

transmission coefficient, the base of differential input of the imaging algorithm, is checked considering the case for one of the lateral antennas referred to the other 23, and reported in Fig. 4.9, which are all above -90 dB.

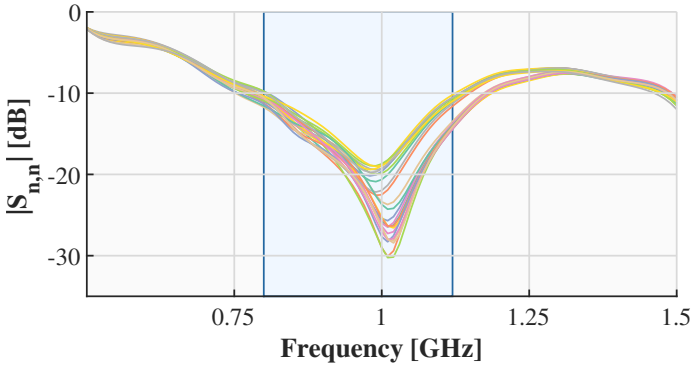

Fig. 4.8 Reflection coefficient amplitude; each line corresponds to the $|S_{n,n}|$ in dB for the n-th antenna of the MWI system with $n = 1,\ldots,24$, [39] ©2021 IEEE.

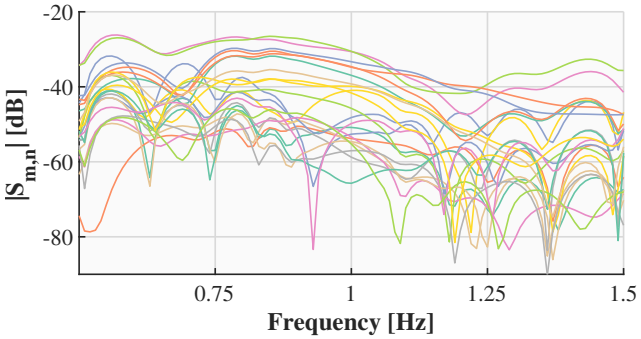

Fig. 4.9 Transmission coefficient amplitude; each line corresponds to the $|S_{m,n}|$ in dB with $n = 1$ (transmitting antenna) and $m = 2,\ldots,24$ (receiving antennas), [39] ©2021 IEEE.

Two primary stages of monitoring will be considered. The first stage is referred to as "detection phase," when the patient goes from being healthy to having an onset stroke. In this scenario, the healthy head is at time instant t_0, and the stroke is at time instant t_1, with a 0.88 cm^3 half-sphere shape (see HS stroke in Fig. 4.10). On the other hand, the second stage is called "Post-onset monitoring." The half-sphere stroke is at t_0, while at t_1, the shape is stretched, forming a capsule with a volume of 3.1 cm^3 (see CAP stroke in Fig. 4.10).

Because the stroke dimensions and growth are dependent on a variety of factors, including their location in the brain, the involved blood vessels, and the time of diagnosis, the dimensions and variations assumed here are chosen to demonstrate the

ultimate potential of the proposed technology and are related to the MWI system's resolution at 1 GHz, which is around 1 cm. Examples with different shapes, including a medical-based one, will be presented during the validation of the second version of the device.

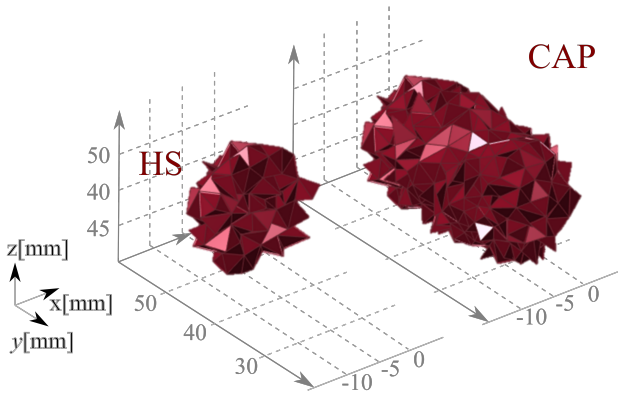

Fig. 4.10 Selection of tetrahedrons for ideal contrast; (left): HS case; (right): CAP case, [39]©2021 IEEE.

To evaluate the performance of the discretized scattering operator $\mathcal{L}$, the "ideal" contrast of the above-mentioned monitoring cases is projected onto its right singular vectors v_n that span the discretized contrast space. A contrast of 1 in the tetrahedrons where the stroke is present and 0 everywhere else is considered optimal. Figure 4.10 shows the selected tetrahedrons when the HS or CAP case is used. The generated projections, displayed in Fig. 4.11, can be deemed the best possible reconstructions for the two monitoring cases using the modeled MWI system.

Once validated the spread capabilities of the system the monitoring capabilities of the MWI system were analyzed by feeding simulated differential scattering matrices into the TSVD imaging algorithm. The amplitude of the transmission coefficients of one antenna with respect to the others is reported in Fig. 4.12 to emphasize the magnitude of the differential scattering parameters. Ischemic and hemorrhagic strokes are considered alongside the two monitoring cases previously outlined. Most differential coefficients are above -120 dB in all circumstances, being a more difficult situation from the technical perspective, requiring a VNA with medium dynamic range performance [57].

In comparison to post-onset monitoring, where the stroke volume variation is more considerable, the detection phase correlates to lower transmission coefficients.

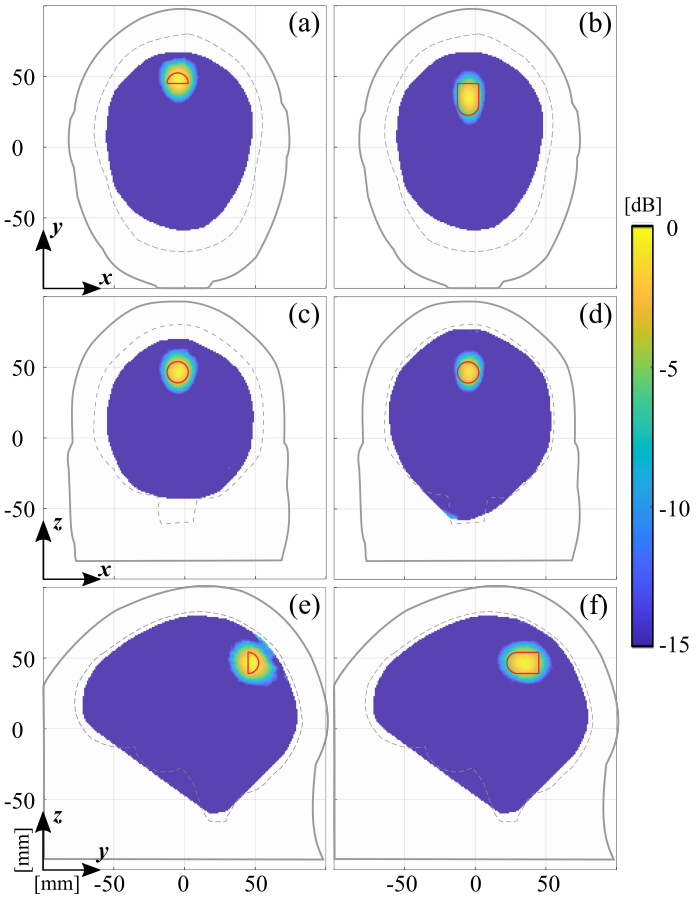

Fig. 4.11 Projection of the ideal dielectric contrast on the right singular vectors of the discretized scattering operator; the exact stroke location and shape are indicated by red contours. Left: HS case; right: CAP case. (a)-(b): transverse plane view; (c)-(d): frontal plane view; (e)-(f): sagittal plane view, [39]©2021 IEEE.

The case of a hemorrhagic stroke is examined in Fig. 4.13. The first column refers to the detection phase, whereas the second column corresponds to post-onset monitoring. The differential scattering matrices are reported in the first row, and the reconstructed images in the three main views are shown in the following rows. In both cases, good contrast reconstructions are achieved, nearly equal to the corresponding projections seen in Fig. 4.11, demonstrating the evolution of the stroke region from the half-sphere to the capsule-shape. Then, in Fig. 4.14, the same analysis is given for the ischemic stroke.

Furthermore, Figs. 4.15 and 4.16 show the identical scenarios as Figs. 4.13 and 4.14, but with the scattering matrices subjected to noise. The synthetic data

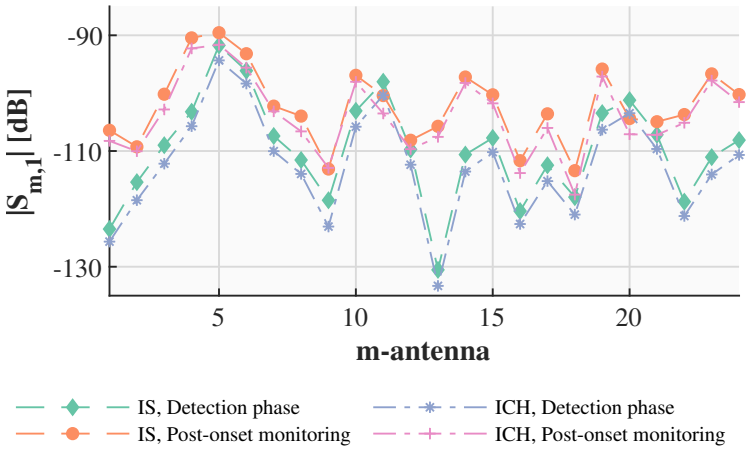

Fig. 4.12 Differential transmission coefficient amplitude of a lateral antenna with respect to the other antennas, [39]©2021 IEEE.

is corrupted by additive white Gaussian noise at two levels, assuming a 6 dBm input (source) power, the SNR is set to 100 dB for the first columns and 90 dB for the second columns. The noise is introduced separately to the scattering matrices simulated at each time instant, which are then differentiated to generate the noisy differential scattering matrices used as input to the imaging algorithm. Even though the matrix pattern appears to be greatly influenced by the extra noise, the expected contrast is successfully reconstructed in all scenarios.

Until this point, the MWI prototype capabilities for clinical follow-up brain stroke were tested using a numerical analysis that used a bespoke 3-D high-fidelity numerical model of the system. According to the numerical analysis, the device is capable of imaging ischemic and hemorrhagic strokes with dimensions and/or fluctuations of the order of 1 cm. Given the general reliability of the virtual evaluation, the next phase is to conduct actual experiments that replicate the simulated events in order to complete the system's final experimental assessment. It's worth emphasizing that the high-fidelity numerical model will still play a key role in this process since it will offer the device-specific mathematical operators required to generate the image kernel in an accurate and trustworthy manner.

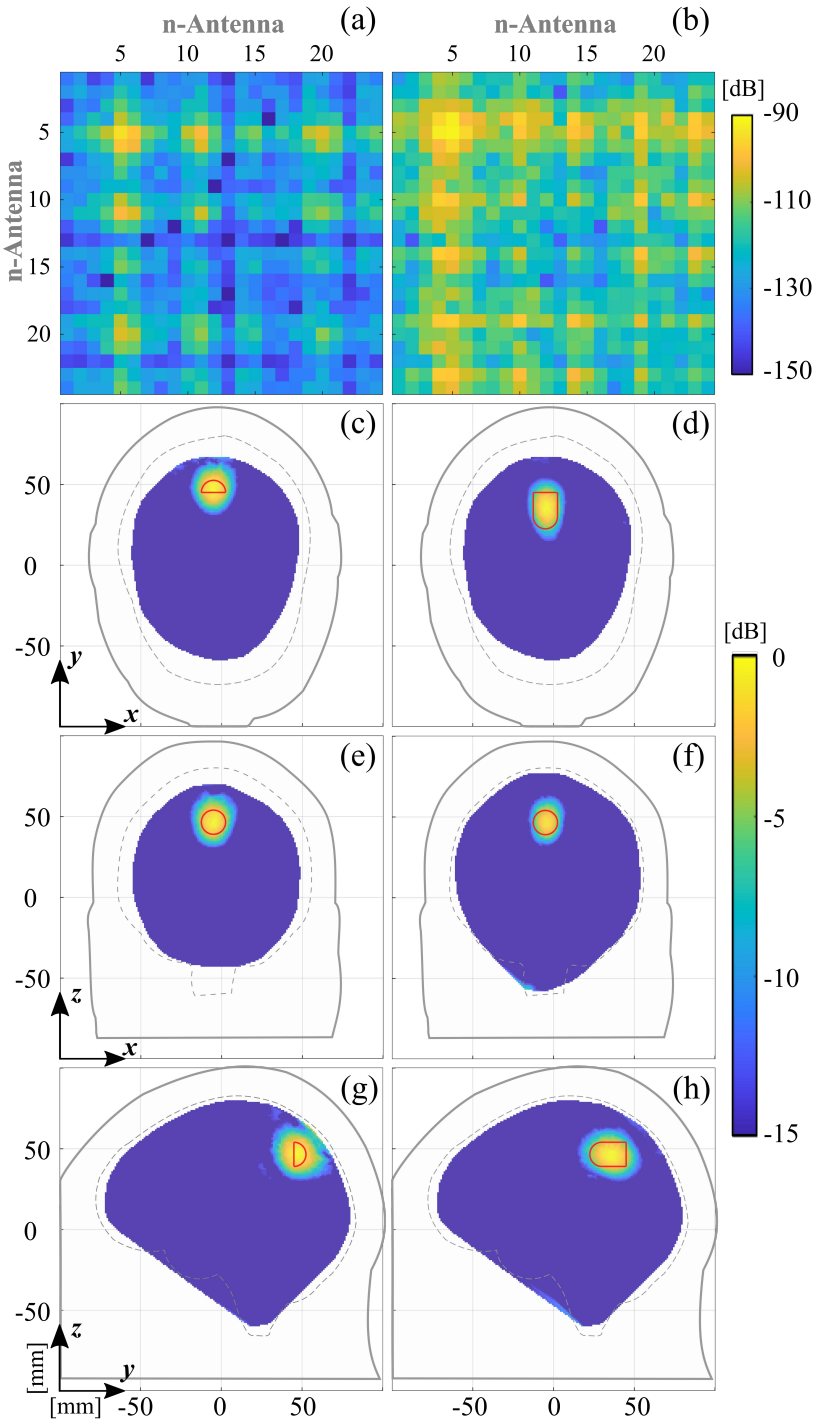

Fig. 4.13 Reconstructed images for a hemorrhagic stroke; the exact stroke location and shape are indicated by red contours. Left: detection phase; right: post-onset monitoring. (a)-(b): differential scattering matrices; (c)-(d):transverse plane view; (e)-(f): frontal plane view; (g)-(h): sagittal plane view.([39]©2021 IEEE)

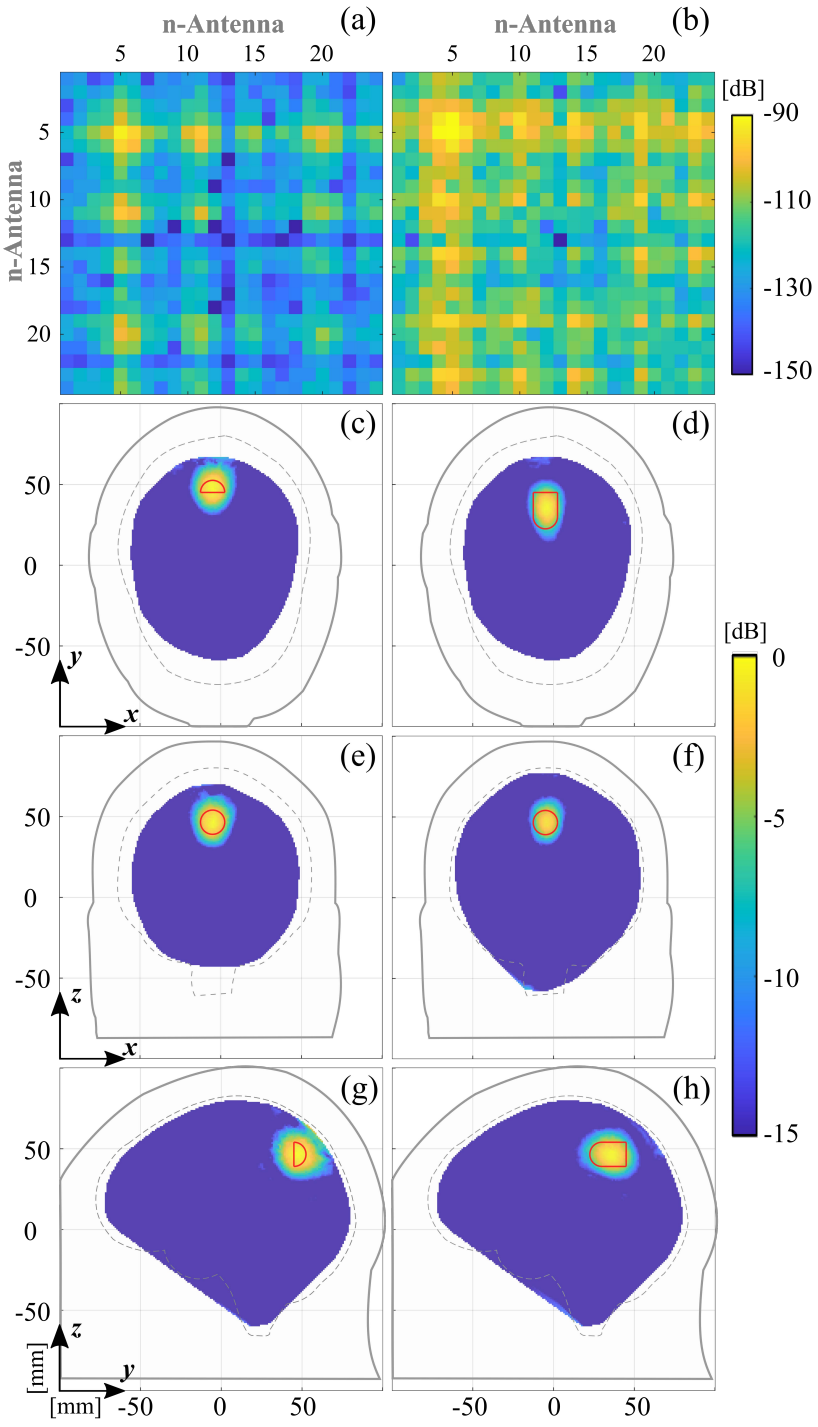

Fig. 4.14 Reconstructed images for a ischemic stroke; the exact stroke location and shape are indicated by red contours. Left: detection phase; right: post-onset monitoring. (a)-(b): differential scattering matrices; (c)-(d):transverse plane view; (e)-(f): frontal plane view; (g)-(h): sagittal plane view.([39]©2021 IEEE)

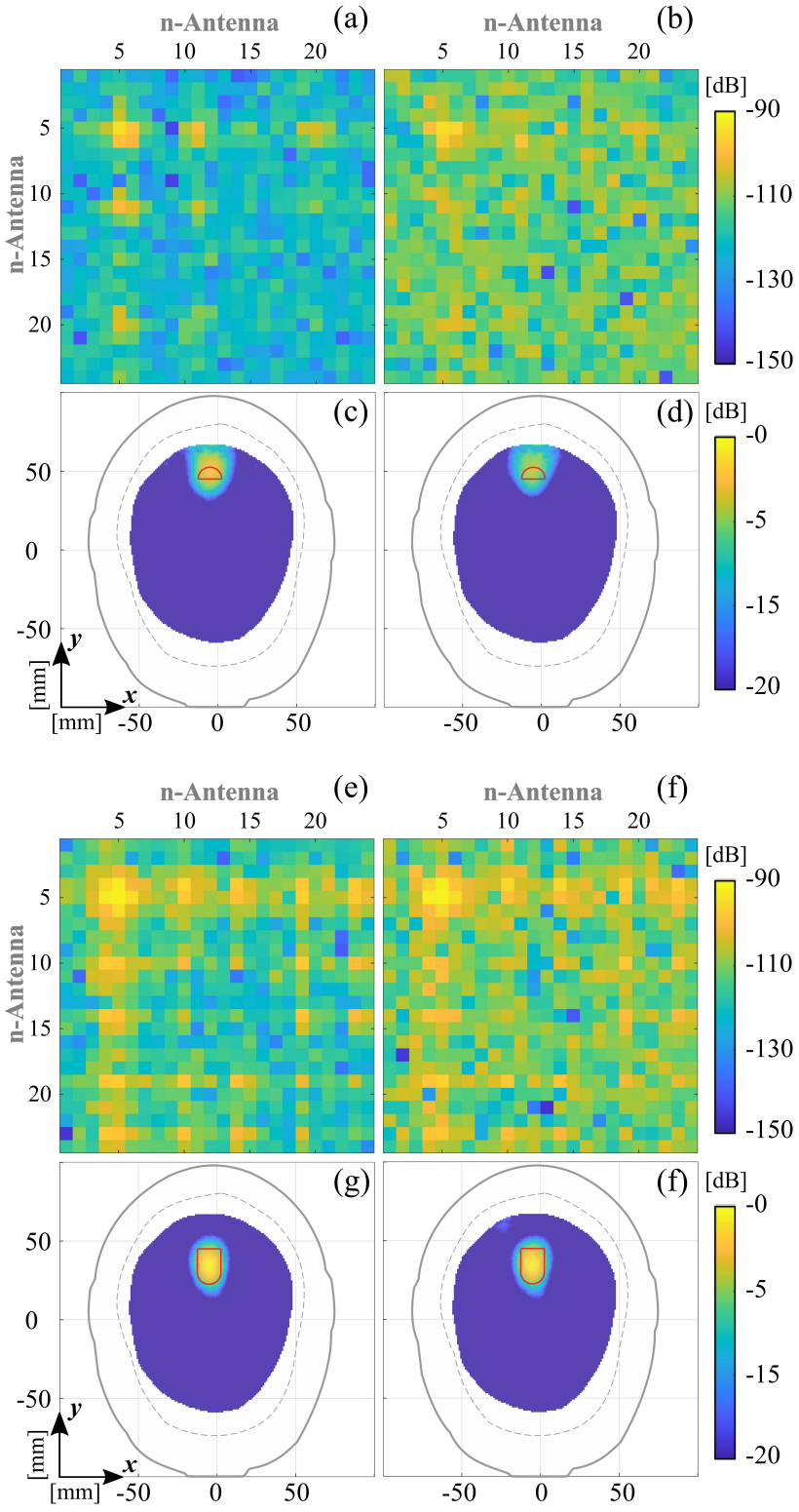

Fig. 4.15 Reconstructed images for a hemorrhagic stroke; the exact stroke location and shape are indicated by red contours. Left: SNR = 100 dB; right: SNR = 90 dB. (a)-(b): differential scattering matrices, detection phase; (c)-(d): reconstructed images in the transverse plane, detection phase; (e)-(f): differential scattering matrices, post-onset monitoring; (g)-(h): reconstructed images in the transverse plane, post-onset monitoring.([39]©2021 IEEE)

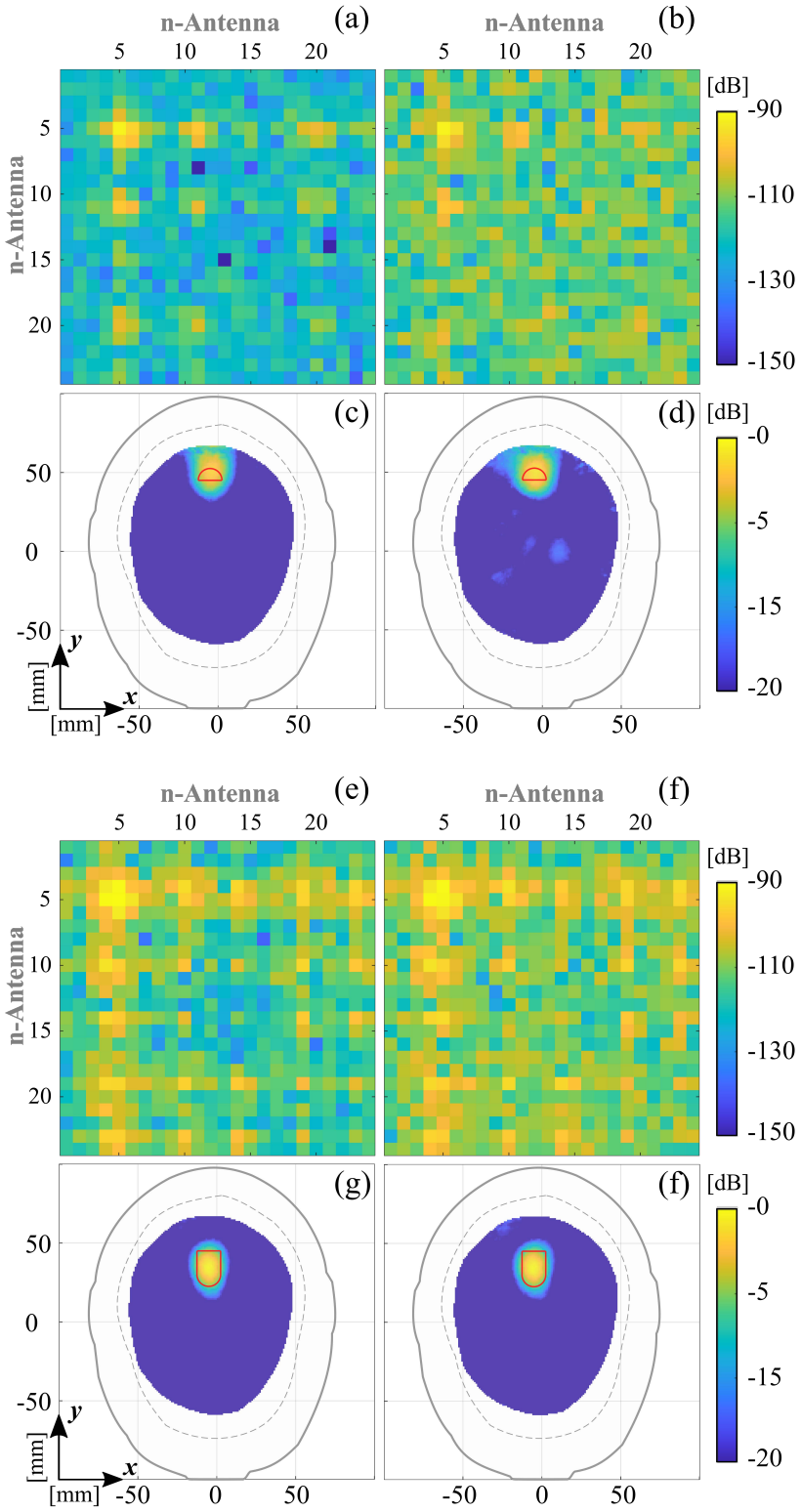

Fig. 4.16 Reconstructed images for a ischemic stroke; the exact stroke location and shape are indicated by red contours. Left: SNR = 100 dB; right: SNR = 90 dB. (a)-(b): differential scattering matrices, detection phase; (c)-(d): reconstructed images in the transverse plane, detection phase; (e)-(f): differential scattering matrices, post-onset monitoring; (g)-(h): reconstructed images in the transverse plane, post-onset monitoring.([39]©2021 IEEE)

4.1.3 Whole System: Experimental Validation

The natural step after the numerical validation is the experimental testing of similar scenarios to the ones virtually considered. Then using the experimental setup and procedures described in chapter 3, this section presents a multi-stage experimental validation of version 1.0 of the system. Starting with the average head case, the first part of the section shows the results considering initially the plastic target [65], and then a target mimicking both types of stroke [40]. Instead, the second stage presents the results using the multi-tissue phantom, i.e. the one using the calf-made one, while both types of stroke are approached. For all cases, false-positive cases are studied.

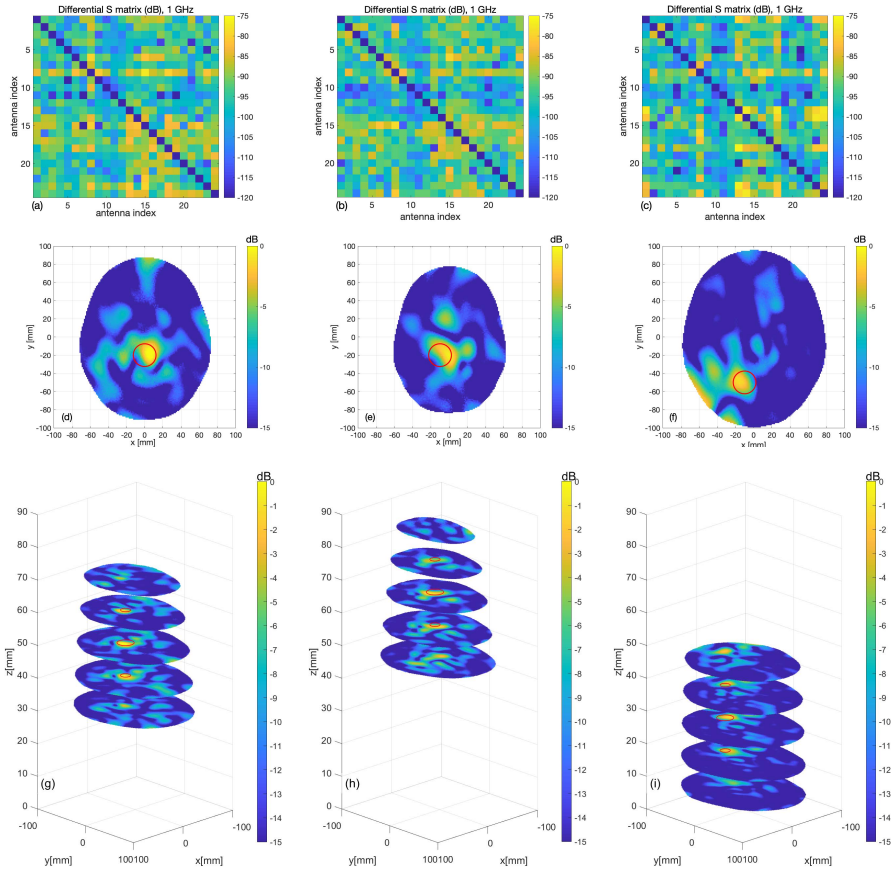

Fig. 4.17 Measurement results using a plastic target: (**a**–**c**) differential scattering matrices; (**d**–**f**) horizontal cross-sections at sphere center and (**g**–**i**) at the various levels, [65].

A spherical plastic target is the first one to be tested, while is used a single cavity filled with mimicked average brain liquid. The target is then placed in three different

locations, looking for a position approximated within the brain region. Following the differential approach of the imaging procedure, two data sets of measurements at different instants are taken for each retrieved image. The first one is without the stroke and the second one is with the stroke positioned inside the phantom. Then, because the systematic measurement errors are canceled out due to the differential and its effect diminishes substantially on the obtained qualitative imaging, here it is not applied VNA port calibration. Moreover, the time per set of measures was about 4 min, elapsing around 10 min for two measurement sets. While the data processing time needed by the TSVD algorithm for the inversion, which uses the operator generated during the virtual validation, is negligible being less than a 1 s.

Similarly, to the virtual case, Fig. 4.17 summarizes the result of the experimental validation, initially tested with the plastic target. So, the top row of Fig. 4.17(a–c) presents the differential 24×24 scattering matrix for the three different positions, excluding the self-term as these destabilize the solution, probably caused by the non-modeled variation near the resonance of the antennas generated by manufacturing inaccuracies. The remaining two rows are representations of the 3-D retrieved and normalized electric contrast, where the second one corresponds to the transverse plane view passing through the target center, and the last one is the exploded view.

After validate the system with the spherical plastic target, the next test considers an ellipsoidal target that mimics the hemorrhagic and ischemic stroke. In this case, two different positions were set trying to cover both brain hemispheres. Figure 4.18 summarizes the results labeling the cases as ICH-HP_I, IS-HP_I, ICH-HP_II, and IS-HP_II, where ICH and IS, stand for intracranial hemorrhage and ischemia, respectively, HP refers to homogeneous phantom, and I and II indicate the positions. Here it is worthy to highly, that the results were obtained using the software-hardware calibrated data. For further details refers to the previous chapter or [40].

Scaling the complexity of the scenarios, the last test of the system v.1.0 employed the multi-tissue phantom, while again both HEM and IS stroke were considered. These last experiment results are reported in Fig. 4.19, where MTP stands for multi-tissue phantom. Similarly, to the previous cases, the normalized amplitudes are depicted and the estimated position of the target is signaled with a red contour. In this last case, it was also used the calibrated data, reaching similar results to the homogeneous case, just with a major number of artifacts.

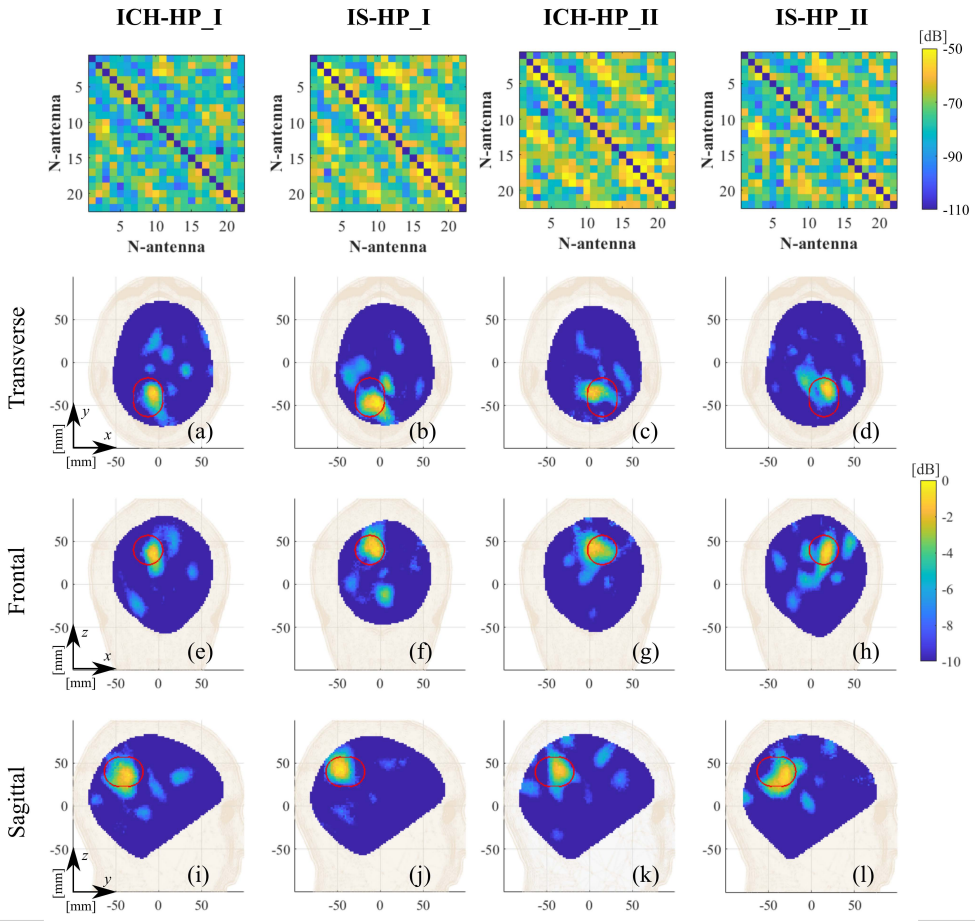

Fig. 4.18 Measurement results using a HEM and IS targets and an homogeneous phantom. (first row) and reconstructed normalized dielectric contrast values. Columns (from left to right): ICH-HP_I, IS-HP_I, ICH-HP_II and IS-HP_II. (a)-(d): transverse views; (e)-(h): frontal views; (i)-(l): sagittal views. The expected stroke area is indicated with a red line [40].

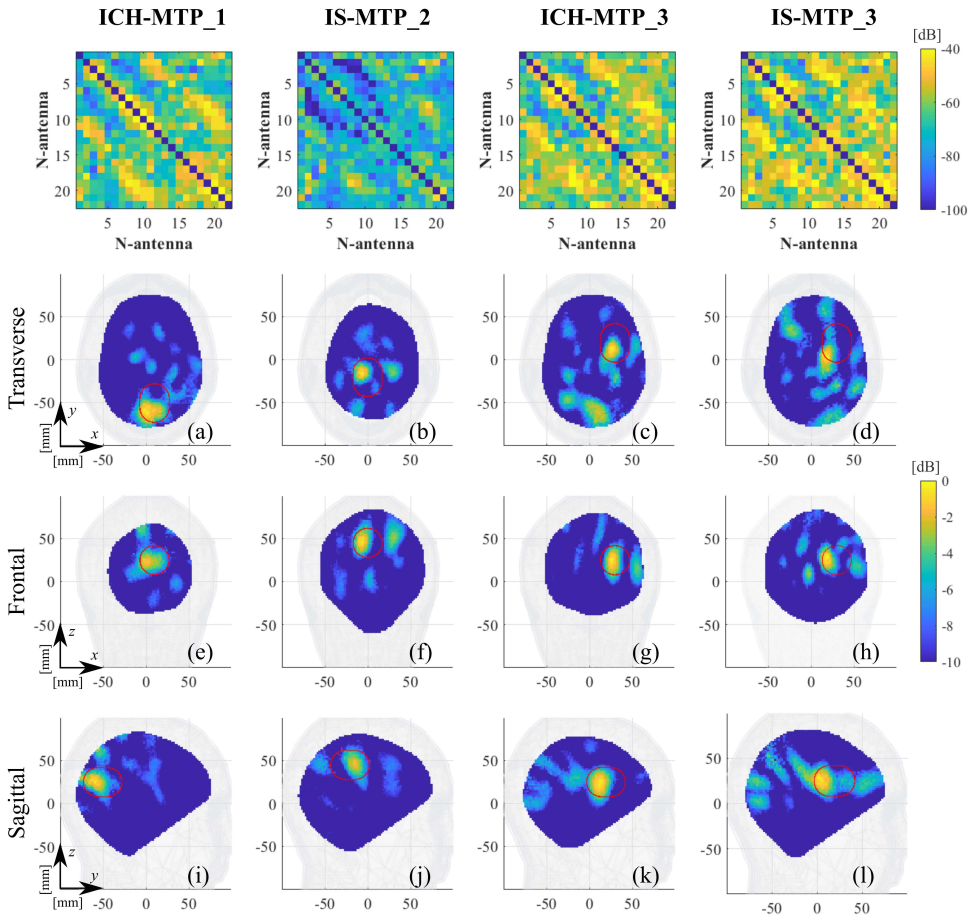

Fig. 4.19 Measurement results using a HEM and IS targets and an multi-tisse phantom. MTP Calibrated differential scatting matrices (first row), and reconstructed normalized dielectric contrast values. Columns (from left to right): ICH-MTP_1, IS-MTP_2, ICH-MTP_3 and IS-MTP_3. (a)-(d): transverse views; (e)-(h): frontal views; (i)-(l): sagittal views. The expected stroke area is indicated with a red line, [40].

To validate the measurements, false-positive and base tests are performed. The imaging reconstruction is tested using a differential scattering matrix of healthy cases only, obtained with the multi-tissue phantom. Hence, the retrieved reconstructions, reported in Fig. 4.20, are normalized to the maximum value of ICH-MTP_1 and cross-cut in their maximum. Three cases are reported with different time-lapses between measurement sets. Firstly, shown in Fig. 4.20(a), it considers a measured setup with an unaltered scenario. So that, the calf-made brain in the MTP is not removed between the measuring. This initial case presents a time distance of around 35 min between the two considered scattering matrix measurements. Instead, the last two cases are a more challenging scenario where, between the two considered measurement sets, the brain was removed and re-introduced in the head phantom. In Fig. 4.20(b), the time distance, between the two considered measurement sets, is around 1 hour and 45 min, while in Fig. 4.20(c) it is around 1 hour and 10 min.

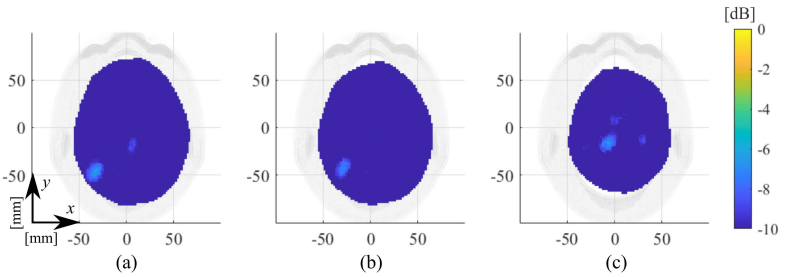

Fig. 4.20 Amplitude values of the reconstructed dielectric contrast for false-positive scenarios in the case of different time intervals; transverse views cut in their maximum, normalized to the maximum value of ICH-MTP_1. (a): 35 min; (b): 1 hour and 45 min; (c): 1 hour and 10 min, [40].

To verify that different measurements of the same scenario generate a similar reconstructed dielectric contrast, there are considered four consecutive measurement sets, starting with one healthy scenario, followed by two ICH target measurements, and finishing with a different healthy one. The first and second measurements are used to generate the reconstructed dielectric contrast in Fig. 4.21(a), corresponding to the ICH-MTP_1 case, also reported in Fig. 4.19(a). Then, the first re-test, illustrated in Fig. 4.21(b), is with the initial healthy scenario (i.e., first measurement set) and the second ICH target case (i.e., third measurement set). Instead, the second re-test, depicted in Fig. 4.21(c), takes into account the second ICH target case (i.e., third measurement set) and the last healthy scenario (i.e., fourth measurement set). Comparing the reconstructed dielectric contrast, it is evident that the imaging

algorithm is able to correctly recover the position of the stroke reconstructing a similar shape, and so confirming the repeatability of the measurement.

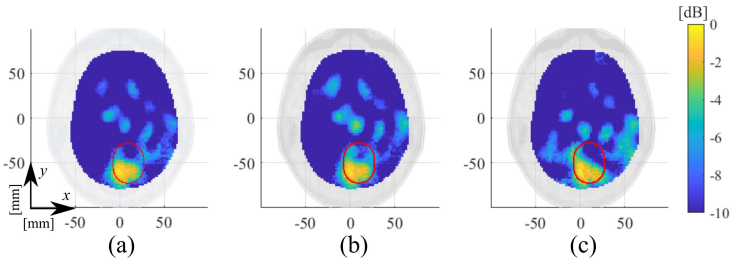

Fig. 4.21 Amplitude values of the reconstructed dielectric contrast for re-test experiment; transverse views cut in their maximum, normalized to the maximum value of ICH-MTP_1; (a): baseline; (b): re-test 1; (c): re-test 2, [40].

4.2 System v.2.0: Make it lighter and less bulky

Following the iterative methodology in this work, here is presented the second version of MWI system. This version, dubbed also v.2.0, aims for a lighter and less bulky prototype while keeping the benefits of the non-liquid coupling medium. Then, in a similar way to the validation of the first version, it consists initially of a numerical part, followed by the experimental one. In the specific, the experimental part focuses on the monitoring.

4.2.1 Numerical Validation

This section starts presenting the power density distribution at 1 GHz, generated by a couple of antennas placed conformal on the lateral of the head as shown in Fig. 4.22 at the top, coinciding with the position used later in the full array layout. For the head, two models are employed both a homogeneous one and a multi-tissue one, reported in the first and third, and second and fourth columns in Fig. 4.22, respectively. For the homogeneous case, the head model considers a 3-mm thickness container mimicking the resin and average brain tissue. The multi-tissue one, instead, includes the different organs and tissues, representing each one as homogeneous elements (see Fig. 4.23). It is worth mentioning that container here is considered the skin, even if cannot be noticed from the diagram.

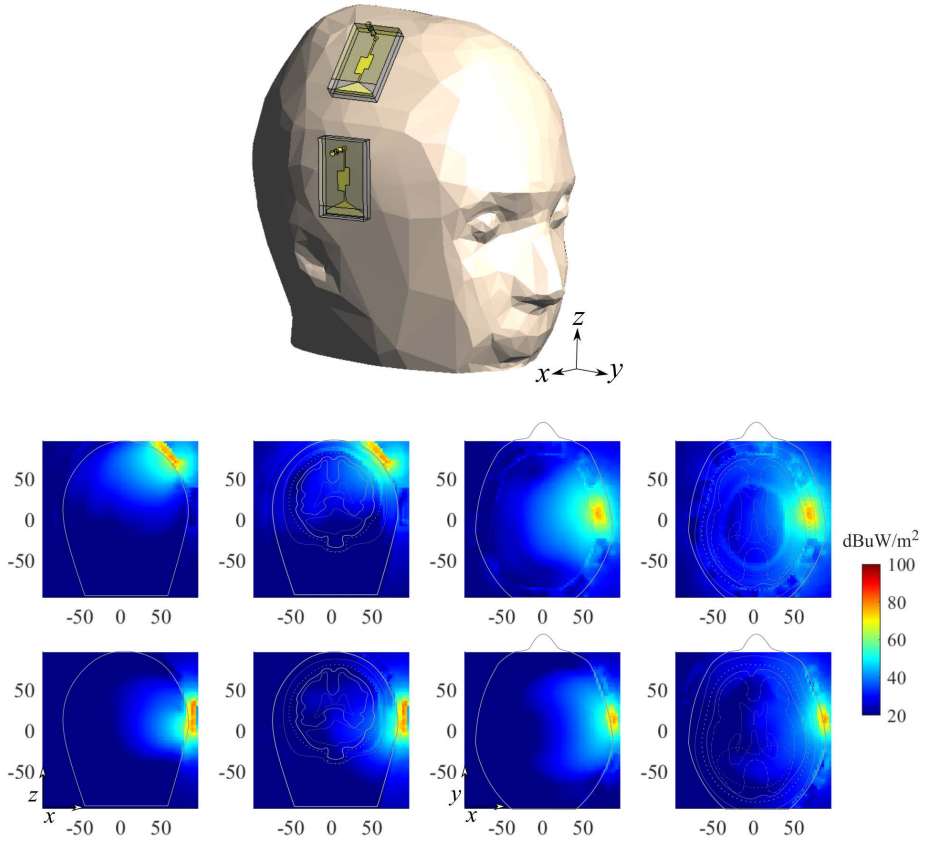

Fig. 4.22 Power density distribution at 1 GHz considering both an homogeneous, fist and third columns, and a multi-tissue head, second and forth columns.

The antennas are placed directly on the external head surface, so reducing the air gaps. The resulted power density distribution gives then an indication of the wave penetration, showing an adequate performance and coverage of the head since the MWI system used a 22-antenna array distributed in two conformal rings in the upper part of the head. These results are also in agreement with the power distributions of the first version of the system.

The next step covers the validation of the imaging capabilities of the system and presenting first the numerical results. The imaging test evaluates the variation of an anthropomorphic realistic hemorrhagic stroke, which is obtained from medical images as explained in the previous chapter [82]. The stroke occurs at the back of the head, around the occipital and parietal zones of the brain, and is a medical disorder that causes the visual system to fail, resulting in cortically-induced blindness [85]. Then, a three steps evolution was done, considering the cases 5 cm^3, 10 cm^3,

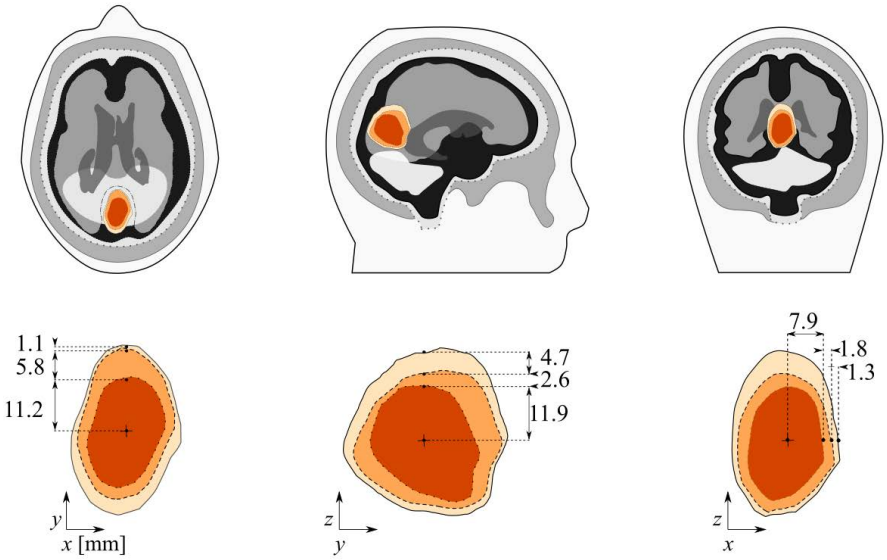

Fig. 4.23 Multi-tissue head model with emulated stroke evolution.

and 15 cm^3, indicated in red, orange, and yellow in Fig. 4.22, respectively. Notice, that this is a very challenging scenario in terms of resolution, working with axial variations in the order of half-centimeter.

Figure 4.24 summarizes the result for the two scenarios, where the differential variations consider always at t_0 the healthy state, i.e. empty stroke. In the figure, the top of each pair of rows illustrates the points(voxels) within the normalized contrast that are above -3 dB, giving a volumetric estimation of the retrieved stroke-affected zone (recall the here is used a 3-D algorithm). The bottom rows present the transverse views, cut in the middle of the targets, indicating with the red lines the contour of the actual stroke in the evaluated case, and the experimental case with circles indicating spheres with the respective volume. Also, the three first columns from left to right are zoom-up views of the zone of interest, and the rightest one is the whole view of the head.

Overall the retrieved contrast for both studied cases gives, first, clear detection of the target, second, and good estimation of the location of the stroke and three and indication of the change, being clear the growing-up of the stroke. The shape-recovery present also a good performance, though limited in part by the distortion of the operator. Here notice that the operator used in both cases is built using the electric fields from the average head. The effect of this distortion can be noticed more in 4.24(b), where the reconstruction shows some small artifacts and the shape

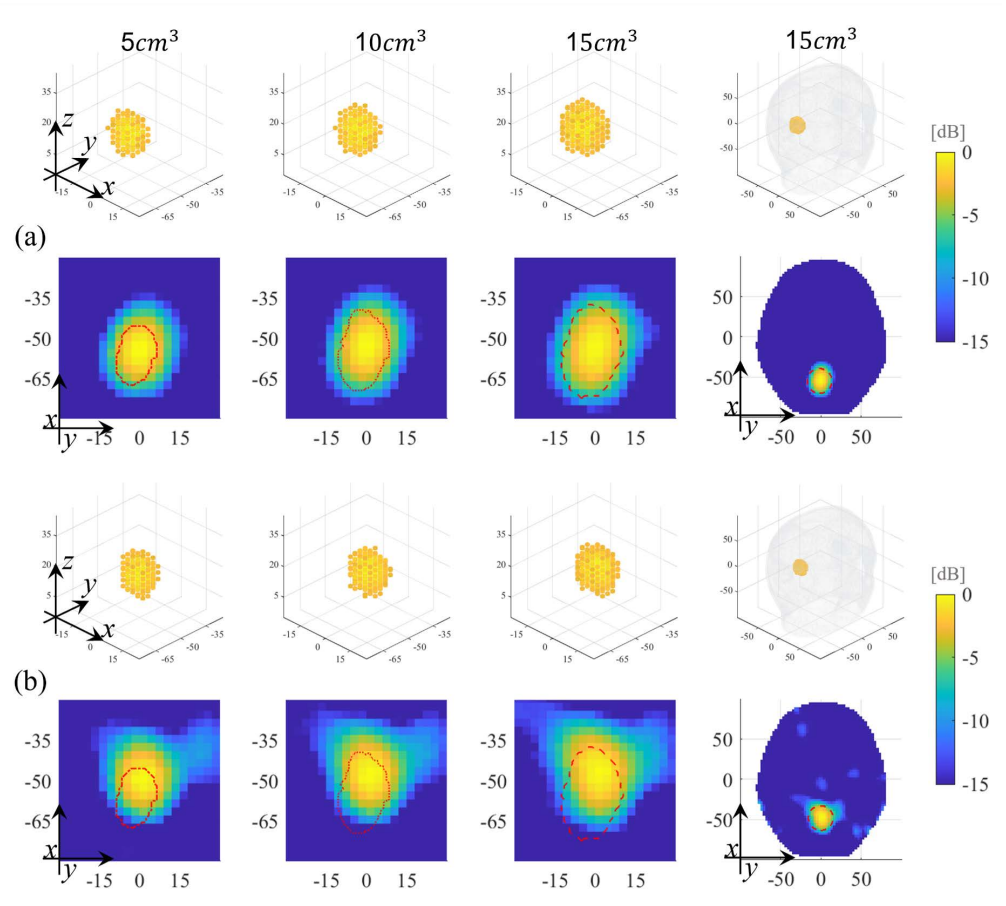

Fig. 4.24 Numerical scenario of HEM progression. Normalized reconstructed dielectric contrast sliced in the middle of the stroke region. (a) Homogeneous head; (b)multi-tissue head.

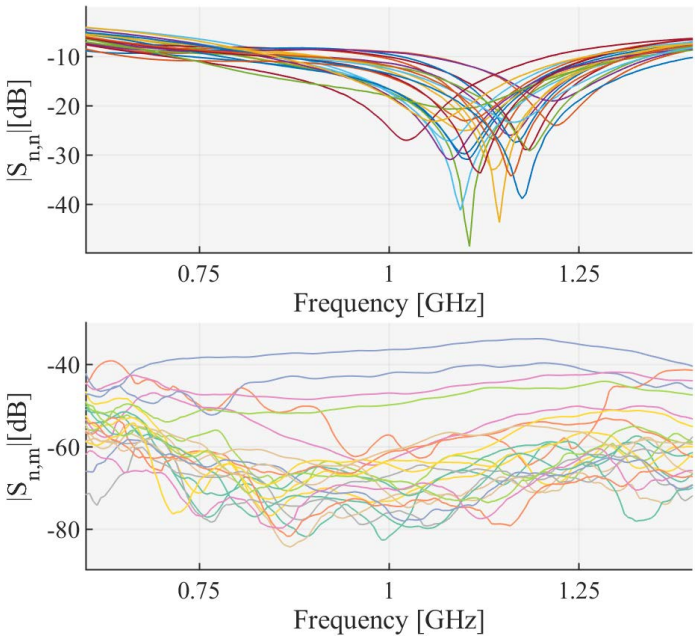

Fig. 4.25 S-parameters amplitude; (Top): reflection coefficients, each line corresponds to the $|S_{n,n}|$ in dB for the n-th antenna of the MWI system with $n = 1,\ldots,22$; (bottom): transmission coefficients, each line corresponds to the $|S_{m,n}|$ in dB with $n = 1$ (transmitting antenna) and $m = 2,\ldots,22$ (receiving antennas).([82]©2022 IEEE)

is not accurately found. However, the result in 4.24(b) represents a great result if we consider the limited amount of a-priori information about the patient added to the operator, showing the potential of the technique in future clinical cases with this kind of situation.

4.2.2 Experimental Validation: Monitoring

Before getting into the imaging, Fig. 4.25 depicts the measured S-parameter for all the antennas, wherein the top is the reflections and at the bottom is the transmission of one of the antennas with all the others. The reflections show that the operation band of this design is shifted to higher frequencies in comparison with the previous one. Though, it still can be used in the band around 1 GHz. Indeed, we decide to work in the band from 0.8 to 1.0 GHz, where the performance of the antennas is less variable, being more in line with the imaging kernel. Regarding the variability, it might be derived from the variability of the manufacturing process that was more noticeable when the brick was reduced, and it is affecting directly the near zone of

the antenna. On the other hand, the transmission parameters show a response above the -80 dB, adequate for the application.

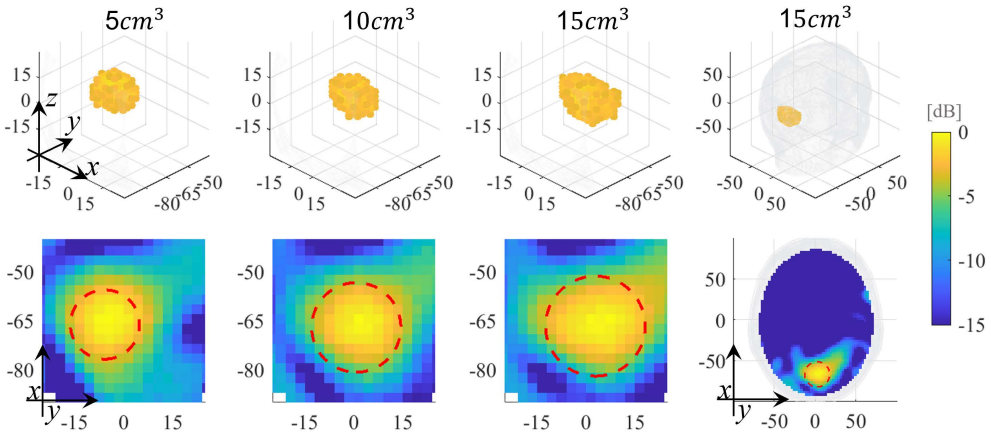

Fig. 4.26 Experimental monitoring of HEM progression. Normalized reconstructed dielectric contrast sliced in the middle of the stroke region, [82]©2022 IEEE.

Now, moving to the physical experiment, the new system is just tested using the homogeneous head phantom. The first test then mimics the previously numerically modeled situation, i.e. a variation between 5 to $15cc^3$ with the hemorrhage placed in the back of the head. The results are depicted in 4.26, being an optimal outcome, since are the first experimental validation in real-time of dynamic monitoring in a true-to-life scenario mimicking brain stroke, at the date of the presentation of the results in [82], to the best of the authors' knowledge.

To extend experimental validation of the second version of the device, as the second test, it is used a different stroke with a bigger volume and more canonical shape. Thus, it aims to track the variation in a single direction. This approach allows for identifying easier the zone changing, contrary to the previously considered case with an approximated radial variation. In this case, the experiment considers both HEM and ISC mixtures for the stroke. The initial stroke position is fixed at back part of the right hemisphere and then filled gradually with 20 cm^3 steps. However, considering the monitoring normally does not have a healthy condition at t_0, here the differential s-parameter are taken between the ones at two consecutive states, i.e., (I) Case 0 (healthy)-20 cm^3; (II) Case 20-40 cm^3; (III) Case 40-60 cm^3. For the imaging, it was used again an average-head-based operator, though in this case is a multi-frequency one with five equally spaced points in the 0.8–1 GHz band.

Thus, the input of the algorithm are $22 \times 22 \times 5$ S-parameter as the one in Fig. 4.27, where also can be noticed the system is working close to at we are get close to the noise floor of the VNA, with differential signals around the -110 dB, but still with a working margin as shown later the imaging results.

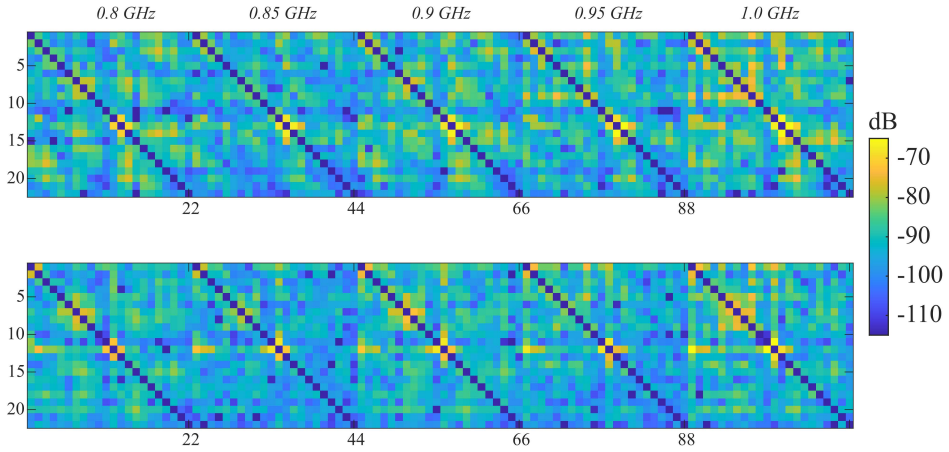

Fig. 4.27 Multi-freq differential scattering matrices for 0 to 20 cm^3 volume variation. (Top) Hemorrhagic case; (Bottom) Ischemic case.

Figures 4.28 and 4.29 illustrate the normalized contrast reconstruction of the different consider cases, where the white contours give an indication of the real position of the stroke during the experiment. Then by row, from top to bottom, there are the sagittal, frontal, and transverse views, cut at the center of the maximum of the contrast. While the columns indicate the reported case. For convenience, since the results are very similar to the previous, Fig.4.29 only reports the transversal view, being the most representative.

In order to verify the repeatability of the measurements, the data collected at different times in the same scenario have been compared. For example, Figs.4.30II.a-II.b, present the differential scattering matrices for two 0-20 cm^3 evolution cases, while Fig.4.30II.a-II.b, refer to two 20-40 cm^3 variations; both cases give similar patterns, meaning that the measurements are consistent. A further verification is given in Fig. 4.31, with the corresponding reconstructed images comparable to the counterparts in Fig. 4.28, I.c, II.c.

Moreover, the system has been tested against false positives: for this purpose, the data gathered at different measuring times, in the same scenario, were differentiated to obtain the input scattering matrix for the algorithm; in the images, the contrast

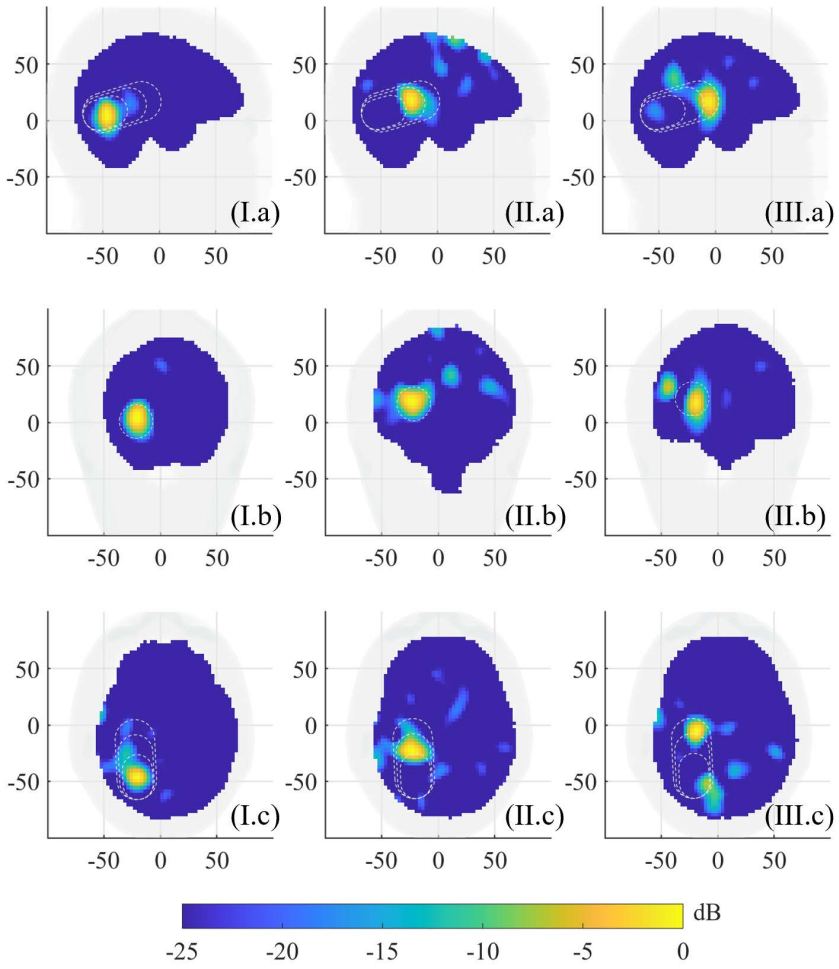

Fig. 4.28 Monitoring of HEM progression. Normalized reconstructed dielectric contrast sliced in the middle of the stroke region. (I) Case 0 (healthy)-20 cm^3; (II) Case 20-40 cm^3; (III) Case 40-60 cm^3. (a) Sagittal view; (b) frontal view; (c) transverse view, [75] ©2022 IEEE.

has been normalized with respect to the maximum value in the previous outcomes. The results for two cases with different stroke volumes are provided: in particular, the differential scattering matrices are shown in Fig. 4.32, while in Fig. 4.33 can be observed the imaged slices, where no changes are detected.

The last test aims to extend the capabilities of the system indicating computing in an experimental scenario the tracking pathological parameter, defined in the previous chapter, which is a temporal indication of the variation of the contrast when the

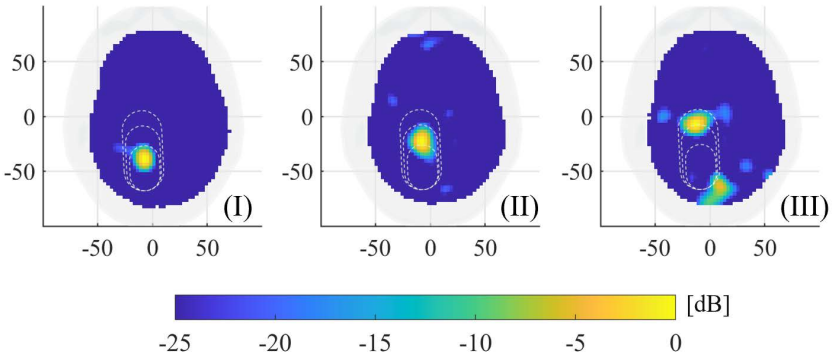

Fig. 4.29 Monitoring of IS progression, transverse view. Normalized reconstructed dielectric contrast sliced in the middle of the stroke region. (I) Case 0(healthy)-20 cm^3; (II) Case 20-40 cm^3; (III) Case 40-60 cm^3.(©2022 IEEE)

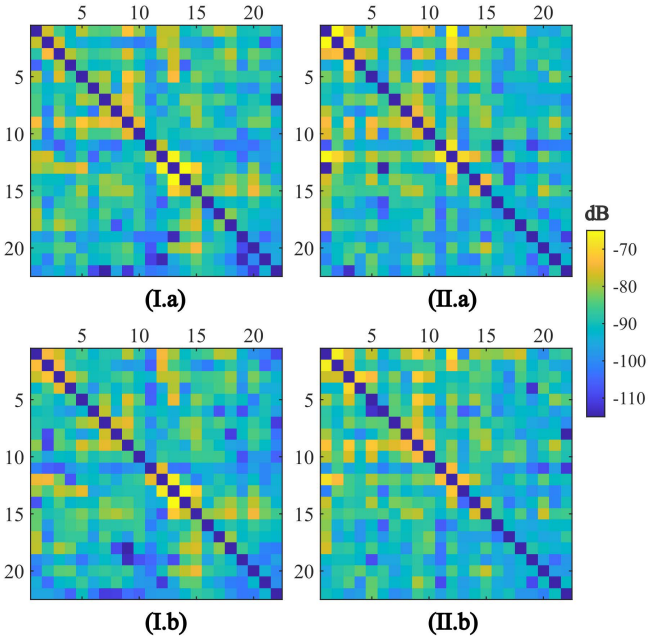

Fig. 4.30 Repeatability study: differential scattering matrices for the HEM case. (I.a, I.b) Distinct measurements of equivalent variations 0 to 20 cm^3 at 1GHz; (II.a, II.b) distinct measurements of equivalent variations 20 to 40 cm^3 at 1GHz, [75] ©2022 IEEE

type of stroke is known. So that, assuming that one knows the type of stroke, this parameter nods the growing or shrinking situation.

Figures 4.34 and 4.35 demonstrate for HEM and ISC cases, this last parameter can signal if a determined contrast (top-row in the figure) comes from the spreading of the stroke-affected area or instead is a recovered zone. Concerning the artifacts

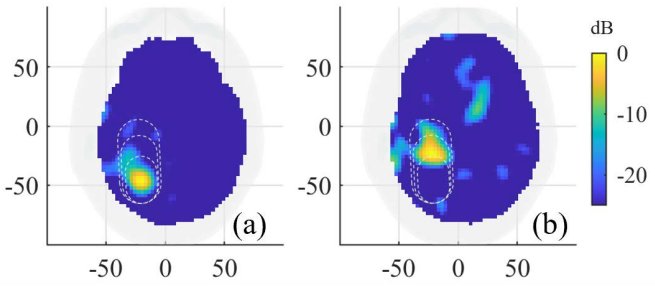

Fig. 4.31 Repeatability study: normalized reconstructed dielectric contrast for a 0-20 cm^3 case (a) and 20-40 cm^3 case (b), comparable to the counterparts obtained from distinct measurements in Fig. 4.28, I.c, II.c, respectively, [75] ©2022 IEEE.

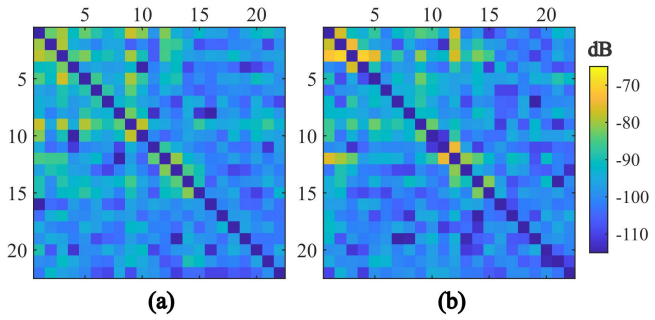

Fig. 4.32 False positive test: differential scattering matrices between two different measurements of the same scenario. (a) 20 cm^3 stroke; (b) 40 cm^3 stroke, [75] ©2022 IEEE

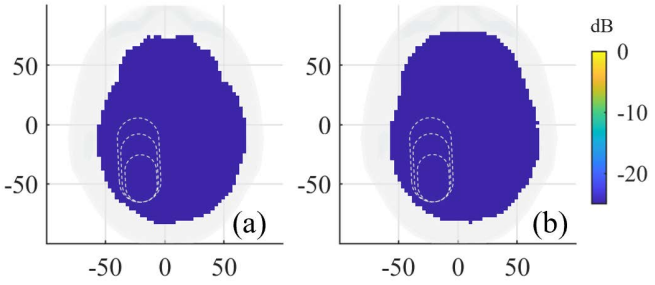

Fig. 4.33 False positive test: reconstructed dielectric contrast between two different measurements of the same scenario. (a) 20 cm^3 stroke; (b) 40 cm^3 stroke. The values are normalized with respect to the maximum obtained in previous detection cases, [75] ©2022 IEEE.

aroused in the back of the brain, especially in the IS case, a realistic hypothesis is that it is due to the presence of the tube feeding the balloon, which could undergo undesired movements.

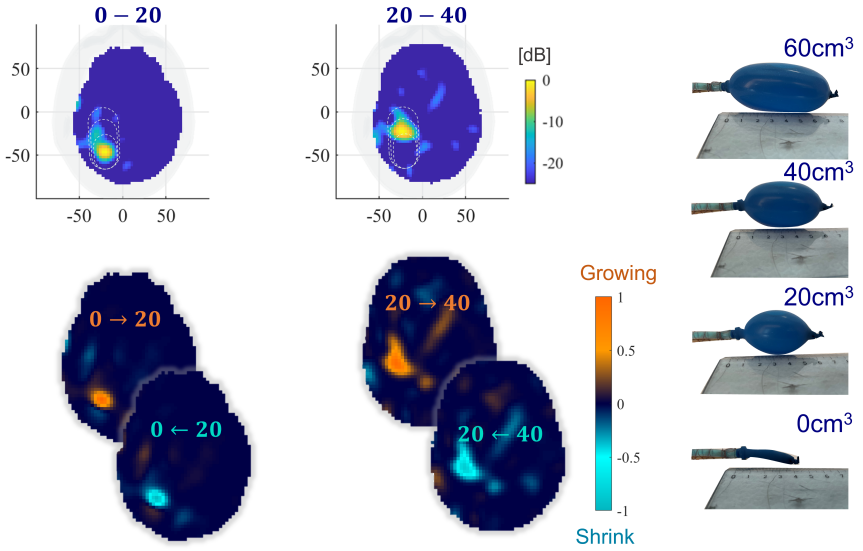

Fig. 4.34 Recovery tracking of an HEM case.

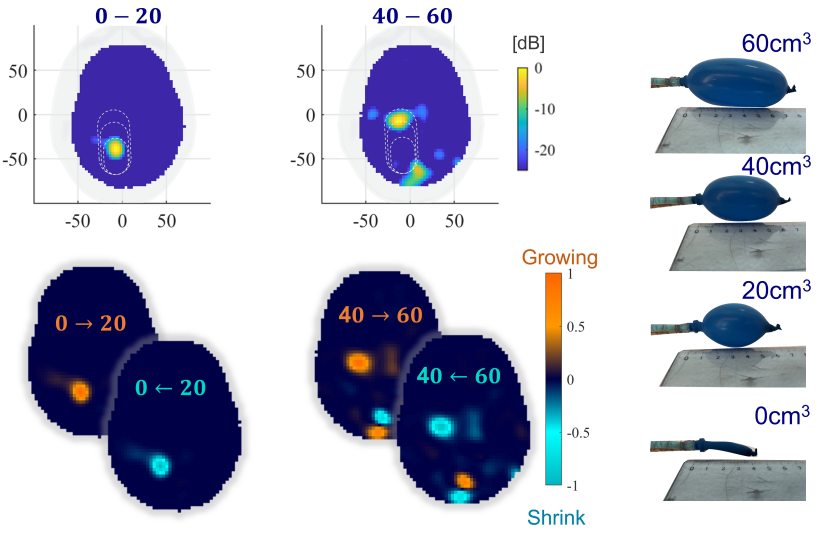

Fig. 4.35 Recovery tracking of an IS case.

4.2.3 Results Discussion

The validation of the proposed imaging system was performed in two big parts, including each the respective version of the system. Thus, the system was initially tested numerically using twin virtual models, and later experimentally using repre-

sentative lab experiments, proving the validity and functionality of the numerical part as an analysis and design tool. The tests consider first the antenna individually and conclude with the whole system test. Overall, the systems demonstrate their capabilities to perform imaging in realistic mimic both HEM and IS stroke situations validating the design process, system functioning, and the imaging algorithm.

The first system presents the first proof-of-concept of the non-liquid matching medium, switching matrix, calibration schemes, and differential imaging algorithm, concentrating the testing on detection, localization, and shape estimation. In this case, the system was able to identify correctly the affected area in homogeneous and multi-tissue head cases. However, the system proves its basic functionality, it presents a limited shape retrieval and a lacking of features of portability that are required for a pre-clinical device. Therefore, the second version aims, first, to reduce the dimensions of the system while keeping the imaging capabilities, thus, an innovative wearable antenna array is proposed. Moreover, considering the open medical need, the testing concentrates on the follow-up capabilities to monitor the post-onset evolution of the stroke in real-time. In this case, a dynamic phantom was employed to emulate stroke evolution over time, and the imaging algorithm is integrated with artifact removal procedures, that provide low noise dielectric contrast reconstructions.

System v.2.0 outcomes proves the reliability of the system in localizing the variation of the stroke-affected area with a sensitivity of about 1 cm, comparable with the theoretical resolution. The variable target is identified evenly, even in the z-direction, where there are a lower number of antennas and the variation was also smaller, due to a slight slope in the positioning of the stroke phantom. These results are very meaningful, not just because of the quality of the resulting images, which are focused and have a low number of artifacts, but because those are computed with a low-complexity device with just 22 antennas. Also, the system allows the assessment of the disease status, namely if there is growth or shrinkage between following exams, of great interest for clinical practice.

Moreover, in view of the clinical scenarios, it is important to remark that the experimental multi-tissue case with the system 1.0 and the numerical one with the system 2.0 have shown the potential of the system, as a whole, to perform even with limited information about the morphology of the patient. The mentioned results still have a big room for improvement, but these are an excellent starting point.

Chapter 5

Conclusions and Perspectives

5.1 Conclusions

The development carried out in this work was spread on two fronts, one related to software and numerical modeling and another on the hardware design and implementation, which converged during the validation stages. As a result, the primary outcome of this project is the first functional 3-D MWI prototype able to live-tracking the brain stroke in realistically mimicked scenarios using a low-complexity architecture. However, defragmenting the big picture in its support bricks and milestones. Some of the notable contributions of this thesis are:

- Developed, modeled, and validated highly realistic twin electromagnetic numerical models of complex clinical scenarios, which were fundamentals for building the imaging kernel and speeding up the design process.
- Design, implementation, manufacture, and characterization of novel antennas, considering the concept of antenna-unit as a single element that includes a radiator and a discrete coupling medium.
- Ideation/implementation of new calibration strategies makes the MWI device more robust to ordinary operation, which is fundamental thinking in a future pre-clinical trial.

- Provide a strong validation of the differential imaging scheme that, that validates the potential of the method as an instrument between full inverse scattering imaging(iterative) and classification approaches.
- Integration of numerical elements, imaging algorithms, and hardware functioning all commissioning the imaging system reliably and efficiently.
- Design and implementation of clinical mimicked scenarios that allow us to validate the device in meaningful situations, recreating head and stroke phantom with diverse strategies.
- Development of a completely functional MWI pre-clinical prototype for brain stroke.

Closing the idea, we move from the design to implementation, finishing with the experimental validation of the MWI via mimicked clinical scenarios, demonstrating agreement between the numerical and real-life experiments. Though the final result is still a lab prototype used for the proof-of-concept, this represents an enormous step toward a pre-clinical device, and then to the final users.

5.2 Perspectives

Looking into the future the potential of MWI in medical applications is huge. However, accelerating its transition to the clinical side will require, first, a major collaboration between physicians, technicians, and patients that guides and explores the potentialities of the technology in a more efficient way. For instance, one point to exploit is the complementary feature of MWI.

On the other hand, with the exponential growth of the computational power, hardware acceleration, and the arrival of machine learning algorithms, it could be also imagined in the future applications of iterative approaches in real time[58, 86]. In the specific of the device presented here, it is planned to extend the experimental validation using a more complex phantom, considering multiple tissues. Also, the reduction of the measured time, now limited by the switching matrix, is planned using solid-state switches. Moreover, machine learning classification algorithms that determine the typology of stroke are also in development. Finally, as the

experimental part demonstrates there is still a lot of room for calibration techniques that give robustness to the measuring process, between them a possible option could be to calibrate directly the operator using measured data [87–89], instead of the traditional calibration of the s-parameters. Moreover, the system capabilities can be enhanced with the use of metamaterials[90, 91], or sparsity-promoting regularization schemes [92].

Bibliography

[1] W. Johnson, O. Onuma, M. Owolabi, and S. Sachdev, "Stroke: a global response is needed," *Bulletin of the World Health Organization*, vol. 94, no. 9, pp. 634 – 634A, 2016-9-01.

[2] S. S. Virani, Á. Alonso, E. J. Benjamin, M. S. Bittencourt, C. Callaway, A. P. Carson, A. M. Chamberlain, A. R. Chang, S. Cheng, F. N. Delling, L. Djoussé, M. S. V. Elkind, J. F. Ferguson, M. Fornage, S. S. Khan, B. M. Kissela, K. L. Knutson, T. W. Kwan, D. T. Lackland, T. T. Lewis, J. H. Lichtman, C. T. Longenecker, M. S. Loop, P. L. Lutsey, S. S. Martin, K. Matsushita, A. E. Moran, M. E. Mussolino, A. M. Perak, W. D. Rosamond, G. A. Roth, U. Sampson, G. M. Satou, E. B. Schroeder, S. H. Shah, C. M. Shay, N. L. Spartano, A. C. Stokes, D. L. Tirschwell, L. B. VanWagner, and C. W. Tsao, "Heart disease and stroke statistics2020 update: A report from the american heart association," in *Circulation*, 2020.

[3] H. Gray, P. Williams, L. Bannister, and I. L. D. Collection, *Gray's Anatomy: The Anatomical Basis of Medicine and Surgery*. Gray's Anatomy, Churchill Livingstone, 1995.

[4] R. A. Felberg and A. Naidech, "The five ps of acute ischemic stroke treatment: Parenchyma, pipes, perfusion, penumbra, and prevention of complications," *Ochsner Journal*, vol. 5, no. 1, pp. 5–11, 2003.

[5] B. Norrving, J. Barrick, A. Davalos, M. Dichgans, C. Cordonnier, A. Guekht, K. Kutluk, R. Mikulik, J. Wardlaw, E. Richard, D. Nabavi, C. Molina, P. M. Bath, K. S. Sunnerhagen, A. Rudd, A. Drummond, A. Planas, and V. Caso, "Action plan for stroke in europe 2018–2030," *European Stroke Journal*, vol. 3, no. 4, pp. 309–336, 2018. PMID: 31236480.

[6] K. B. Walsh, "Non-invasive sensor technology for prehospital stroke diagnosis: Current status and future directions," *International Journal of Stroke*, vol. 14, no. 6, pp. 592–602, 2019. PMID: 31354081.

[7] M. O. Owolabi, A. G. Thrift, A. Mahal, M. Ishida, S. Martins, W. D. Johnson, J. Pandian, F. Abd-Allah, J. Yaria, H. T. Phan, G. Roth, S. L. Gall, R. Beare, T. G. Phan, R. Mikulik, R. O. Akinyemi, B. Norrving, M. Brainin, and V. L. Feigin, "Primary stroke prevention worldwide: translating evidence into action," *The Lancet Public Health*, vol. 7, no. 1, pp. e74–e85, 2022.

[8] R. Chandra, H. Zhou, I. Balasingham, and R. M. Narayanan, "On the opportunities and challenges in microwave medical sensing and imaging," *IEEE Transactions on Biomedical Engineering*, vol. 62, no. 7, pp. 1667–1682, 2015.

[9] M. Persson, A. Fhager, H. D. Trefná, Y. Yu, T. McKelvey, G. Pegenius, J.-E. Karlsson, and M. Elam, "Microwave-based stroke diagnosis making global prehospital thrombolytic treatment possible," *IEEE Transactions on Biomedical Engineering*, vol. 61, pp. 2806–2817, 2014.

[10] "EMTensor." Available at https://www.emtensor.com/.

[11] D. Cook, H. Brown, I. Widanapathirana, D. Shah, J. Walsham, A. Trakic, G. Zhu, A. Zamani, L. Guo, A. Brankovic, A. Al-Saffar, A. Stancombe, A. Bialkowski, P. Nguyen, K. Bialkowski, S. Crozier, and A. Abbosh, "Case report: Preliminary images from an electromagnetic portable brain scanner for diagnosis and monitoring of acute stroke," *Frontiers in Neurology*, vol. 12, 2021.

[12] S. Candefjord, J. Winges, A. A. Malik, Y. Yu, T. Rylander, T. McKelvey, A. Fhager, M. Elam, and M. Persson, "Microwave technology for detecting traumatic intracranial bleedings: tests on phantom of subdural hematoma and numerical simulations," *Medical & Biological Engineering & Computing*, vol. 55, pp. 1177 – 1188, 2016.

[13] S. Semenov, M. Hopfer, R. Planas, A. Hamidipour, and T. Henriksson, "Electromagnetic tomography for brain imaging: 3d reconstruction of stroke in a human head phantom," in *2016 IEEE Conference on Antenna Measurements Applications (CAMA)*, pp. 1–4, 2016.

[14] P. Lu and P. Kosmas, "Three-dimensional microwave head imaging with gpu-based fdtd and the dbim method," *Sensors*, vol. 22, no. 7, 2022.

[15] I. Bisio, A. Fedeli, C. Garibotto, F. Lavagetto, M. Pastorino, and A. Randazzo, "Two ways for early detection of a stroke through a wearable smart helmet: Signal processing vs. electromagnetism," *IEEE Wireless Communications*, vol. 28, no. 3, pp. 22–27, 2021.

[16] A. Fedeli, V. Schenone, A. Randazzo, M. Pastorino, T. Henriksson, and S. Semenov, "Nonlinear s-parameters inversion for stroke imaging," *IEEE Transactions on Microwave Theory and Techniques*, vol. 69, no. 3, pp. 1760–1771, 2021.

[17] A. S. M. Alqadami, A. Trakic, A. E. Stancombe, B. Mohammed, K. Bialkowski, and A. Abbosh, "Flexible electromagnetic cap for head imaging," *IEEE Transactions on Biomedical Circuits and Systems*, vol. 14, no. 5, pp. 1097–1107, 2020.

[18] A. S. M. Alqadami, A. Zamani, A. Trakic, and A. Abbosh, "Flexible electromagnetic cap for three-dimensional electromagnetic head imaging," *IEEE Transactions on Biomedical Engineering*, vol. 68, no. 9, pp. 2880–2891, 2021.

[19] O. Fiser, V. Hruby, J. Vrba, T. Drizdal, J. Tesarik, J. Vrba, and D. Vrba, "Uwb bowtie antenna for medical microwave imaging applications," *IEEE Transactions on Antennas and Propagation*, pp. 1–1, 2022.

[20] I. Bisio, A. Fedeli, C. Garibotto, F. Lavagetto, M. Pastorino, and A. Randazzo, "Two ways for early detection of a stroke through a wearable smart helmet: Signal processing vs. electromagnetism," *IEEE Wireless Communications*, vol. 28, no. 3, pp. 22–27, 2021.

[21] G. Zhu, A. Bialkowski, L. Guo, B. Mohammed, and A. Abbosh, "Stroke classification in simulated electromagnetic imaging using graph approaches," *IEEE Journal of Electromagnetics, RF and Microwaves in Medicine and Biology*, vol. 5, no. 1, pp. 46–53, 2021.

[22] A. Brankovic, A. Zamani, A. Trakic, K. Bialkowski, B. Mohammed, D. Cook, J. Walsham, and A. M. Abbosh, "Unsupervised algorithm for brain anomalies localization in electromagnetic imaging," *IEEE Transactions on Computational Imaging*, vol. 6, pp. 1595–1606, 2020.

[23] A. Al-Saffar, L. Guo, and A. Abbosh, "A tripartite data-driven approach for wide-band electromagnetic imaging," *IEEE Transactions on Computational Imaging*, vol. 7, pp. 1278–1288, 2021.

[24] G. Fang, P. Xu, and W. Liu, "Automated ischemic stroke subtyping based on machine learning approach," *IEEE Access*, vol. 8, pp. 118426–118432, 2020.

[25] M. Persson, A. Fhager, H. D. Trefná, Y. Yu, T. McKelvey, G. Pegenius, J.-E. Karlsson, and M. Elam, "Microwave-based stroke diagnosis making global prehospital thrombolytic treatment possible," *IEEE Transactions on Biomedical Engineering*, vol. 61, pp. 2806–2817, 2014.

[26] D. Cook, H. Brown, I. Widanapathirana, D. Shah, J. Walsham, A. Trakic, G. Zhu, A. Zamani, L. Guo, A. Brankovic, A. Al-Saffar, A. Stancombe, A. Bialkowski, P. Nguyen, K. Bialkowski, S. Crozier, and A. Abbosh, "Case report: Preliminary images from an electromagnetic portable brain scanner for diagnosis and monitoring of acute stroke," *Frontiers in Neurology*, vol. 12, 2021.

[27] D. M. Godinho, J. Felicio, C. A. Fernandes, and R. C. Conceicao, "Experimental evaluation of an axillary microwave imaging system to aid breast cancer staging," *IEEE Journal of Electromagnetics, RF and Microwaves in Medicine and Biology*, pp. 1–1, 2021.

[28] K. S. Sultan, B. Mohammed, M. Manoufali, and A. M. Abbosh, "Portable electromagnetic knee imaging system," *IEEE Transactions on Antennas and Propagation*, vol. 69, no. 10, pp. 6824–6837, 2021.

[29] C. Dachena, A. Fedeli, A. Fanti, M. B. Lodi, M. Pastorino, and A. Randazzo, "Microwave imaging for the diagnosis of cervical diseases: A feasibility analysis," *IEEE Journal of Electromagnetics, RF and Microwaves in Medicine and Biology*, vol. 5, no. 3, pp. 277–285, 2021.

[30] M. Savazzi, S. Abedi, N. Ištuk, N. Joachimowicz, H. Roussel, E. Porter, M. O'Halloran, J. R. Costa, C. A. Fernandes, J. M. Felício, and R. C. Conceição, "Development of an anthropomorphic phantom of the axillary region for microwave imaging assessment," *Sensors*, vol. 20, no. 17, 2020.

[31] M. Savazzi, J. R. Costa, C. A. Fernandes, J. M. Felício, and R. C. Conceição, "Numerical assessment of microwave imaging for axillary lymph nodes screening using anthropomorphic phantom," in *2021 15th European Conference on Antennas and Propagation (EuCAP)*, pp. 1–4, 2021.

[32] A. Prokhorova, S. Ley, and M. Helbig, "Quantitative interpretation of uwb radar images for non-invasive tissue temperature estimation during hyperthermia," *Diagnostics*, vol. 11, no. 5, 2021.

[33] M. Wang, L. Crocco, and M. Cavagnaro, "On the design of a microwave imaging system to monitor thermal ablation of liver tumors," *IEEE Journal of Electromagnetics, RF and Microwaves in Medicine and Biology*, vol. 5, no. 3, pp. 231–237, 2021.

[34] J.-C. Bolomey, *Crossed Viewpoints on Microwave-Based Imaging for Medical Diagnosis: From Genesis to Earliest Clinical Outcomes*, pp. 369–414. Cham: Springer International Publishing, 2018.

[35] M. Bertero and P. Boccacci, *Introduction to Inverse Problems in Imaging*. Inst. Phys., Bristol, U.K., 1998.

[36] C. Xudong, *Computational Methods for Electromagnetic Inverse Scattering*. Wiley-IEEE Press, 2018.

[37] N. K. Nikolova, *Introduction to Microwave Imaging*. EuMA High Frequency Technologies Series, Cambridge University Press, 2017.

[38] E. A. Attardo, A. Borsic, G. Vecchi, and P. M. Meaney, "Whole-system electromagnetic modeling for microwave tomography," *IEEE Antennas and Wireless Propagation Letters*, vol. 11, pp. 1618–1621, 2012.

[39] D. O. Rodriguez-Duarte, J. A. T. Vasquez, R. Scapaticci, L. Crocco, and F. Vipiana, "Assessing a microwave imaging system for brain stroke monitoring via high fidelity numerical modelling," *IEEE Journal of Electromagnetics, RF and Microwaves in Medicine and Biology*, vol. 5, no. 3, pp. 238–245, 2021.

[40] D. O. Rodriguez-Duarte, J. A. Tobon Vasquez, R. Scapaticci, G. Turvani, M. Cavagnaro, M. R. Casu, L. Crocco, and F. Vipiana, "Experimental validation of a microwave system for brain stroke 3-d imaging," *Diagnostics*, vol. 11, no. 7, 2021.

[41] J. A. Tobon Vasquez, R. Scapaticci, G. Turvani, G. Bellizzi, N. Joachimowicz, B. Duchêne, E. Tedeschi, M. R. Casu, L. Crocco, and F. Vipiana, "Design and experimental assessment of a 2D microwave imaging system for brain stroke monitoring," *Int. J. Antennas Propag.*, no. Article ID 8065036, p. 12 pages, 2019.

[42] C. Gilmore, P. Mojabi, A. Zakaria, M. Ostadrahimi, C. Kaye, S. Noghanian, L. Shafai, S. Pistorius, and J. LoVetri, "A wideband microwave tomography system with a novel frequency selection procedure," *IEEE Transactions on Biomedical Engineering*, vol. 57, no. 4, pp. 894–904, 2010.

[43] D. O. Rodriguez-Duarte, J. A. T. Vasquez, and F. Vipiana, "Multi-shot calibration technique for microwave imaging systems," in *2021 IEEE Conference on Antenna Measurements Applications (CAMA)*, pp. 476–480, 2021.

[44] V. Teppati, A. Ferrero, and M. Sayed(Eds.), *Modern RF and Microwave Measurement Techniques*. The Cambridge RF and Microwave Engineering Series, Cambridge University Press, 2013.

[45] J. Jianming, *The Finite Element Method in Electromagnetic*. Wiley-IEEE Press, second ed., 2002.

[46] Z. Chen, C.-F. Wang, and W. J. R. Hoefer, "A unified view of computational electromagnetics," *IEEE Transactions on Microwave Theory and Techniques*, vol. 70, no. 2, pp. 955–969, 2022.

[47] S. N. Makarov, G. M. Noetscher, J. Yanamadala, M. W. Piazza, S. Louie, A. Prokop, A. Nazarian, and A. Nummenmaa, "Virtual human models for electromagnetic studies and their applications," *IEEE Reviews in Biomedical Engineering*, vol. 10, pp. 95–121, 2017.

[48] D.Andreuccetti, R.Fossi, and C.Petrucci, "An internet resource for the calculation of the dielectric properties of body tissues in the frequency range 10 hz - 100 ghz. ifac-cnr, florence (italy), 1997. based on data published by c.gabriel et al. in 1996.."

[49] S. Y. Semenov and D. R. Corfield, "Microwave tomography for brain imaging: feasibility assessment for stroke detection," *Int. J. of Antennas and Propagat.*, vol. 2008, p. 8 pages, 2008.

[50] D. Ireland and M. Bialkowski, "Feasibility study on microwave stroke detection using a realistic phantom and the fdtd method," in *2010 Asia-Pacific Microwave Conference*, pp. 1360–1363, 2010.

[51] R. Scapaticci, M. Bjelogrlic, J. A. Tobon Vasquez, F. Vipiana, M. Mattes, and L. Crocco, *Emerging Electromagnetic Technologies for Brain Diseases Diagnostics, Monitoring and Therapy*, ch. 2. Microwave Technology for Brain Imaging and Monitoring: Physical Foundations, Potential and Limitations, pp. 7–35. Springer int. pub., 2018.

[52] R. Scapaticci, J. Tobon, G. Bellizzi, F. Vipiana, and L. Crocco, "Design and numerical characterization of a low-complexity microwave device for brain stroke monitoring," *IEEE Transactions on Antennas and Propagation*, vol. 66, no. 12, pp. 7328–7338, 2018.

[53] R. Scapaticci, L. D. Donato, I. Catapano, and L. Crocco, "A feasibility study on Microwave Imaging for brain stroke monitoring," *Prog. Electromagn. Res. B*, vol. 40, pp. 305–324, 2012.

[54] C. Balanis, *Advanced Enginnering Electromagnetics*. Willeys, 1989.

[55] M. Slaney, A. Kak, and L. Larsen, "Limitations of imaging with first-order diffraction tomography," *IEEE Transactions on Microwave Theory and Techniques*, vol. 32, no. 8, pp. 860–874, 1984.

[56] O. M. Bucci, L. Crocco, R. Scapaticci, and G. Bellizzi, "On the design of phased arrays for medical applications," *Proc. IEEE*, vol. 104, pp. 633–648, Mar. 2016.

[57] Keysight Technologies, "Keysight 2-port and 4-port PNA network analyzer, N5227A 10 MHz to 67 GHz," *Data Sheet and Technical Specifications*, Apr. 2019.

[58] M. Ricci, B. Štitić, L. Urbinati, G. D. Guglielmo, J. A. T. Vasquez, L. P. Carloni, F. Vipiana, and M. R. Casu, "Machine-learning-based microwave sensing: A case study for the food industry," *IEEE Journal on Emerging and Selected Topics in Circuits and Systems*, vol. 11, no. 3, pp. 503–514, 2021.

[59] X. Li, M. Jalilvand, Y. L. Sit, and T. Zwick, "A compact double-layer on-body matched bowtie antenna for medical diagnosis," *IEEE Transactions on Antennas and Propagation*, vol. 62, no. 4, pp. 1808–1816, 2014.

[60] M. Rokunuzzaman, A. Ahmed, T. C. Baum, and W. S. T. Rowe, "Compact 3-d antenna for medical diagnosis of the human head," *IEEE Transactions on Antennas and Propagation*, vol. 67, no. 8, pp. 5093–5103, 2019.

[61] A. S. M. Alqadami, K. S. Bialkowski, A. T. Mobashsher, and A. M. Abbosh, "Wearable electromagnetic head imaging system using flexible wideband antenna array based on polymer technology for brain stroke diagnosis," *IEEE Transactions on Biomedical Circuits and Systems*, vol. 13, no. 1, pp. 124–134, 2019.

[62] D. O. Rodriguez-Duarte, J. A. T. Vasquez, R. Scapaticci, L. Crocco, and F. Vipiana, "Brick-shaped antenna module for microwave brain imaging systems," *IEEE Antennas and Wireless Propagation Letters*, vol. 19, no. 12, pp. 2057–2061, 2020.

[63] L. Crocco, I. Karanasiou, M. James, and R. C. Conceicao(Eds.), *Emerging Electromagnetic Technologies for Brain Diseases Diagnostics, Monitoring and Therapy*. Springer int. pub., 2018.

[64] O. M. Bucci, L. Crocco, and T. Isernia, "Improving the reconstruction capabilities in inverse scattering problems by exploitation of close-proximity setups," *J. Opt. Soc. Am. A*, vol. 16, pp. 1788–1798, Jul. 1999.

[65] J. A. Tobon Vasquez, R. Scapaticci, G. Turvani, G. Bellizzi, D. O. Rodriguez-Duarte, N. Joachimowicz, B. Duchêne, E. Tedeschi, M. R. Casu, L. Crocco, and F. Vipiana, "A prototype microwave system for 3d brain stroke imaging," *Sensors*, vol. 20, no. 9, 2020.

[66] K. D. P. P. M. Meaney, "Theoretical premises and contemporary optimizations of microwave tomography," in *Microwave Technologies* (K. H. Y. A. Kishk, ed.), pp. 1–24, London: IntechOpen, 2022.

[67] N. Joachimowicz, B. Duchêne, C. Conessa, and O. Meyer, "Anthropomorphic breast and head phantoms for microwave imaging," *Diagnostics*, vol. 85, pp. 1–12, Dec. 2018.

[68] N. Joachimowicz, B. Duchêne, J. A. Tobon Vasquez, R. Scapaticci, G. Turvani, G. Dassano, M. R. Casu, L. Crocco, and F. Vipiana, "Head phantoms for a microwave imaging system dedicated to cerebrovascular disease monitoring," in *IEEE International Conference on Antenna Measurements and Applications (CAMA)*, Sept. 2018.

[69] IEEE, "Ieee recommended practice for determining the peak spatial-average specific absorption rate (sar) in the human head from wireless communications devices: Measurement techniques," *IEEE Std 1528-2013 (Revision of IEEE Std 1528-2003)*, pp. 1–246, 2013.

[70] S. Y. Semenov and D. R. Corfield, "Microwave tomography for brain imaging: Feasibility assessment for stroke detection," *International Journal of Antennas and Propagation*, vol. 2008, pp. 1–8, 2008.

[71] M. A. Stuchly and S. S. Stuchly, "Coaxial line reflection methods for measuring dielectric properties of biological substances at radio and microwave frequencies-a review," *IEEE Transactions on Instrumentation and Measurement*, vol. 29, no. 3, pp. 176–183, 1980.

[72] M. Cavagnaro and G. Ruvio, "Numerical sensitivity analysis for dielectric characterization of biological samples by open-ended probe technique," *Sensors*, vol. 20, no. 13, 2020.

[73] A. Kraszewski, M. A. Stuchly, and S. S. Stuchly, "Ana calibration method for measurements of dielectric properties," *IEEE Transactions on Instrumentation and Measurement*, vol. 32, no. 2, pp. 385–387, 1983.

[74] Keysight Technologies, "Materials measurement suite." https://www.keysight.com/it/en/product/N1500A/materials-measurement-suite.html, 2022.

[75] D. O. Rodriguez-Duarte, C. Origlia, J. A. T. Vasquez, R. Scapaticci, L. Crocco, and F. Vipiana, "Experimental assessment of real-time brain stroke monitoring via a microwave imaging scanner," *IEEE Open Journal of Antennas and Propagations*, 2022.

[76] C. Laredo, Y. Zhao, S. Rudilosso, A. Renú, J. C. Pariente, Á. Chamorro, and X. Urra, "Prognostic significance of infarct size and location: The case of insular stroke," *Scientific Reports*, vol. 8, p. 9498, Jun 2018.

[77] A. Bruno, N. Shah, A. E. Akinwuntan, B. Close, and J. A. Switzer, "Stroke size correlates with functional outcome on the simplified modified rankin scale questionnaire," *Journal of Stroke and Cerebrovascular Diseases*, vol. 22, pp. 781–783, Aug 2013.

[78] J. L. Saver, K. C. Johnston, D. Homer, R. Wityk, W. Koroshetz, L. L. Truskowski, and E. C. Haley, "Infarct volume as a surrogate or auxiliary outcome measure in ischemic stroke clinical trials. the RANTTAS investigators," *Stroke*, vol. 30, pp. 293–298, Feb. 1999.

[79] J. L. Saver, "Time is brain–quantified," *Stroke*, vol. 37, pp. 263–266, Dec. 2005.

[80] "Esun." Available at https://www.esun3d.net/Products/PVA.

[81] "Smooth-on." Available at https://www.smooth-on.com/product-line/dragon-skin/.

[82] D. O. Rodriguez-Duarte, S. de Luque Arias, J. A. Tobon Vasquez, R. Scapaticci, L. Crocco, and F. Vipiana, "A portable microwave scanner for brain stroke monitoring: Design, implementation and experimental validation," in *2022 16th European Conference on Antennas and Propagation (EuCAP)*, pp. 1–5, 2022.

[83] D. O. Rodriguez-Duarte, J. Tobon, R. Scapaticci, B.Kolundzija, L. Crocco, and F. Vipiana, "High fidelity modelling of a microwave imaging device for brain stroke monitoring," in *42nd PhotonIcs and Electromagnetics Research Symposium (PIERS)*, (Xiamen, China), 12 2019.

[84] D. O. Rodriguez-Duarte, J. Tobon, and F. Vipiana, "Realistic numerical modelling for 3-d brain stroke monitoring," in *2020 IEEE International Symposium on Antennas and Propagation and North American Radio Science Meeting*, pp. 1195–1196, 2020.

[85] E. L. Saionz, D. Tadin, M. D. Melnick, and K. R. Huxlin, "Functional preservation and enhanced capacity for visual restoration in subacute occipital stroke," *Brain*, vol. 143, pp. 1857–1872, 05 2020.

[86] M. A. Mansoori, P. Lu, and M. R. Casu, "Fpga acceleration of 3d fdtd for multi-antennas microwave imaging using hls," *IEEE Access*, vol. 9, pp. 122696–122711, 2021.

[87] D. O. Rodriguez-Duarte, J. A. Tobon Vasquez, and F. Vipiana, "Hybrid simulation-measurement calibration technique for microwave imaging systems," in *2021 15th European Conference on Antennas and Propagation (EuCAP)*, pp. 1–5, 2021.

[88] D. O. Rodriguez-Duarte, C. Origlia, J. A. T. Vasquez, and F. Vipiana, "Hybrid resolvent kernel calibration technique for microwave imaging systems," in *2021 IEEE International Symposium on Antennas and Propagation and USNC-URSI Radio Science Meeting (APS/URSI)*, pp. 2014–2015, 2021.

[89] C. Origlia, D. O. Rodriguez-Duarte, J. A. Tobon Vasquez, and F. Vipiana, "Microwave antenna array calibration via simulated and measured s-parameters matching," in *2022 16th European Conference on Antennas and Propagation (EuCAP)*, pp. 1–5, 2022.

[90] E. Razzicchia, N. Ghavami, D. O. Rodriguez-Duarte, J. A. Tobon Vasquez, F. Vipiana, and P. Kosmas, "Benefits of employing metasurfaces on the design of a microwave brain imaging scanner," in *2021 International Conference on Electromagnetics in Advanced Applications (ICEAA)*, pp. 141–141, 2021.

[91] N. Ghavami, E. Razzicchia, O. Karadima, P. Lu, W. Guo, I. Sotiriou, E. Kallos, G. Palikaras, and P. Kosmas, "The use of metasurfaces to enhance microwave imaging: Experimental validation for tomographic and radar-based algorithms," *IEEE Open Journal of Antennas and Propagation*, vol. 3, pp. 89–100, 2022.

[92] S. Vakalis and J. A. Nanzer, "Analysis of array sparsity in active incoherent microwave imaging," *IEEE Geoscience and Remote Sensing Letters*, vol. 17, no. 1, pp. 57–61, 2020.